Microfluidic Devices and Biological Lasers for Biophotonic Applications

Mark D. Mackenzie

Submitted for the degree of Doctor of Philosophy

Department of Physics

School of Engineering and Physical Sciences

Heriot-Watt University

February - 2017

Abstract

The increasing collaboration between physicists and biologists in recent years has led to a series of breakthroughs enabled, in part, by the use of lasers in biological experiments. Once such recent development is the biological laser where a living cell containing a fluorescent protein or dye acts as a laser gain medium. This thesis presents work designed to develop the idea of the living laser leading to their implementation as a research tool. This work has consisted of two main areas of research; microfluidics and biological lasers.

The use of microfluidics enables the miniaturisation of many existing types of biological diagnostics. In this thesis devises are demonstrated for use in temperature sensing and flow cytometry. These were fabricated through the use of Ultrafast Laser Inscription (ULI) and selective chemical etching. As part of this work we have also investigated the integration of silver nanoparticles into microfluidic devices, using photo-reduction, for the enhancement of Raman sensing.

Several types of living laser have been fabricated containing different fluorescent dyes and Enhanced Green Fluorescent Protein (eGFP). Lifetime extension has been achieved using vitamin C and work has been conducted towards demonstrating calcium sensing inside cells. As an alternative to the dyes used in these experiments we have also investigated the use of upconverting nanoparticles.

Acknowledgments

I would like to thank the many people who have helped and supported me throughout my time at Heriot-Watt University both as an MSc student and during my PhD. Most of all I would like to thank Prof. Ajoy Kar and Dr Lynn Paterson who have provided constant guidance and advice throughout and without who I would not have been able conduct this work.

My group members have provided help and support both as colleagues and as friends over the last 4 years. My thanks to current members Giorgos Demetriou, Nitin Jha, Anusha Keloth, Adam Lancaster, James Morris and Fiona Thorburn. Previous group members Asheigh Barron, Rose Mary, Stephen Beecher, John McCarthy, John Macdonald and especially Debaditya Choudhury. The excellent help, training and advice provided by Adi at the start of my PhD has proven invaluable throughout.

My PhD has included collaborations with various groups and institutions which has aided in my research and also allowed me to visit places I would not otherwise have had the opportunity to see.

Prof. Rory Duncan and his group members with who I worked on biological lasers. Katarzyna Cialowicz, Charlotte Hamilton, Kirsty Martin and Rebecca Saleeb. Veerendra Kalyan Jagannadh and Ashlesha Bhide of the Indian Institute of Science who I worked with on microfluidics and silver nanoparticles. Blanca del Rosal and Paloma Rodríguez-Sevilla of Universidad Autónoma de Madrid with who I worked with on microfluidics and upconverting materials. When visiting their institutions, I was always made to feel welcome and enjoyed my time there greatly.

Finally, I would like to again thank my supervisors Prof. Ajoy Kar and Dr Lynn Paterson as well as my family for their encouragement and support in writing my thesis.

Name:	Mark D. Mackenzie		
School/PGI:	School of Engineering and Physical Sciences		
Version: *(i.e. First, Resubmission, Final)*	Final	Degree Sought (Award **and** Subject area)	PhD Physics

Declaration

In accordance with the appropriate regulations I hereby submit my thesis and I declare that:

1) the thesis embodies the results of my own work and has been composed by myself

2) where appropriate, I have made acknowledgement of the work of others and have made reference to work carried out in collaboration with other persons

3) the thesis is the correct version of the thesis for submission and is the same version as any electronic versions submitted*.

4) my thesis for the award referred to, deposited in the Heriot-Watt University Library, should be made available for loan or photocopying and be available via the Institutional Repository, subject to such conditions as the Librarian may require

5) I understand that as a student of the University I am required to abide by the Regulations of the University and to conform to its discipline.

* *Please note that it is the responsibility of the candidate to ensure that the correct version of the thesis is submitted.*

Signature of Candidate:		Date:	

Submission

Submitted By *(name in capitals)*:	
Signature of Individual Submitting:	
Date Submitted:	

For Completion in the Student Service Centre (SSC)

Received in the SSC by *(name in capitals)*:			
Method of Submission *(Handed in to SSC; posted through internal/external mail)*:			
E-thesis Submitted (mandatory for final theses)			
Signature:		Date:	

Publications by the author

Peer reviewed journal articles by the author

1. B. del Rosal, C. Sun, Y. Yan, M. D. Mackenzie, C. Lu, A. A. Bettiol, A. K. Kar, and D. Jaque, "Flow effects in the laser-induced thermal loading of optical traps and optofluidic devices," Opt. Express **22**, 23938-23954 (2014).

2. V. K. Jagannadh, M. D. Mackenzie, P. Pal, A. K. Kar, S. S. Gorthi, "Imaging Flow Cytometry With Femtosecond Laser-Micromachined Glass Microfluidic Channels," IEEE Journal of Selected Topics in Quantum Electronics **21**, 4 (2015).

3. P. Rodríguez-Sevilla, L. Labrador-Páez, D. Wawrzyńczyk, M. Nyk, M. Samoć, A. K. Kar, M. D. Mackenzie, L. Paterson, D. Jaque, P. Haro-González, "Determining the 3D orientation of optically trapped upconverting nanorods by in situ single-particle polarized spectroscopy," Nanoscale 8, 1 (2015).

4. V. K. Jagannadh, M. D. Mackenzie, P. Pal, A. K. Kar, S. S. Gorthi, "Slanted Channel microfluidic chip for 3D fluorescence imaging of cells in flow," Opt. Express **24**, 22144-22158 (2016).

5. M. D. Mackenzie, K. I. Ciałowicz, C. Hamilton, K. J. Martin, R. S. Saleeb, L. Paterson, R. R. Duncan, and A. K. Kar, "Femtosecond Pumped Biological Laser for Use in Fluorescence Studies," Submitted to Scientific Reports.

Conferences by the author

1. M. D. Mackenzie, D. Choudhury, L. Paterson, R. R. Duncan and A. K. Kar, "Femtosecond Pumping of eGFP transfected Human Embryonic Kidney Cells," CLEP-PR & OECC/PS 2013, Kyoto, Japan, Poster WPJ-2 (2013).

2. M. D. Mackenzie, D. Choudhury, L. Paterson, R. R. Duncan and A. K. Kar, "Femtosecond Pumping of Human Embryonic Kidney Cells Transfected with Enhanced Green Fluorescent Protein," AIPT Conference (2013).

3. M. D. Mackenzie, B. Rosal, D. Jaque and A. K. Kar, "Effects of flow rate on heating inside microfluidic devices," Biophotonics symposia, Photon 14, London, UK (2014).

4. V. K. Jagannadh, M. D. Mackenzie, P. Pal, A. Kar and S. Gorthi, "Optofluidic Microscopy Using Femtosecond Micromachined Glass Microfluidics," Photonics 2014, Kharagpur, India, T3A.6 (2014).

5. M. D. Mackenzie, C. Hamilton, R. Duncan and A. Kar, "Femtosecond Pumped Biological Laser," Photonics West, SPIE BiOS 9341-11 (2015).

6. A. K. Kar, M. D. Mackenzie, K. I. Cialowicz, R. S. Saleeb and R. R. Duncan, "Vitamin C for stabilising biological lasers," Photonics West, SPIE BiOS 9711-42 (2016).

7. M. D. Mackenzie, A. Bhide, P. Pal, M. Varma, A. K. Kar and L. Paterson, "Photoreduction of Silver Nanoparticles in Glass to Create SERS Microfluidics for Enhanced Molecular Sensing," Marine Microbiome Discovery & Innovation (2016).

Contents

List of Figures

List of Abbreviations

BBO	β-Barium Borate
DAPI	4',6-diamidino-2-phenylindole
DMEM	Dulbecco's Modified Eagle Medium
DMSO	Dimethyl Sulfoxide
EBSS	Earle's Balanced Salt Solution
eGFP	Enhanced Green Fluorescent Protein
FITC	Fluorescence Isothiocyante
FRET	Förster Resonance Energy Transfer
GFP	Green Fluorescent Protein
HEK293	Human Embryonic Kidney Cells 293
HF	Hydrofluoric Acid
IISc	Indian Institute of Science
KOH	Potassium Hydroxide
OPA	Optical Parametric Amplifier
PDMS	Polydimethylsiloxane
PEEK	Polyether Ether Ketone
ROS	Reactive Oxygen Species
SEM	Scanning Electron Microscope
SERS	Surface Enhanced Raman Spectroscopy
SLM	Spatial Light Modulator
STED	Stimulated Emission Depletion
ULI	Ultrafast Laser Inscription
WT-GFP	Wild Type Green Fluorescent Protein

1. Introduction: Microfluidics and Biological Lasers

1.1 Development of the Laser

The laser can perhaps be viewed as one of the defining achievements of physics in the 20th century. It is unique in how widely it has been adopted in the sciences, everyday life and public recognition of its impact on society. First proposed by Albert Einstein in 1917 it remained only a concept until Theodore Maiman demonstrated the first Ruby laser in 1960 [2].

Laser light is distinct from that available from other sources in that it is highly coherent and monochromatic and the many uses this enables has led to massive research and development of laser sources. Briefly their high coherence allows laser beams to propagate over large distances with low divergence and to be focused tightly with applications in areas such as range finding and microscopy. Their narrow wavelength emission leads to high signal to noise ratio and low dispersion enabling applications such as fibre optic telecommunications.

Lasers can be operated in a number of ways. The 'basic' continuous wave laser emits a constant stream of light. An example of this which is widely used is the HeNe laser, common in teaching and experimental labs. It is relatively cheap to produce emitting light at 633 nm among other wavelengths. Q-switching involves changing the cavity loss of a laser allowing for a higher population inversion before lasing occurs and a pulsed emission with high peak powers. Mode locking techniques including saturable absorbers, acousto optic modulators and Kerr lensing can be used to produce ultra-short laser pulses by forcing a laser's longitudinal modes to oscillate in phase with each other interfering to create a single pulse as short as a few femtoseconds.

1.1.1 Use of lasers in biology

There has been a large scale adoption of lasers in a variety of biological applications. They can be used for cutting and ablating in surgery as an alternative to traditional scalpels allowing for a contact free, and therefor sterile cut. In research they can be used for fluorescence imaging, multi-photon excitation, Raman, confocal microscopy and optical transfection, creating a temporary hole in their membrane which then self-heals

[3]. This has the advantage over other methods of being relatively non-invasive and selective.

The optical trapping of cells using a highly focused laser beam gives the ability to move a cell in three dimensions either to position it with respect to others or to separate it from a population by moving it into a separate region of a microfluidic device or a micro capillary which can then be removed from the sample.

1.1.2   The Laser and Material Processing

One of the largest areas of adoption for the laser in industry has been for material processing; cutting, welding and patterning of materials. A commonly used laser for these applications is the CO_2 laser. First produced in 1964 and emitting in the 10 µm region it is also used in research. It also has some medical applications due to its strong water absorption.

The processing of materials using ULI using femtosecond lasers is a current area of research and used throughout this thesis to fabricated a range of photonic and microfluidic devices. Laser ablation, which can fabricated sub-micron surface features, was first demonstrated in 1994 [4] but while this is impressive, the modification is limited to the surface. Sub surface modification can be inscribed by focusing a femtosecond laser into a transparent media. At the focus of the beam the high peak intensities cause material modification the specifics of which are described in chapter 2. The potentially induced modifications are a change in refractive index, used for creating waveguides, nano-gratings, used for selective chemical etching and voids. Compared to alternative methods of manufacturing, such as lithography, ULI allows for 3D fabrication and rapid prototyping without the need for clean room facilities.

One of the main uses of ULI in laser research is the fabrication of compact waveguide lasers [5]. This is especially useful in materials which cannot easily be drawn into fibres of sufficient quality to form a fibre laser [6]. ULI waveguide devices can take advantage of the 3D capabilities of ULI to fabricate structures which would not be possible, or difficult, through other methods. One such example is surface waveguides where the waveguide is brought to the surface of the device to enable evanescent coupling to samples places on the surface, useful for sensing applications [7]. More novel devices developed using ULI include the photonic lantern which converts between single and multimode fibres with applications in telecoms for achieving high data rates [8]. The

combining the laser writing of waveguides with other types of structure inside substrates to form microfluidic devices is covered in the next section.

1.1.3 Microfluidics

Microfluidics is an area of research focused on techniques to miniaturise medical and biological diagnostics with the aim of improving throughput, decreasing required sample volumes and reducing costs. It is an expanding field with an increasing number of publications each year [9]. Two of the most widely used methods of creating microfluidics are 1. lithography in Polydimethylsiloxane (PDSM) and 2. ULI followed by selective chemical etching. In this thesis we focus on ULI methods of microfabrication where by carefully selecting laser parameters it is possible to fabricate nano-cracks in some materials [10] which can be etched to create microchannels. The advantage of ULI microfluidic manufacturing over other forms of production is that it allows for 3D fabrication, fast prototyping and does not require clean room facilities. While the devices presented in this thesis are fabricated in fused silica glass it is possible to create devices in a variety of glasses, crystals and plastics [11, 12].

Integrating both microfluidic channels and waveguides inside substrates allows for the combination of laser illumination and samples to fabricate a wide variety of devices. This can be used for simple illumination of a sample for fluorescence excitation [13] or heating of a sample. Alternatively, it is possible to use waveguides to deflect [14], trap, count [15] and stretch cells through the use of dual counter propagating waveguides [16]. Many traditional optical components such as mirrors and interferometers can be miniaturised and integrated into microfluidics [17, 18] resulting in smaller more rugged diagnostic methods.

An interesting area of microfluidics is high speed cell sorting to separate cells from a population. Traditional cell sorting requires large expensive equipment limiting availability. Microfluidic cell sorting has been shown using imaging to identify cells before selecting which output they go to using a laser to divert them from a population [19]. Another method of cell sorting is to use their deformability. Small channels with a pressure difference along them only allow cells of a certain size or deformability to pass through [20]. This can be used to separate different types of cell or potentially identify diseased cells as their deformability can change based on health.

Using the 3D capabilities of ULI it is possible to expand on the abilities of other forms of fabrication. An example of this is flow focusing which has been demonstrated in PDMS devices in 2D where two streams of liquid compress a third between them to confine a sample in a narrow, useful for droplet generation [21]. Using ULI it is possible to fabricate a 3D flow focusing device where 4 streams of liquid surround a central 5th confining it in both the horizontal and vertical directions keeping the sample away from the channel surfaces [15]. This is useful both for reducing damage to cells from channel walls and confining their freedom of movement making focusing with microscopes or targeting with embedded waveguides easier.

1.1.4 Fluorescent Dyes and Proteins in Biology

Green Fluorescent Protein (GFP) has enabled a revolution in biological imaging leading to a Nobel Prize awarded in 2008 for those involved in its discovery and development, Osamu Shimomura, Martin Chalfie and Roger Tsien. The protein was discovered by Osamu Shimomura through a long term study to discover the mechanism by which the jellyfish *Aequorea Victoria* emits bioluminescence [22]. He carried out his work between the 1960s and 80s in which time he caught hundreds of thousands of jellyfish to discover that their florescence depends on two light emitting proteins. The first, Aequoren, emits blue light when exposed to calcium and the second, GFP, which emits green light when pumped with blue. Energy is transferred between the two through a non-radiative process leading to the jellyfish emitting green light.

The idea that GFP could be transfected into other organisms was first proposed by Douglas Prasher and in collaboration with Martin Chalfie they successfully demonstrated this [23]. By attaching fluorescent proteins to areas of interest inside cells it is possible to image them and gain information about the processes occurring inside them. Wild Type Green Fluorescent Protein (WT-GFP) has proven to be very modifiable leading to the development of a large variety fluorescent proteins emitting throughout the visible spectrum for multicolour imaging [24]. Other developments include proteins whose emission gives information about cells as their emission varies with properties like pH or calcium levels. More novel developments are proteins which are photoactivatable or designed to kill cells by deliberately creating Reactive Oxygen Species (ROS).

There is a fundamental limit to the resolution of optical microscopes and for a time it was thought this would never be overcome. The development of super-resolution fluorescence

microscopy techniques has led to another revolution in biological imaging as well as another Nobel Prize awarded in 2014 to Eric Betzig, Stefan Hell and William Moerner. These fluorescence techniques include Förster Resonance Energy Transfer (FRET) and Stimulated Emission Depletion (STED) microscopy. In FRET two different fluorescent proteins of are linked with a variable spacing. As they move closer together non radiative energy transfer between the two alters the emission wavelength allowing this ratio to be used as a 'molecular ruler'. STED relies on the fact that for a single point source it is possible to determine its location statistically by taking a large number of measurements and averaging them. Various methods are used so that in a population of fluorophores only a small number are activated at any one time such as reducing pump power or using a higher energy to temporarily deplete them.

Fluorescent proteins can be used as a laser gain medium in a similar way to dye lasers. This was first demonstrated in 2002 using WT-GFP in solution between two plane mirrors pumped with a Ti:Sapphire laser at 790 nm through two photon absorption [25]. The first living laser, defined here as a biological cell containing a gain medium, was demonstrated in 2011 by Gather and Yun [26] using Human Embryonic Kidney Cells (HEK293) transfected with eGFP. They placed the cells between two plane mirrors and pumped with nanosecond pulses from an Optical Parametric Amplifier (OPA) at 465 nm. The lasing did not damage the cells and multiple modes were observed in the emission. Biological lasers have potential as a tool for examining cells through enhancing signal to noise in experiments and the examination of the emitted modes which may give information about cell shape and health.

1.2   Thesis Outline

The work reported in this thesis was carried out by the student over the course of three years as part of EPSRC funding. A brief description of each chapter is given below.

Chapter 2

An overview of the theory needed for this thesis will be given focusing on the areas of ULI The inscription of waveguides and creation of microfluidic devices through selective chemical etching is covered, as is fluorescent proteins, dyes and the necessary laser physics to create a living laser.

Chapter 3

Temperature sensing inside a microfluidic device was achieved using the fluorescence emission ratio between Rhodamine B and 110. This chapter will describe the fabrication of the device used and what the results reveal about the temperature distribution inside microfluidic devices.

Chapter 4

A multi-channel flow cytometer was fabricated using ULI and selective chemical etching for the imaging and counting of cells with the aim of improving the speed and availability of current diagnostic methods. The device will be described as well as the experiments conducted using whole blood and yeast cells.

Chapter 5

The emission of NaYF4:Er^{3+},Yb3^{+} upconverting nanorods was shown to have polarised emission allowing their orientation to be determined using a polariser and spectrometer. This technique was investigated by constructing a duel beam optical trap to position the nanorods. This has applications in biological sensing.

Chapter 6

Biological lasers were created using both fluorescent dyes and proteins. This section will detail the laser cavities used and their performance. Additional experiments were conducted to look at improving the lifetime of the laser using vitamin C and calcium sensing which may be used to improve the detectability of changes in fluorescence compared to current fluorescence techniques.

Chapter 7

Chapter 7 will offer concluding remarks on the work conducted in this thesis and thoughts on potential future work.

1.3   Summary

The recent development of a living laser shows that despite the field of laser physics being over 50 years old it is still possible to come up with new innovations. In this thesis we

examine how such a laser can be used in biological research to enhance current methods of examining cells.

One of the largest applications of lasers has been in material processing where their high peak powers provide unique abilities in welding, cutting and patterning. ULI uses the high peak power and short pulses of femtosecond lasers to modify transparent materials at a scale not possible through traditional methods. We have used this technique to fabricate several devices in which novel sensing capabilities have been explored, for example temperature sensing and flow cytometry.

Both these areas of research stem from the first demonstration of the laser by Theodore Maiman in the 1960s. His work has led to the development of a whole field of scientific study with applications in research, medicine, manufacturing and in peoples' everyday lives, as well as this thesis, for which the author is grateful.

2. Review: Microfluidic Devices and Living Lasers

Working in the area of biophotonics requires a researcher to gain knowledge spanning the fields of both physics and biology in order to be successful. This review section will cover topics including the use of femtosecond lasers to modify bulk glasses producing nano scale modification as well as the creation of biological lasers.

2.1 Ultrafast laser inscription

Glass is a uniquely useful material which has been used for millennia for the creation of decorations, containers and windows. Since the beginning of the fields of science and medicine it has been used to contain materials and perform reactions due to its properties such as being non-reactive with most chemicals, optically clear and the ease with which it can be moulded into different shapes. With the development of microfluidic devices for use in diagnosing and studying disease we would like to use glass as our construction material for the reasons given above. This requires new methods of fabrication as the traditional ways of shaping glass such as glass blowing, mechanical drills and saws fail at the micro and nano scale.

A method of modifying materials at these scales is ULI. In ULI an ultrafast laser, with femtosecond scale pulse length, is focused into a material which is transparent to the laser wavelength. Due to the high irradiance at the focus the pulses are absorbed through multi photon processes leading to changes in structure. These changes can be used to produce waveguides for guiding light or etched with acid to fabricate microfluidic channels. The advantage of ULI over other methods of producing microfluidic devices is that it has the ability to work in 3 dimensions, does not require a clean room and can be rapidly modified as it works without the use of masks like in lithography.

ULI has been used to fabricate waveguide lasers operating in the infrared and environment sensors. Microfluidic cell sorters and lasers have been shown. Our work, presented in this thesis, focuses on using ULI to produce fused silica microfluidic devices for temperature sensing and flow cytometry. The following sections will examine the theory relevant to fabricating such devices.

2.2 Energy Transfer

From everyday experience we know that when a beam of light falls upon a surface there are several possibilities. The light may be reflected like on a mirrors surface, it may scatter like with paper, it may be absorbed leading to heating of the material or fluorescence and lastly it may be transmitted unaltered. The high peak powers of lasers allow for another option. When an ultrafast laser pulse is focused into a material transparent to the laser wavelength it can still be absorbed, despite having photon energy less than the bandgap of the material, through multi photon processes.

An electron can absorb multiple photons, each with energy less than the bandgap, moving from the valance band to the conduction band through intermittent virtual energy levels. Alternatively, the high irradiance of the laser pulse may distort the electric field of the material allowing for an electron to tunnel between bands. These processes of photoionisation are illustrated in *Figure 2.1* as well as an intermittent process which is a combination of the two.
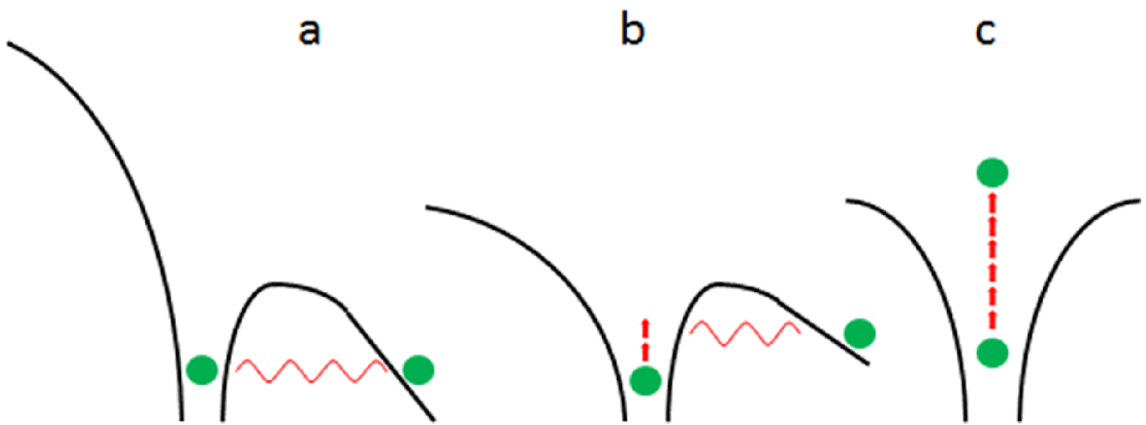
Figure 2.1: Possible methods of photoionisation of an atom when exposed to femtosecond pulses. a) the electron tunnels through the potential energy barrier, b) a combination of multiphoton absorption and tunnelling and c) multi photon absorption.

The likelihood of an electron being ionised out of the valance band by either multi photon absorption or tunnelling is given by the Keldysh parameter [27], *Equation 2.1,* where γ is the adiabatic parameter, ω the laser frequency, e charge of an electron, m_e the mass of an electron, c speed of light, n_0 refractive index, ε_0 permittivity of free space, E_g the band gap of the material and I the laser intensity. When this value is smaller than 1.5 tunnelling processes will be responsible for most ionisation, above 1.5 multi photon absorption and

for around 1.5 a mixture of processes will occur. The laser systems and parameters used in our work give a γ of ~ 1, a combination of both tunnelling and multi photon absorption processes.

$$\gamma = \frac{\omega}{e} \sqrt{\frac{m_e c n_0 \varepsilon_0 E_g}{I}} \qquad\qquad \text{Equation 2.1}$$

An electron liberated from its parent atom may gain energy through the mechanism of inverse bremsstrahlung where it must simultaneously absorb a photon and collide with an atom for conservation of energy and momentum to be maintained [27, 28]. Avalanche ionisation where these electrons strike atoms liberating more electrons which in turn gain more energy results to an exponential increase in free electrons and energy absorbed from the laser pulse. This avalanche ionisation requires the laser pulse length to be of sufficient duration that several iterations of photon absorption and impact ionisation can occur absorbing the pulse energy. If it is very short, less than 10 fs [4], the pulse passes through the focal volume before a large percentage of its energy can be depleted. As the initial photoionisation that seeds avalanche ionisation does not depend on defects being present in the material the process is position independent leading to consistent results throughout.
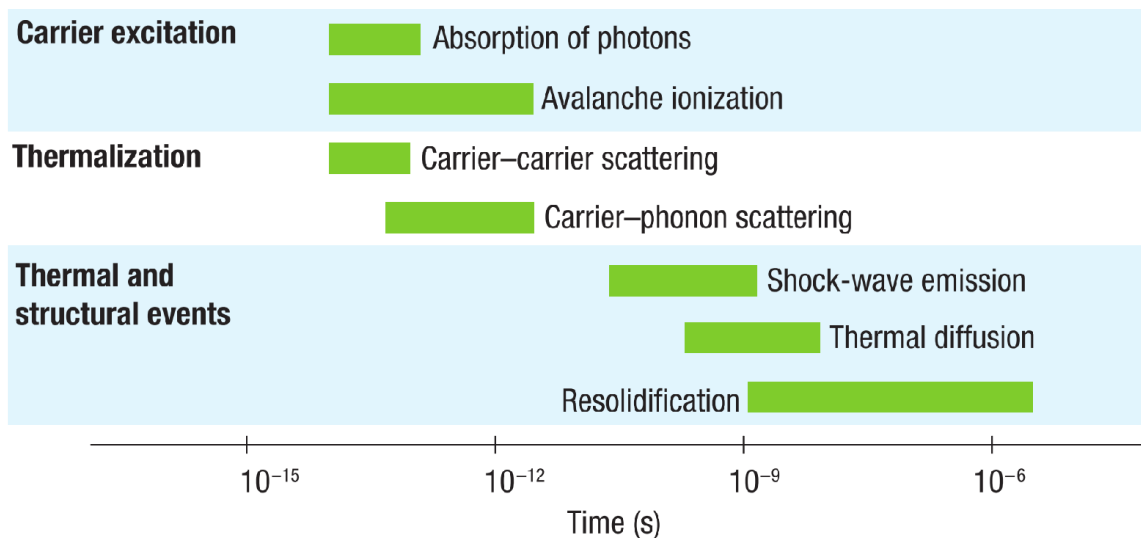
Figure 2.2: Time taken for various energy transfer mechanisms to occur in ULI. [4]

The energetic electrons excited by the laser collide with each other and with atoms within the focal volume distributing energy between themselves. This process occurs over the space of around 1 ps before other processes dissipate the energy as shown in *Figure 2.2*.

10

Over several ns a shockwave is emitted from the excited core and thermal energy diffuses outwards. If the laser pulse imparts enough energy to melt the material it may leave behind modifications when it re-solidifies such as stress, the relocation of dopants or changes in the structure of molecules.

In fused silica there are 3 type of modification possible dependent on laser pulse energy and length among other parameters as illustrated in *Figures 2.3* and *2.4*. The first type of modification, which starts at pulse energies of 50 nJ and pulse lengths of 40 fs, is a smooth change in refractive index. For slightly higher pulse length or energy nanogratings are formed. These are useful for fabricating microfluidic devices as they show faster etching than unmodified fused silica. The third type of modification which occurs at higher still pulse lengths and energies is a mixture of voids, nanogratings and smooth modification.

While refractive index modification and voids may be expected after exposure to the laser the formation of nanogratings is more interesting and difficult to explain. The initial laser pulse ionises the atoms in the focal volume leading to an electron plasma. This then interferes with further pulses to create nanogratings perpendicular to the laser polarisation [29-31].
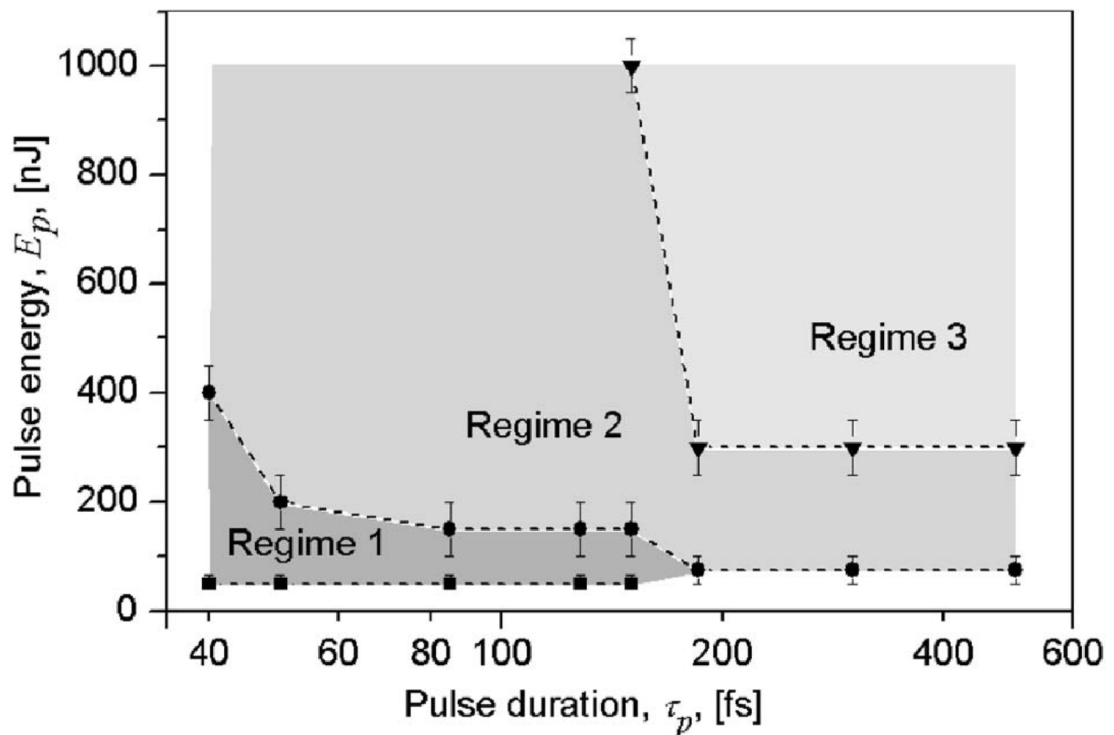
Figure 2.3: Etching regimes in fused silica. Regime 1) smooth modification, 2) Grating formation and 3) Mixed modification containing smooth modification and gratings. [10]
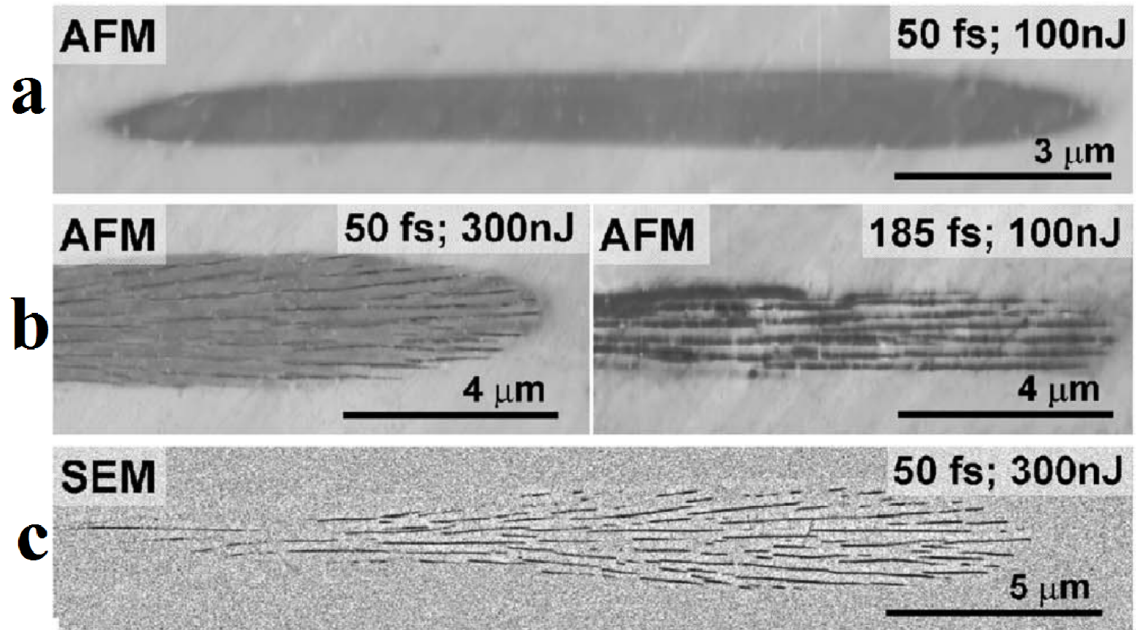
Figure 2.4: Etching regimes in fused silica. Regime a) smooth modification, b) Grating formation and c) Mixed modification containing smooth modification and gratings. [10]

2.3 The Writing of ULI Devices

In our work two laser systems were used to preform ULI. Both are femtosecond ytterbium fibre lasers; an IMRA μ-Jewel and a Fianium HE-1060-1J. Both lasers have variable repetition rate and pulse width as given in *Table 2.1*. As discussed in section 2.2 changing laser pulse energy, pulse length and polarisation alters the type of modification seen. Other parameters which influence modification are repetition rate, wavelength, objective NA, pulse front tilt, repeat scans and translation speed. This large number of variables makes finding optimum inscription parameters difficult, requiring large parameter scans.

Parameter	IMRA μ-Jewel	Fianium HE-1060-1J
Central Wavelength	1047 nm	1064 nm
Pulsewidth	≥350 fs	≥300 fs
Repetition Rate	0.1-5 MHz	≤1 MHz

Table 2.1: Selected parameters for the two femtosecond lasers used for manufacturing ULI waveguides and microfluidic devices.

Pulses from the lasers were focused into a sample mounted on air baring stages produced by Aerotech to allow positioning in 3 dimensions relative to the laser beam. These were ABL10100 linear stages and an AVL125 vertical stage with repeatability in positioning

of 50 nm and 300 nm respectively. The high positioning accuracy is required for fabricating microfluidics and waveguides as it determines the smallest features which can be produced.

To control the laser power and polarisation incident on the sample the control optics shown in *Figure 2.5* were used. A half waveplate and polarising beamsplitter for attenuating the beam followed by a half and quarter waveplate to give linear polarisation in a given direction or circular polarisation. A small amount of power was picked off from the beam to monitor the power and calibrated before each run. For switching the beam on and off, a high speed shutter with an open/close time of 1 ms was used. The beam is then focused into the sample through an objective.
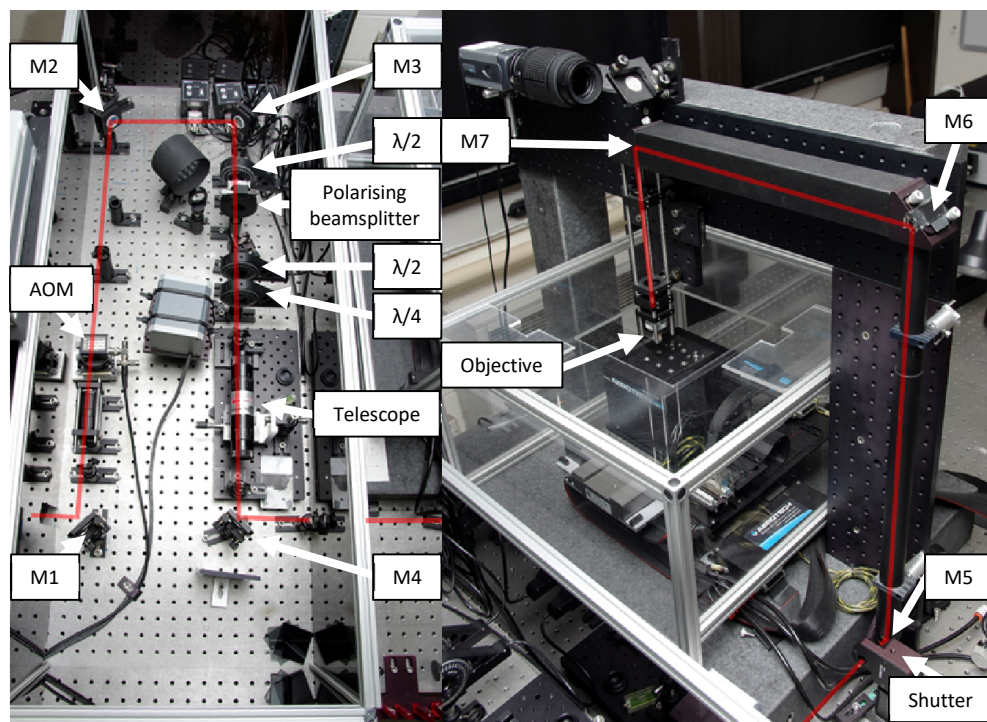
Figure 2.5: ULI inscription rig consisting of a femtosecond laser, polarisation control optics and an objective positioned above accurate translation stages.

Instead of translating the sample relative to the laser beam it is possible to translate the laser beam relative to the sample using a spatial light modulator (SLM) or deformable mirror [32]. This has the advantage of requiring less investment and allowing for beam shaping but at the downside of only being able to modify material in a small area.

2.4   Waveguides

The refractive index modification induced by ULI can be used for the writing of optical waveguides to guide light either for use as waveguide lasers or for the fabrication of optical devices. Both positive and negative changes in refractive index are obtainable depending on the material and inscription parameters used. For positive changes the modified region forms the core of the fibre while for negative it can form the cladding. Waveguides can be written in either the transverse or longitudinal direction as shown in *Figure 2.6* depending on how the material is translated relative to the laser.
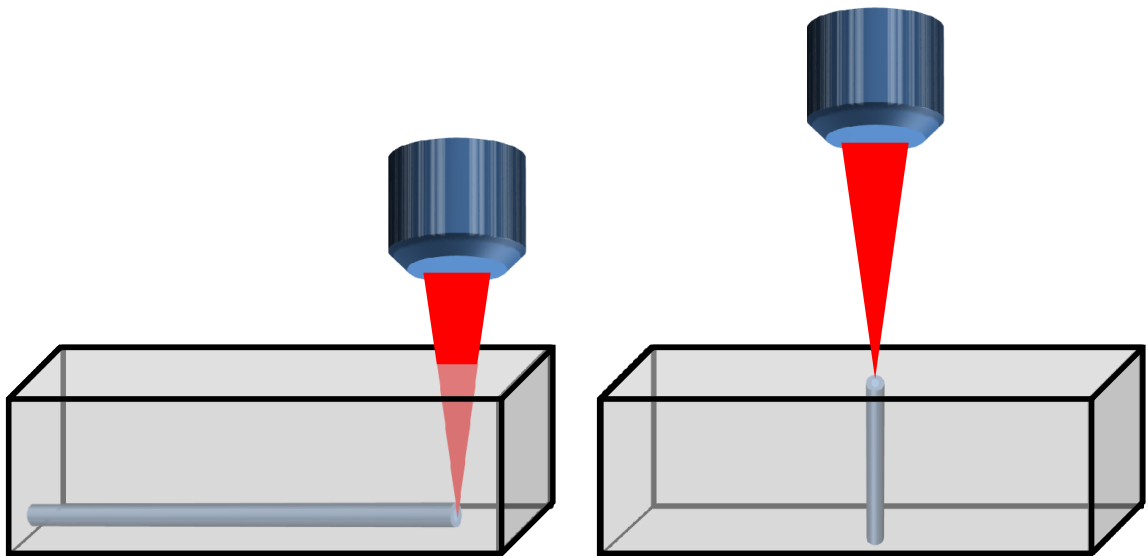
Figure 2.6: The two methods of inscription left, transverse and right, longitudinal.

The number of modes which can be supported in an optical waveguide is indicated by the V number, given by *Equation 2.2*, where the cut off for a single mode is 2.405. Values above this will support multiple modes. λ is the wavelength, a the radius of the waveguide and n the refractive index in the core and cladding. As an example in fused silica the refractive index is 1.45 and a modification of it 5×10^{-3} is achievable. For a wavelength of 980 nm this gives a cut off radius of 3.1µm.

$$V = \frac{2\pi}{\lambda} a \sqrt{n_{core}^2 - n_{cladding}^2}$$ Equation 2.2

For waveguides to have the same number of modes in the horizontal and vertical directions they must be symmetric. The circularity of the modified region is determined

14

by the NA of the objective lens used for inscription and will not typically be high enough to produce a circular modification. As an example this can be shown for a 1047 nm laser beam in fused silica, n=1.45, using *Equations 2.3* and *2.4* where Z_R is the Rayleigh length, w_0 the beam waist and λ the wavelength. Setting Z_R equal to w_0 gives a required NA of 1.9. The highest NA which can propagate in a given material is equal to its refractive index making this impossible for fused silica.

$$z_R = \frac{\pi w_0^2}{\lambda}$$

Equation 2.3

$$2w_0 = 1.22 \frac{\lambda}{NA}$$

Equation 2.4

This is only an issue for transverse modification where the horizontal dimension of the waveguide cross section is determined by the beam waist and the vertical component by the Rayleigh length. For longitudinal modification both the vertical and horizontal dimensions of the waveguide cross section are determined by the beam waist. To correct for the astigmatism in transverse waveguides several methods have been devised.
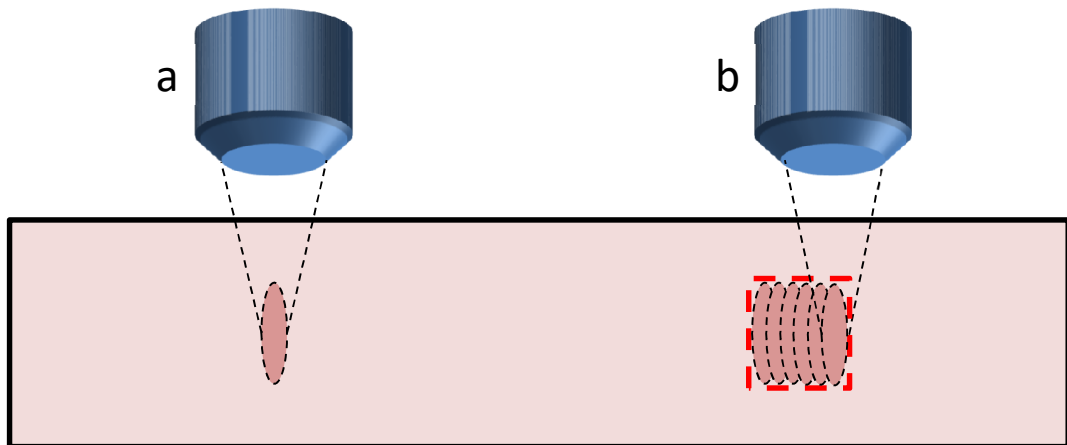
Figure 2.7: Multiscan inscription in a glass to fabricate square waveguides. a) single scan with an oval shape and b) showing the combination of scans to fabricate a square waveguide.

The multiscan method involves writing multiple lines of modification in parallel as illustrated in *Figure 2.7*. Changing the power therefore selects the height of the waveguide and the number of scans the width. A single mode waveguide will not necessarily be symmetric in both dimensions as the refractive index modification will be higher at the

centre of the laser focus than at the edges. This method requires precise stages with sub µm control of positioning.

By shaping the input beam it is possible to alter the ratio of astigmatism between the horizontal and vertical directions in the focal spot. This can be achieved using either a slit [33] or a pair of cylindrical lenses [34]. The lenses have the advantage over the slit method of not reducing the laser power.

2.5 Selective Etching

Acids have been used to pattern glass for hundreds of years to produce frosted glass windows or decorations. The acid most commonly used for this, and in our work, is Hydrofluoric Acid (HF) which etches glass through the process given in *Equation 2.5*. It is one of the more dangerous acids which can be worked with, requiring specialist containers and safety equipment, but is one of the few acids which can etch fused silica at a high rate.

$$SiO_2 + 6HF \rightarrow H_2SiF_6 + 2H_2O$$
<div align="right">Equation 2.5</div>
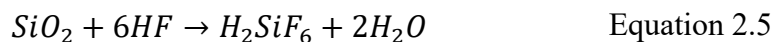
Materials exposed to femtosecond pulses and modified by ULI may be weakened leading to faster etching when exposed to acid compared to unmodified material. This effect alone in fused silica is not sufficient for fabricating detailed microfluidic devices. For such work we use the inscription of nanograting structures which give much better selectivity as acid travels along the cracks. As the nanogratings are written perpendicular to the direction of laser polarisation then the direction of etching must also be perpendicular to achieve the highest etch rate. *Figures 2.8* and *2.9* show how the etch rate varies with both pulse energy and polarisation. For low pulse energies all polarisations give the same etching as this is below the threshold for nanograting formation. At slightly higher energies nanogratings are formed and a large increase in etching is observed for nanogratings parallel to the direction of etching. Very high pulse energies sees the etch rate for all polarisations increase as the material begins to ablate allowing the acid to flow along the modified regions. Selective etch rates of up to 280 times are achievable allowing for the fabrication of detailed microfluidic devices [35].
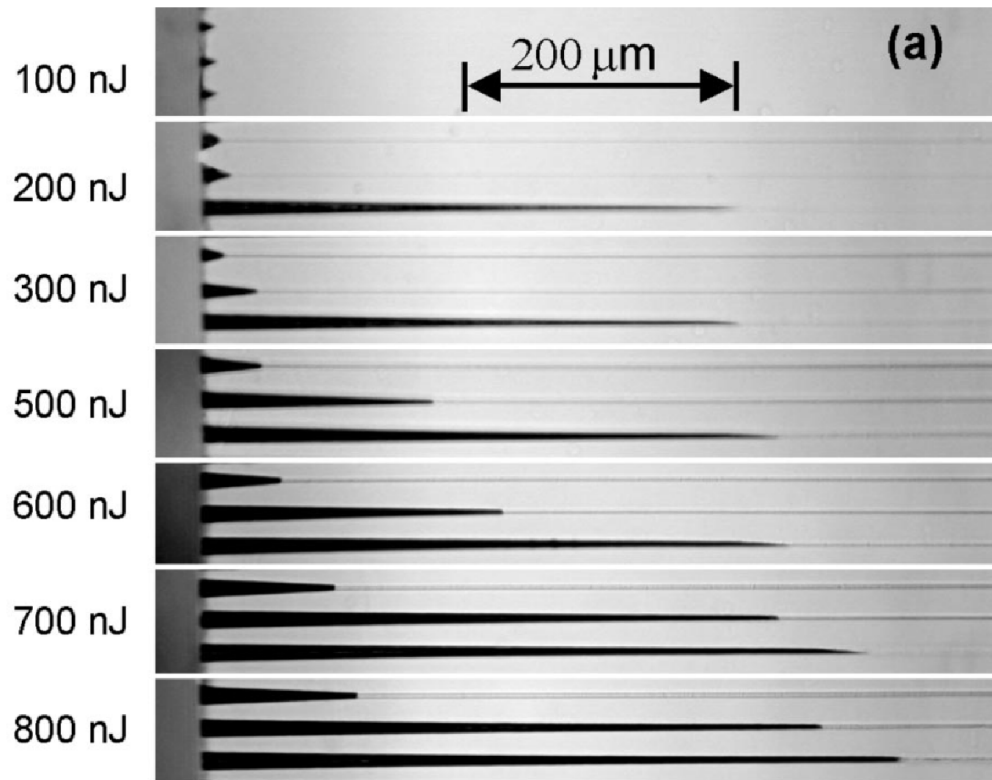
Figure 2.8: Polarisation dependent etching in fused silica. In each image from top to bottom the polarisation orientation is 0°, 45° and 90° relative to the vertical axis. [35]
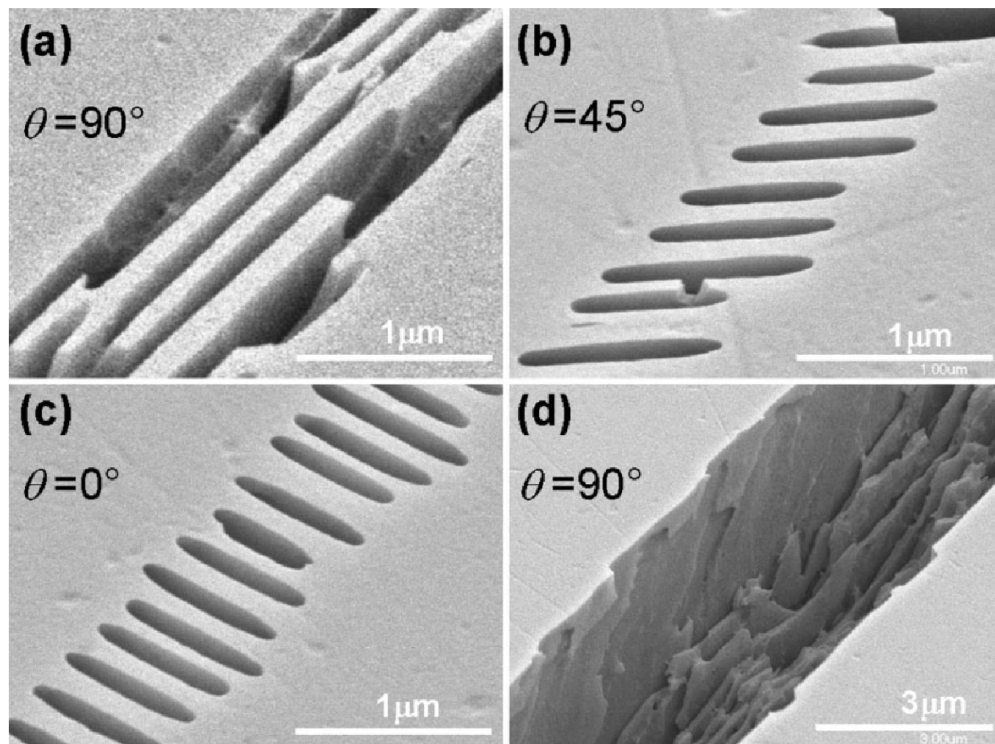
Figure 2.9: SEM images for different inscription polarisations after exposure to HF in order to expose their features. For (a),(b) and (c) the inscription pulse energy was 300 nJ. For (d) the pulse energy was 900 nJ. [35]

Etching selectivity is important as it determines the size of microfluidic device which can be fabricated and therefore how many structures can be included. This is due to the fact that all etching begins at the surface of the device and works inwards. As the channels nearer the surface are exposed to acid for longer than those in the middle they will etch more and in extreme cases may even breach the surface of the glass chip. If all that is required is straight channels then it is possible to write a modification which diverges as it moves inwards from the surface. Thus this divergence balances with the exposure time giving straight channels at the expense of having a larger feature size in the centre of the device.

Alternative etchants to HF such as Potassium Hydroxide (KOH) allow for higher selectivity at the expense of slower absolute etch rate. By using both etchants, in separate steps, it is possible to have both high etch rates and fine detail assuming small structures are only required in the centre of the device. KOH does not have as many safety considerations as HF but requires a heated bath for etching. Etching with any substance benefits from being conducted in a sonic bath as this aids with both dislodging material inside the device channels and replenishing the etchant inside them.

After etching, channels will have a rough surface as can be seen in *Figure 2.9 (d)* both inside the channel and on the surface of the unmodified glass. This is due to the inhomogeneous cracks induced in the glass but also from imperfections already present due to the manufacturing processes, either formation, cutting or polishing [36]. This roughness can be reduced through the process of annealing where the glass is slowly brought up to the softening point, 1,700 °C for fused silica, then back down. This typically requires a pottery oven.

2.6   Fluorescent Proteins and Dyes

The history of the microscope stretches back thousands of years starting with the focusing of light through water in ancient times. The first optical microscopes developed in the 17 hundreds allowed scientists to examine the microscopic world for the first time leading to advances in all areas of biology and medicine. Since this time there has been a drive and a demand to improve the resolution of microscopes with improvements in optics and illumination.

There are two issues with imaging cells which can be addressed with fluorescent dyes and proteins. The first is that cells generally are transparent to light with only changes in refractive index giving definition to their different features. By attaching a fluorophore to specific areas of a cell, for example staining the cytoskeleton, these features can be seen and if multiple colours are used a uniform cell becomes a multi-coloured well of information. The second issue is a fundamental one, the diffraction limit, a limit on the smallest feature which can be resolved with a given wavelength of light and objective. For 488 nm light and a 1.3 NA objective this is ~0.2 μm; much smaller than the typical size of a cell but much larger than what would be required to examine the smallest features of a cell or its proteins. Fluorescence imaging techniques, using genetically engineered fluorescent proteins, allow for the diffraction limit to be overcome.

Apart from direct improvements in spatio-temporal imaging through the labelling of cells and resolution through breaking the diffraction limit there have been other developments in sensing which utilise fluorescent dyes and proteins. Some have been modified to react to a cells internal environment, for example its calcium levels or pH, changing either their emission wavelength or intensity allowing for these properties to be monitored. Other modifications allow for dyes to act as viability markers, by only being activated when passing through a functioning cell membrane, or to deliberately kill cells when exposed to light.

Fluorescent dyes have been used as laser gain media for decades in laser laboratories as broad band visible laser sources. More recently fluorescent dyes and proteins have been shown to lase inside biological cells giving the prospect of adding to the above methods of looking at cells. As part of this thesis has worked towards creating living lasers using fluorescent dyes and proteins as the gain media the following sections will be used to set out how these media were discovered and developed [22, 26, 37].

2.6.1 Fluorescent Proteins

With the discovery of GFP by Osamu Shimomura [22] and the demonstration that it could be transfected into other organisms [23] a whole field of biological imaging was born (Nobel Prize in chemistry 2008 to Osamu Shimomura, Martin Chalfie and Roger Tsien). While WT-GFP was the first fluorescent protein discovered efforts made to find more have been successful with others being found in corals, jellyfish, amphioxus, and

copepods. It is suspected that all these proteins share a common origin rather than being the result of convergent evolution [38].

An interesting feature of WT-GFP is that it has two absorption peaks, one at 395 nm and a second lower peak at 475 nm, while emitting with one maximum at 509 nm. This is due to a non-radiative process, excited state proton transfer, where energy from the 395 nm peak is transferred to the 475 nm peak before emission.

All fluorescent proteins share a common shape with a central chromophore surrounded by an outer β-barrel which protects it from damage and interaction with the outside environment. *Figure 2.10* shows this with the outer amino acids represented as ribbons. As well as protecting the chromophore the β-barrel restricts its movement reducing non-radiative energy loss.

Fluorescent proteins are highly modifiable with simple changes resulting in the development of colours being available throughout the visible spectrum, enhancements in brightness and specialist abilities such as deliberately killings cells and photoactivation. The fact that a single amino acid change can be used to change the emission of WT-GFP from green to yellow [37] shows how easy it is to modify and explains why there are so many variants available today. *Figure 2.11* shows examples of the proteins available throughout the visible.

In addition to enabling multi-colour fluorescence imaging, these proteins have been used to develop a number of imaging and analysis techniques. Using photobleaching the diffusion inside a cell can be monitored or the movement of tagged molecules may be tracked. Using proteins which respond to calcium or pH levels allows for these to be monitored. They even allow for the diffraction limit to be defeated through the use of super resolution fluorescence techniques such as FRET and STED amongst others [39, 40].

Fluorescent proteins can be used as laser gain media as shown in various papers [25, 26]. In these examples, as in our work, pulsed pumping is used due to the short fluorescence lifetime of these proteins and dyes, which are on the order of a few nanoseconds [41, 42]. Pumping with pulses significantly shorter than the fluorescent lifetime has been shown to result in a lower threshold compared to nanosecond pumping for the protein DsRed due to the higher population inversion achieved before lasing occurs [43].

The use of fluorophores inside a biological cell to realise a living laser can potentially inform us of the cell's properties. A cell's size, shape and refractive index will alter the laser emission. Lasing can also potentially enhance detectability in low signal experiments as it will increase the peak emission at a given wavelength compared to fluorescence.

Figure 2.10: The structure of a fluorescent protein showing the protective outer β-barrel and inner chromophore. The specific variant is roGFP2. [37]
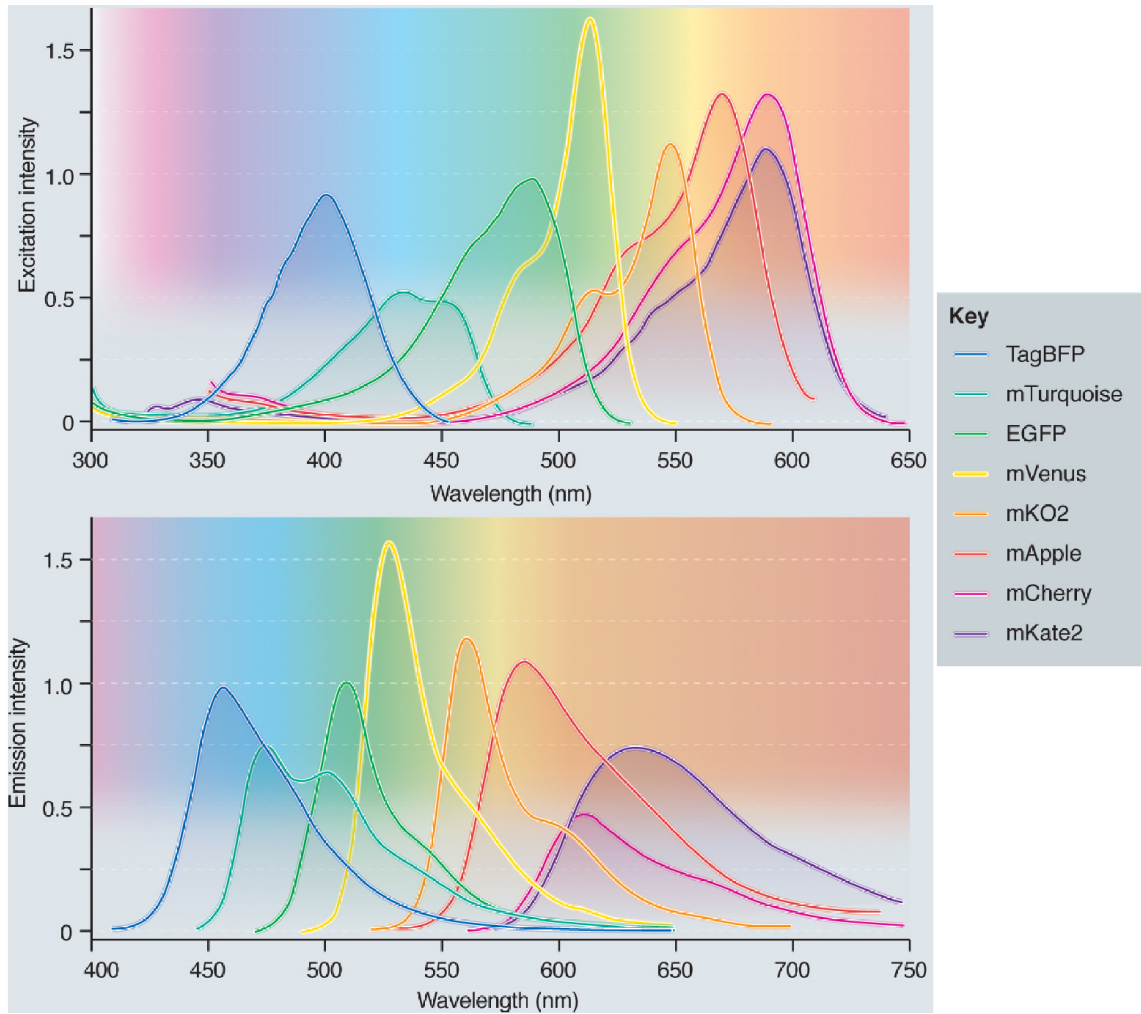
Figure 2.11: Fluorescent proteins absorption and emission spectra. [24]

2.6.2 Fluorescent Dyes

Dye lasers were one of the first types of laser to have a broad emission profile allowing for lasing throughout the visible spectrum as seen in *Figure 2.12* for one dye line produced by Life Technologies Ltd. Due to this they were widely used but have since been mostly superseded by solid state lasers because of the difficulty in employing dye jet laser systems.

Like fluorescent proteins, dyes can also be used with cells as a stain for imaging. In our work we use them as a gain media inside cells due to their high emission and ease of use compared to fluorescent proteins. Whereas the process of adding GFP to a cell can take several days, dyes can be added in under an hour.

Areas in which dye lasers are still used for research over solid state systems are those in which their liquid nature is needed. Examples of this are levitated dye droplet lasers which take advantage of whispering gallery modes within the droplets [44] and microfluidic dye lasers [45] which can be thought of as miniature versions of traditional large scale systems.
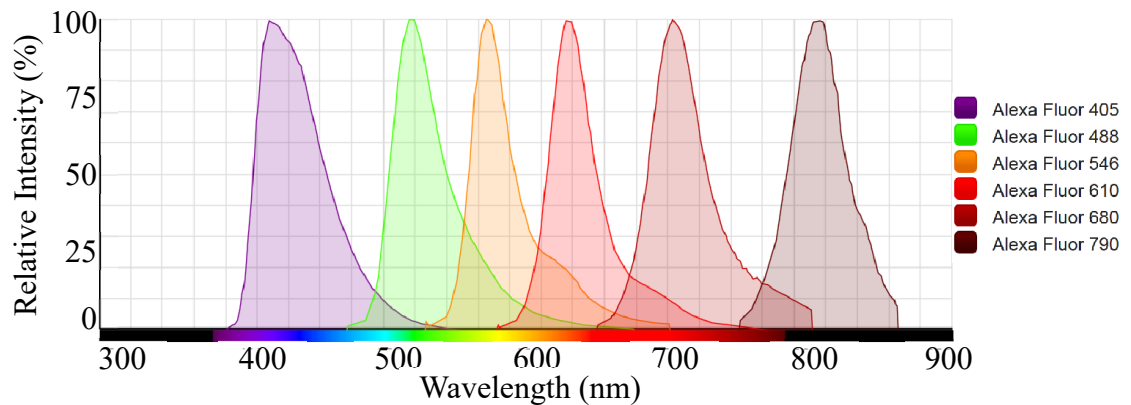
Figure 2.12: A selection of fluorescent dyes available in the Alexa line from Life Technologies Ltd.

2.7 Optical Tweezers

Researchers investigating the behaviour of cells would like to be able to pick them up and move them around. To place one cell next to another then watch and see how they interact. Unfortunately, due to the scales involved such manipulation is not easy without causing damage to the cells involved. Optical tweezers are a method by which we can manipulate micro and nanometre scale objects noninvasively. The process involves tightly focusing a laser beam onto a cell which moves towards the point of maximum intensity. The cell can then be moved in 3 dimensions resulting in the positioning we desire. This process was discovered and investigated by A. Ashkin who reported on the initial trapping [46], 3D levitation [47] and manipulation of live viruses and bacteria [48].

The method by which optical trapping works can be thought of simply as a force resulting from the divergence of light as it passes through a spherical object [49]. For a tightly focused laser beam this results in trapping in 3 dimensional as shown in *Figure 2.13*. The actual position at which the cell rests will be slightly below the focal point as there is a balance between the force the trap exerts and gravity.
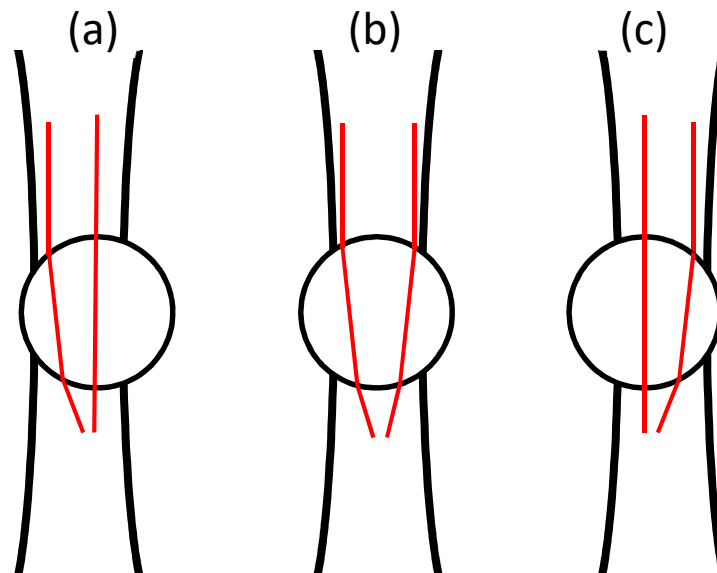
Figure 2.13: Optical trapping of a spherical particle using ray tracing. a) particle to left of trap resulting in net force to the right, b) particle in centre of trap resulting in no net force and c) particle to right of trap resulting in force to the left.

The optical trapping we have carried out in our work involved sub-micron sized particles. At this scale, smaller than the laser wavelength, the above ray method no longer applies and other explanations must be considered. For such a small particle it may be thought of as a dipole on which the electric field acts creating a gradient force drawing the particle toward the centre of the trapping beam [50, 51].

Multi-particle trapping can be used for measuring the force between particles, setting the separation for cell interaction experiments or simply positioning multiple particles at once. Splitting the trapping laser using beam splitters and steering them individually or using a diffractive optic is effective but results in power losses limiting the total number of traps. An SLM may be used to create and arbitrary number of traps by quickly swapping between traps.

In microfluidics optical traps have been constructed using embedded waveguides. As light diverges from the ends of the waveguides two are needed to form the trap, positioned opposite each other and counter propagating. The overlapping beams form a trap with a point of highest intensity between the two and particles are drawn to this point. Devices capable of rotating particles have been shown useful for imaging. By increasing the power in a dual beam trap, a cell can be stretched as a diagnostic method, because disease can affect a cell's cytoskeleton, altering elasticity [16].

2.8   Silver Nanoparticles

Raman spectroscopy is a powerful tool for the identification of molecules. It can be used to take the chemical 'fingerprint' of a substance uniquely identifying it. This has been used, for example, in the whiskey industry to check the authenticity of samples identifying fakes [52]. As Raman signals are typically weak, one of the main difficulties in taking measurements is separating the signal from that of the central laser wavelength. One way of enhancing the signal is Surface Enhancement of Raman Spectroscopy (SERS). The lasers electric field is enhanced near small metal surfaces which increases Raman signals making them easier to detect [53, 54]. Several metals provide suitable surfaces for SERS measurements including silver, gold, copper, aluminium, indium and platinum

2.8.1   Silver Nanoparticles Background

Silver nanoparticles, defined as having sizes between 1-100 nm, come in many different shapes ranging from spheres, to rods to cubes. They are widely used commercially as antimicrobials in products such as deodorants and water purification solutions but this leads to their release into the environment with questions over their effect on humans and wildlife. Evidence has shown that silver nanoparticles bioaccumulation with negative impacts on fish and other marine animals [55] as well as the potential for ill effects in humans [56].

The enhancement of Raman signals using silver nanoparticles in SERS has become a widely used technique amongst other possible substrates [53, 54]. In our work we aim to combine silver nanoparticles with 3 dimensional microfluidics to create high throughput SERS sensors. Work already conducted in this area indicates that such patterning is possible using a multi component fabrication process utilising a glass microchannel and PDMS cover [57].

2.8.2   Photoreduction

The production of silver nanoparticles can be conducted through different methods depending on the desired quantity and application. Chemical synthesis of silver nanoparticles in solution can be performed through several methods, with the one used in our work involving silver nitrate and sodium citrate heated to around 100°C being one of the simpler methods. In this process the first nanoparticles to be formed are small, these

then grow as the reaction continues. This process can be arrested by adding ammonia to the solution resulting in more uniform particle size [58]. Physical and biological methods are also available [59].

Photoreduction of nanoparticles using a focused laser beam to heat the precursor chemicals is an alternative to heating the sample. This gives the advantage of selectively creating nanoparticles to pattern a surface. Using this process in conjunction with microfluidics enables the fabrication of high throughput SERS sensors [57, 60].

2.9 Summary

Initially there was only one scientific discipline that of philosophy which over time divided into the main fields of Chemistry, Physics and Biology as it became impossible for one person to become an expert in them all. With the current trend to collaborative research it is now necessary for researchers to learn at least some things outside their main field and work with those who are experts in other disciplines. For a physicist this can be a fascinating process as we are exposed to the world of the cell and chemistry.

This theory chapter has covered various topics relevant to the work undertaken in following sections. These sections will focus on individual projects undertaken to fabricate microfluidics and lasers with the aim of demonstrating useful applications for such devices.

3. Microfluidics Temperature Sensing

3.1 Introduction: Temperature Sensing on Small Scales

The field of microfluidics is still relatively new but it has seen massive interest in its short lifetime with potential applications in biological research and clinical point of care. These applications, such as reducing diagnostic cost and mimicking the in vivo environment of cells, have been extensively reviewed [9, 61, 62]. Our own interest in this area of research involves the use of microfluidics to fabricate devices for counting, *Section 4*, SERS analysis*,* and the culture of cells. As the field matures there is a need to develop tools for measuring the properties of such devices so we can predict how they will function. One of the key properties which requires measurement is temperature. This has implications for flow dynamics and cell health, especially for biological cells as even small variations in temperature can cause changes in cell function [63]. This is likely to be of particular importance for devices which use relatively high laser powers, 100's of mW, which result in heating, such as optical cell sorters [19] and stretchers [16]. Traditionally we would use a thermometer for such measurements but for the scales involved in microfluidics it is likely that this would perturb the system being measured reducing the significance of the result to normal operating conditions.

As this is a known problem in microfluidics several researchers have proposed the use of fluorescence thermometry as a solution. The technique uses quantum dots [64] or fluorescent dye [65] which reacts to temperature changes, shifting in either wavelength or intensity. The change in the dye emission relative to temperature is calibrated by measuring its response at known temperature settings. The calibrated emission can then be used to non-invasively measure temperature. This has proven successful but demonstrations to date have either focused on static conditions or not studied the effects flow has on temperature distribution. To fully understand the dynamics of the devices we fabricate, predict how they will affect cells inside them and optimise our experiments we need to know how flow alters temperature distribution.

To investigate if it was possible to measure the effects of flow on temperature distribution through fluorescence thermometry we made use of ULI and HF etching to fabricate a single channel fused silica device, as set out in *Section 2*. As shown in *Figure 3.1* it consisted of a single channel with two inlets and two waveguides for heating the channel. Utilising two rhodamine dyes to preform fluorescence thermometry and varying flow

conditions we found the technique to be effective for measuring temperature with a high degree of both spatial and temporal resolution.
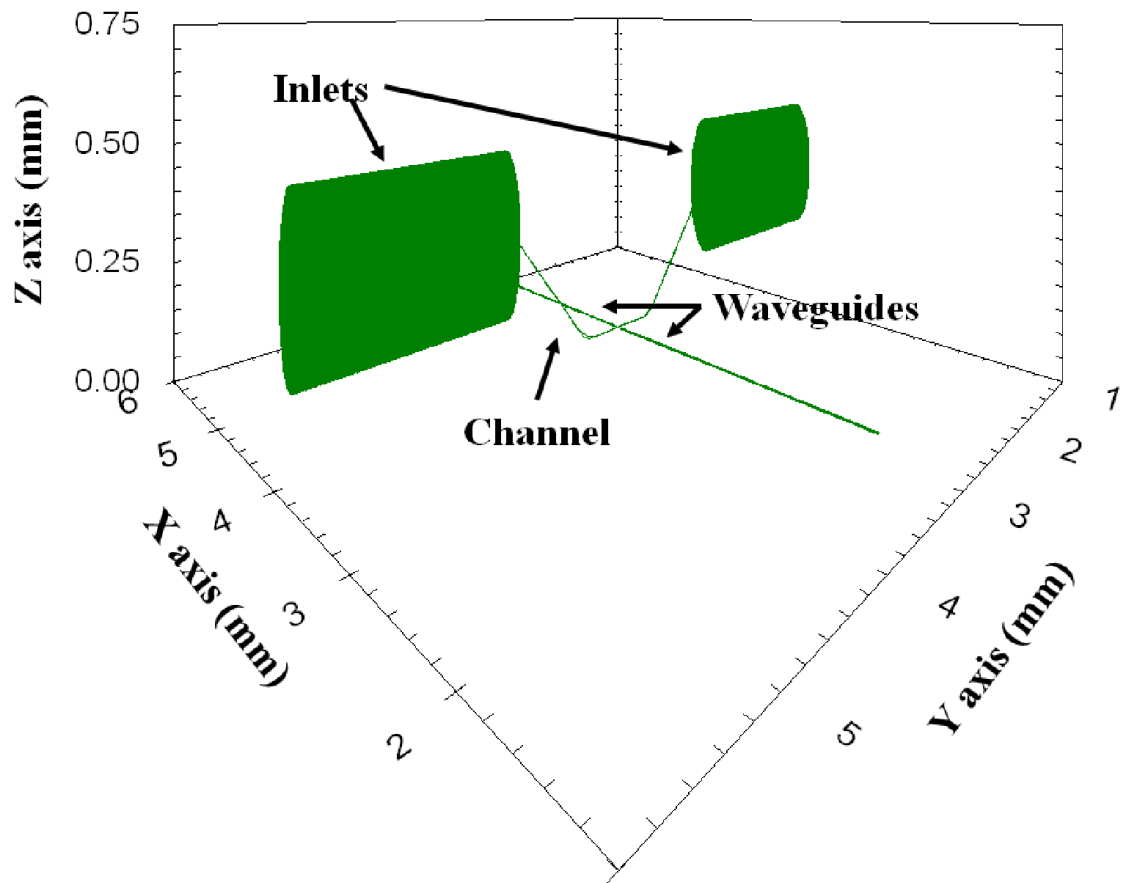
Figure 3.1: Wireframe diagram of device showing the inlets, waveguides and channels. There is a small gap between the channel and waveguides.

Having established the measurement technique was capable of generating accurate 2D maps of temperature we broadened our examination making use of additional PDMS devices, showing that we could use fluorescence thermometry in other materials. PDMS devices are fabricated through lithography which has different advantages compared to ULI. PDMS devices have highly defined channel shape while ULI has 3D capability and integrated waveguides. Making use of a PDMS device with complex channel structure we examined how its shape affected the distribution of temperature inside it. Constructing a finite element computer simulation, we compared our results to those which would be expected based on theory. We found a good degree of correlation between our experimental measurements and the model further validating the technique. Looking at the temperature in several different devices we observed that the temperature distribution and stabilisation time is highly dependent on flow rate. This had implications for future

work using biological samples as we observed temperature changes of up to 20 °C for typical operating conditions. As many cell processes such as binding rates, molecular motor activity and cytoskeleton function depend on temperature this significant change in temperature will affect measured cell properties [63].

3.2   Fluorescence Thermometry

Rhodamine is a family of dyes with a wide range of applications. In biological research it has uses such as staining mitochondria [66], measuring mercury ion levels [67] and SERS experiments [68]. It is used as a gain medium in dye lasers and in water tracing applications. In water tracing the dye's fluorescence means it can be used in concentrations as low as 10 parts per trillion increasing the distance from source it can be tracked for, compared to non-fluorescent dyes. Depending on the variant used rhodamine can be orange, pink or red in colour with a bright fluorescence emission when excited by blue light.

We chose Rhodamine dye for our investigation as others have reported it is effective for conducting fluorescence thermometry [69]. Two variants were used, rhodamine B and rhodamine 110. Rhodamine B changes emission intensity with temperature allowing us to determine temperature changes non-invasively by measuring the dyes emission. Rhodamine 110 does not change emission intensity with temperature so by monitoring its emission we will detect changes due to varying illumination levels and dye concentration.

As the emission peaks of the two dyes are close to each other, 527 nm and 580 nm for 110 and B respectively as seen in *Figure 3.2*, we can monitor both simultaneously using a spectrometer with the ratio between their peak emissions indicating temperature. This can be calibrated by heating the dyes to a known temperature.
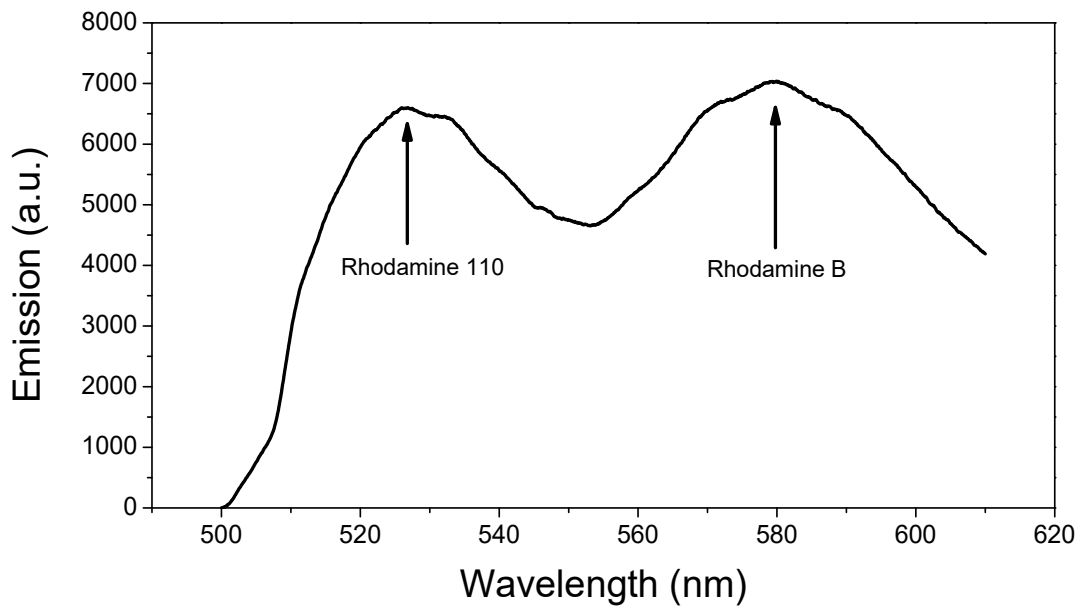
Figure 3.2: Combined rhodamine dye 110 and B emission with each peak indicated.

3.3   Device Design and Fabrication

The fused silica devices used in our investigation were fabricated using ULI and HF etching. Fused silica was chosen as it is biocompatible, has high etching selectivity allowing for the creation of complex structures and can be modified to fabricate low loss waveguides for delivering light to the channel. The design is shown in *Figure 3.1* consisting of a single channel, two inlets and two waveguides. The channel is angled to approach the surface of the device, within 170 μm, to enable imaging with high magnification objectives which typically have short working distances.

As our goal was to investigate heating inside the device we needed to heat it as much as possible to explore the maximum possible temperature range. Water absorption varies with wavelength as seen in *Figure 3.3* with several peaks which we would like to match with our excitation source. Considering the wavelengths available to us we decided to use 980 nm and 1450 nm with absorptions of 0.48 cm^{-1} and 32.7 cm^{-1} respectively. These are commonly available diode laser wavelengths.
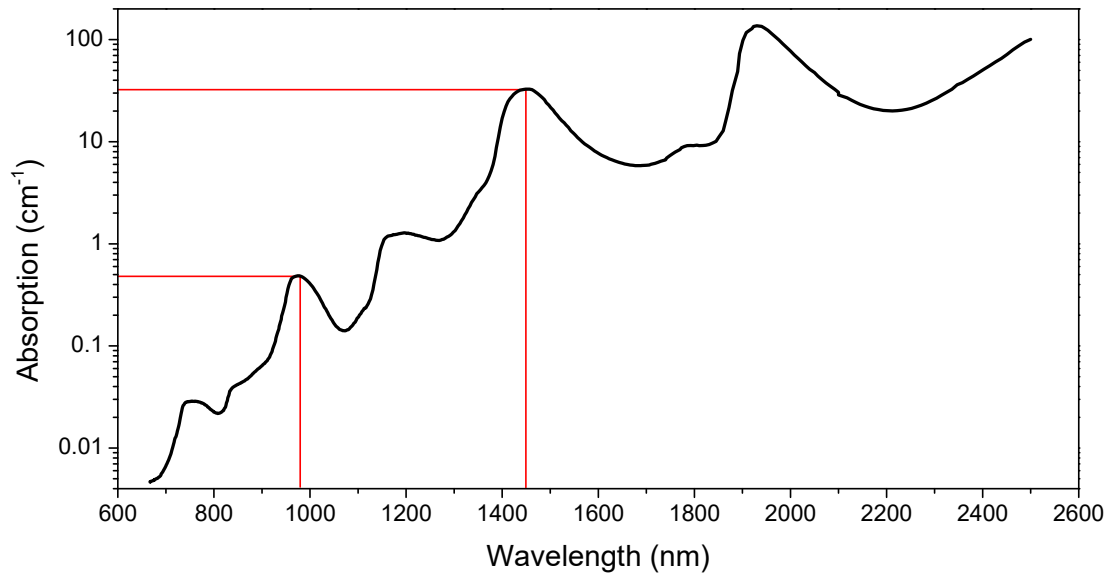
Figure 3.3: Water absorption with 980 nm and 1450 nm indicated [70].

Waveguide fabrication depends on a number of inscription parameters as described in *Section 2.4*. Our goal when optimising these was to minimise waveguide loss to couple as much power as possible into the channel and single mode operation so that the channel was heated in a predictable manner. This presents a problem using a single waveguide as one which is single mode at 1450 nm will be multimode at 980 nm. The reverse is not true however and by using a single mode waveguide optimised for 980 nm we achieved single mode operation at each wavelength at the cost of additional loss at 1450 nm. The additional water absorption is more significant than the additional loss at 1450 nm leading to a net gain in power absorbed by the water.

Optimising for single mode operation at 980 nm and low loss required a series of waveguides to be written using different laser parameters to find those which met these requirements. To narrow down the range of parameters we made use of the V number *Equation 2.2* to predict the diameter at which they would operate on a single mode. Using a wavelength of 980 nm, the refractive index for fused silica being 1.45 and knowing the refractive index modification will be around 0.5 %, from our previous work on waveguide writing within the research group, we expect a diameter of less than 5.2 μm to be single mode.

Even with this starting point there is still a large number of parameters available, laser power, repetition rate, number of scans, scan separation, objective NA and translation speed. This gives an indication as to why establishing ULI in new materials can be a time

consuming process. As fused silica is a well-studied material we drew on this knowledge base to select a repetition rate of 500 kHz, NA of 0.4, and scan separation of 0.35 μm leaving power, inscription speed and number of scans to be varied.

Writing waveguides while varying these parameters produced a set of waveguides which were then inspected to measure loss and determine how many modes they supported. The modes of a waveguide can be observed by coupling a laser source into them and imaging the output. Translating the input relative to the waveguides excites different modes in the waveguide allowing these to be recorded.

For loss measurements we measure insertion loss. It is defined as the difference in signal when a fibre connecting a laser to a detector is broken in two and a waveguide placed between the ends. We made use of a 980 nm diode laser coupled to a single mode fibre. This was positioned to couple light into the waveguides and the output collected using another single mode fibre connected to a KD optics power meter, DATS01HP. The equipment used for this is shown in *Figure 3.4*.
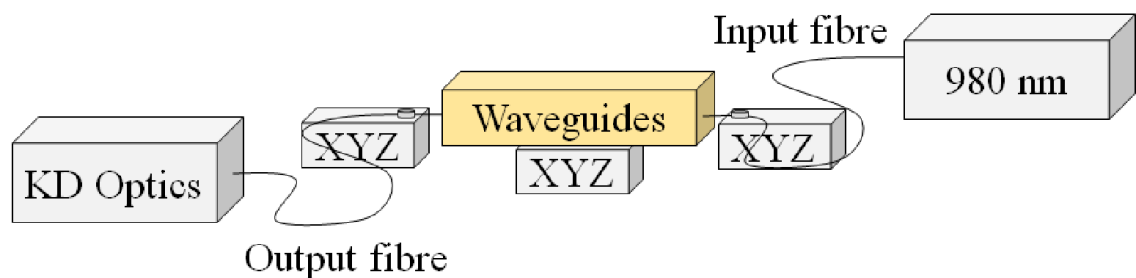
Figure 3.4: Waveguide loss measurement setup with fibre coupled laser source, 980 nm, and detector, KD Optics. The fibres and waveguides were mounted on translation stages and aligned relative to each other to maximise the coupling of light between them.

The insertion loss is the combination of several components as described in *Table 3.1* and *Figure 3.5*. Insertion loss is simple to measure compared to the individual components so was used to optimise our waveguides. If the individual components of loss are required there are several methods of determining them.

Those we have used are the cutback method where the insertion loss of the sample is measured then a portion of the sample removed. The insertion loss is re-measured with the difference between this reading and the previous one being the propagation loss of the removed length of sample. Knowing the propagation loss, we can then simply determine the other components.

The other method we used relies on the assumption that input and output coupling loss are the same. This is valid for single mode waveguides and fibres where the mode field diameter is the same. For this method the insertion loss is measured using single mode fibre input and output then measured again using a large core fibre for the output which collects all the light. The difference in loss is the coupling loss and once this is known the other components can be calculated.

Coupling Loss -	Coupling loss, as seen in *Figure 3.19*, is the loss due to mismatch between the mode field diameter of the optical fibre and waveguide.
Propagation Loss -	This is the loss due to scattering or absorption of light as it passes along the waveguide.
Fresnel Loss -	At every interface there will be a Fresnel loss. For n_{air}=1 and $n_{fused\ silica}$=1.45 this is 3.4%. This is significant as there are 4 interfaces in the system. By adding index matching fluid, n_{decane}=1.41, this reflection is reduced to 0.02%. Decane is a derivative of petrol with uses in paint, varnishes and in optics for index matching.
Divergence -	As the light leaves the fibre it diverges. This will depend on the NA of the fibre. For our waveguides in air this is 8.35°. Placing the sample in decane reduces this to 5.91°. By placing the fibre close to the waveguides this loss is minimised. Within 1 μm the laser spot increases in diameter by only 4%.

Table 3.1
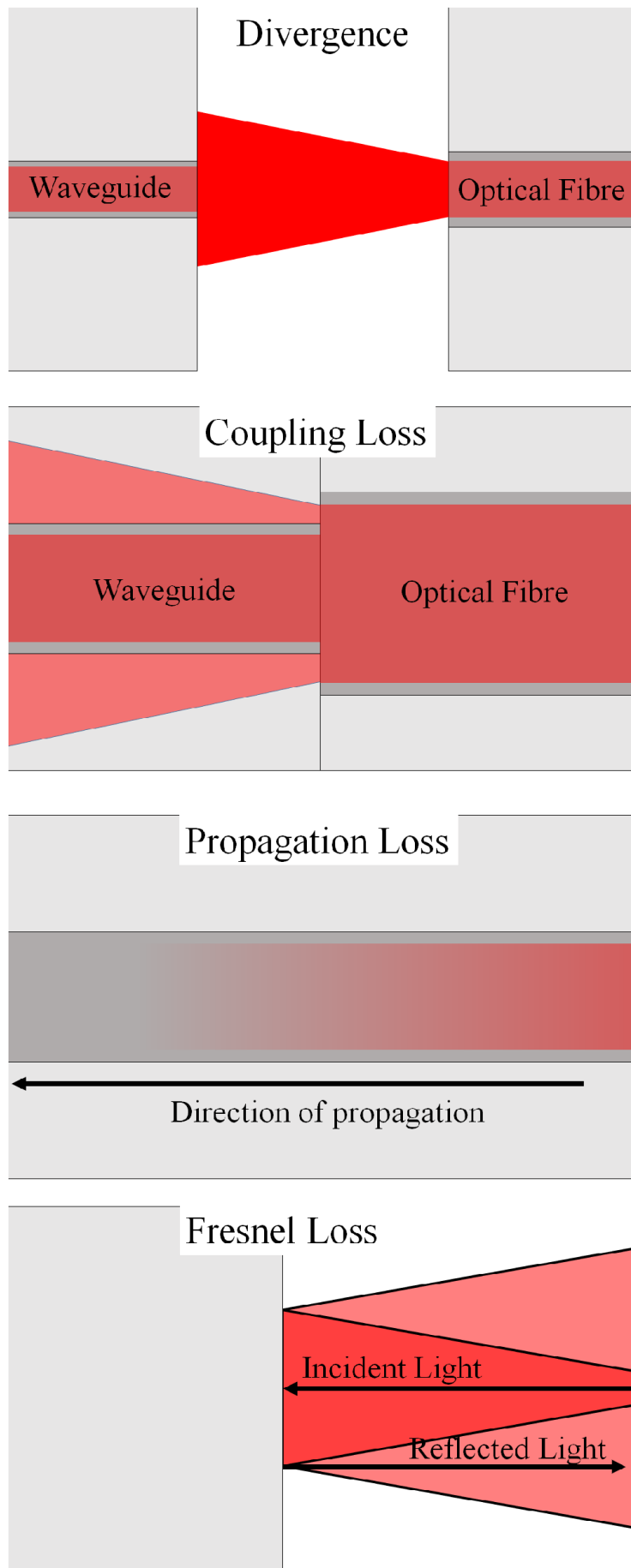
Figure 3.5: Sources of loss in optical waveguides.

The insertion loss for waveguides inscribed with varying power and scans is shown in *Figure 3.6*. There is a clear relationship between loss and inscription power which can be explained by both the refractive index change and inscription height increasing with power until the v number equation condition is met, *Equation 2.2*. At even higher powers than those measured we would expect the loss to increase again as we transitioned from the refractive index modification inscription to damage regimes. *Figure 3.7* shows how the insertion loss varies with number of scans, i.e. waveguide width. While the effect is not as pronounced as in *Figure 3.6* there is still a correlation between scans and loss with the lowest loss being for 9 scans. The high loss for narrow waveguides can be explained by the v number equation. For wider waveguides there is increasing coupling loss as we attempt to couple an increasingly large multi-mode waveguide to a single mode fibre.
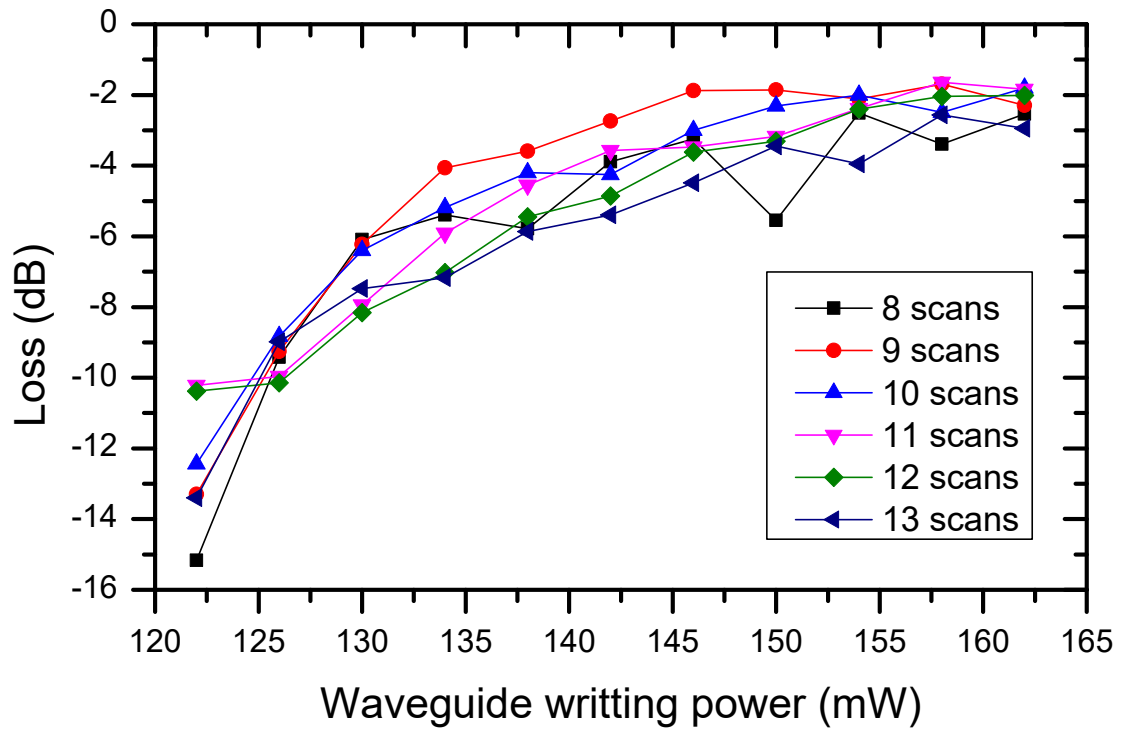
Figure 3.6: Waveguide insertion loss increasers with writing power.
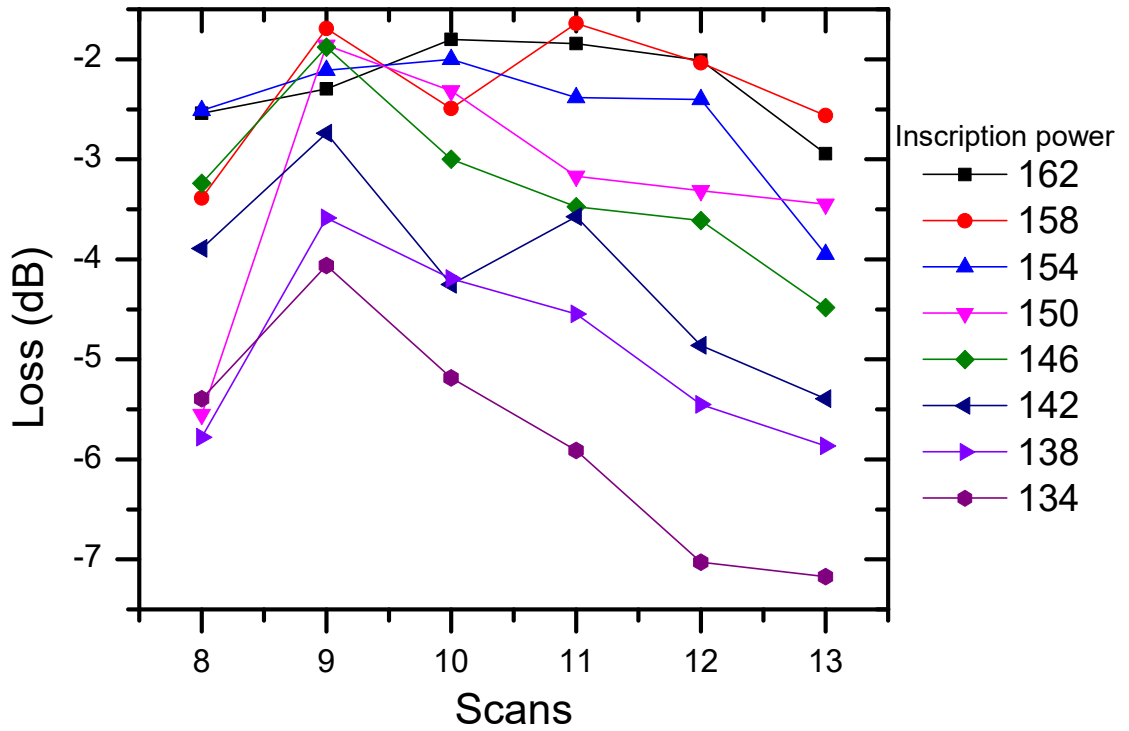
Figure 3.7: Waveguide insertion loss varies with number of scans peaking around 9 scans.

Measuring the loss of each waveguide we found the parameters which gave the lowest loss for single mode operation. The loss of this waveguide was then measured at 1450 nm, taking account of additional sources of loss at this wavelength due to the use of input fibre designed for 980 nm. The optimal parameters as well as losses are:

Inscription power -	152 mW
Translation speed -	1 mm.s^{-1}
Objective NA -	0.4
Repetition rate -	500 kHz
Pulse length -	360 fs
Scans -	10 with a spacing of 0.35 giving a diameter of 3.15 μm. The inscription laser has a spot size of 3.2 μm making the modified region larger than that set by the writing code.
Loss, 980 nm -	2 dB estimated over for the final device
Loss, 1450 nm -	5.5 dB estimated over for the final device

Table 3.2

To determine optimal etching parameters, we conducted a scan of possible values using an IMRA μ-Jewel femtosecond laser. From previous work we know that using a repetition rate of 500 kHz, pulse length of 360 fs and 0.4 NA objectives will give the highest etching selectivity [7, 11, 20]. This leaves power and translation speed to be inspected. Single lines were inscribed in a fused silica substrate with varying parameters then etched in HF to compare etching selectivity. From this we determined that the optimal inscription parameters were as follows:

Inscription power -	300 mW
Translation speed -	2 mm.s^{-1}
Objective NA -	0.4
Repetition rate -	500 kHz
Pulse length -	360 fs

Table 3.3

Using our optimised parameters for waveguides and etching we inscribed the design as shown in *Figure 3.1*. The design fits multiple times into a single fused silica substrate allowing us to take advantage of the fast prototyping abilities of ULI to fabricate multiple variations on the same design at once. These variations were in the size of the central channel and depth from the surface. The inscribed devices are shown in *Figures 3.8* and *3.9* where we can see the inlet channels and waveguides. While the parameters for inscription of regions to be etched are different to the waveguides it is still necessary to inset the waveguides to avoid them being exposed to the HF as they etch more quickly than unmodified fused silica.
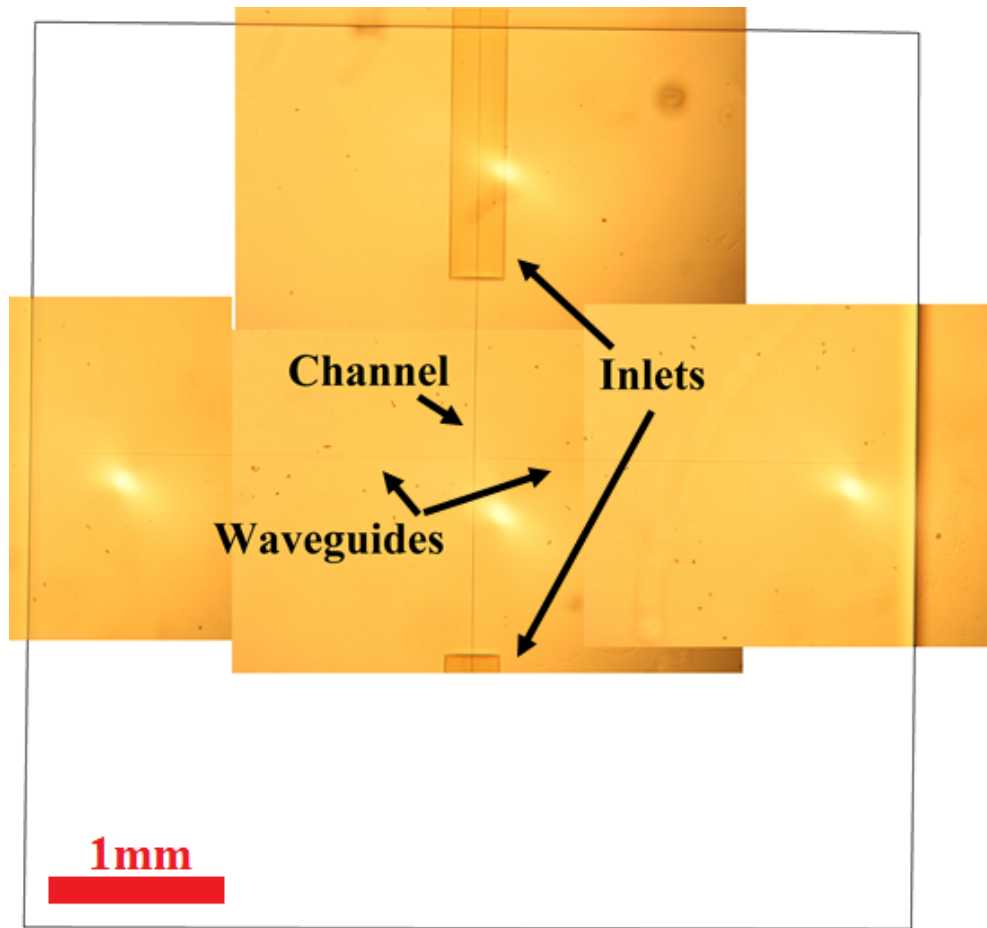
Figure 3.8: Composite image showing the device inscribed in fused silica before etching. The border represents the device edges to give an indication of device size.
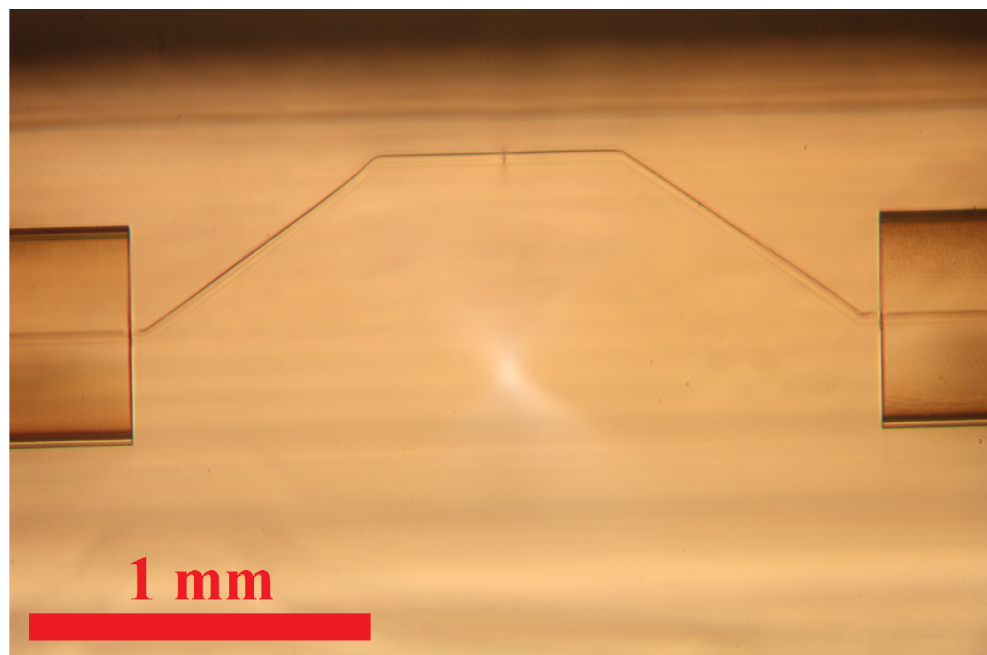
Figure 3.9: Side view of the device before etching showing how the channel approaches the surface. The waveguide can be seen as a small spot in the centre of the channel.

After inscription the devices are etched in acid clearing the channel and inlets of fused silica. While etching selectivity of up to 280:1 is achievable [35], unmodified material will etch as well as that which has been modified so the process must be carefully monitored to prevent over etching, resulting in larger channel sizes or in extreme cases device loss when the channel breaches the device surface. Etching was conducted in 10% HF for around 12 hours, with each device being removed individually when it had completely etched. The devices produced are shown in *Figures 3.1* and *3.11* where the channel and waveguide are indicated. The channel sizes after etching were:

Parameter	Minimum (µm)	Maximum (µm)
Channel height	27	57
Channel width	13	35
Depth from surface	61	102

Table 3.4
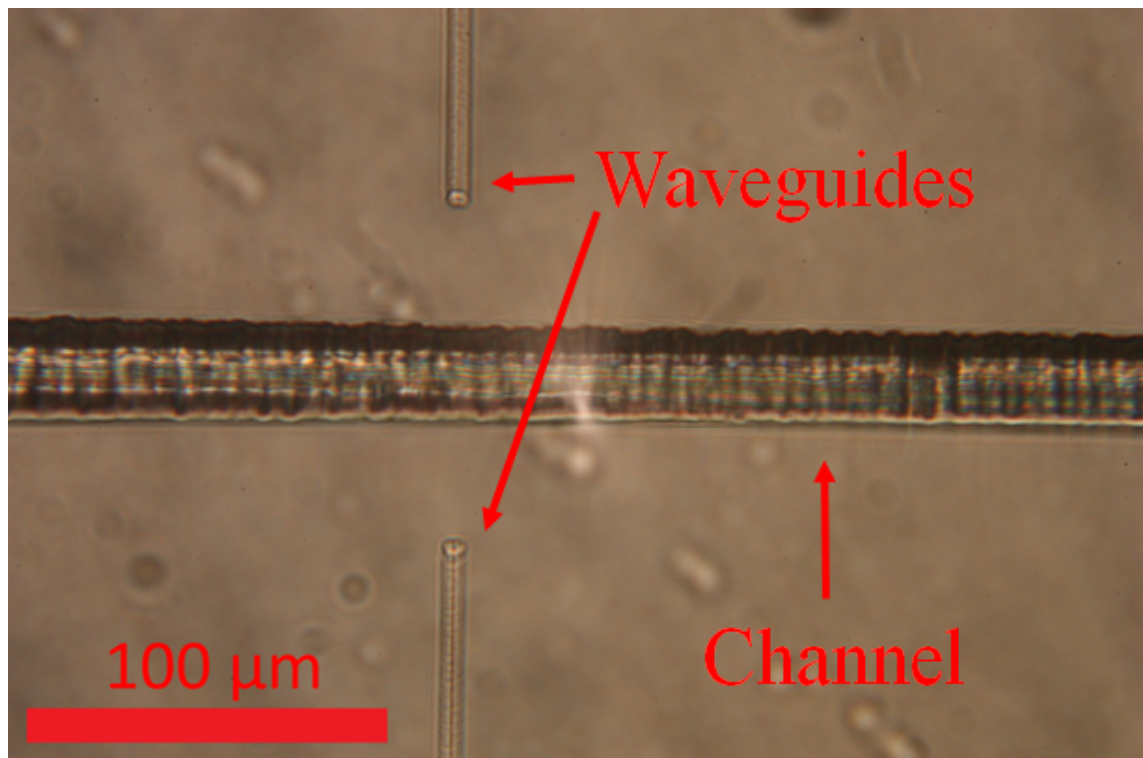
Figure 3.10: Top view of the microfluidic device after etching showing the microfluidic channel and unetched waveguides for delivering light.

39
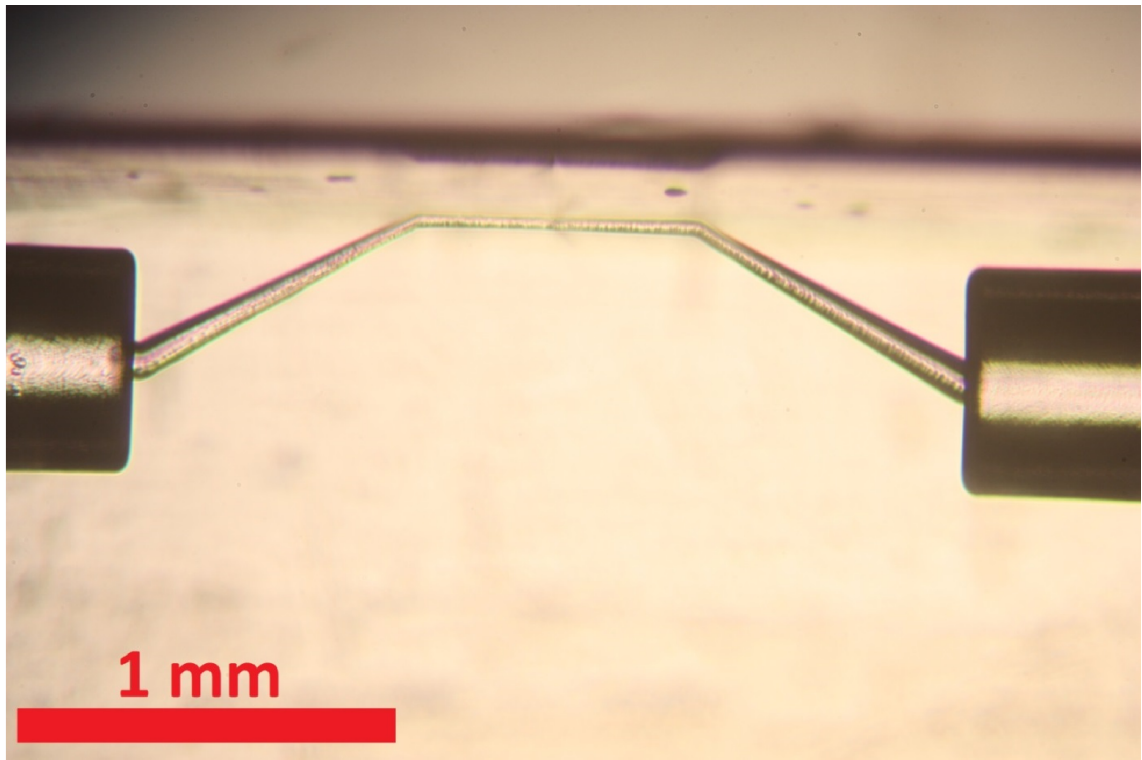
Figure 3.11: Side view of the device after etching showing the channel approaches the surface of the glass chip.

To allow our device to be connected to a syringe pump we attached microfluidic tubing, with an outer diameter of 360 μm and inner diameter 100 μm. The tubing was made of Polyether Ether Ketone (PEEK) which is chemically resistant, biocompatible and resistant to high temperatures. It was bonded to the inlets using Thorlabs N0A61 UV curing optical adhesive. The glue is liquid allowing it to be pulled into the inlet through capillary action then set using a UV lamp.

When measuring waveguide loss, it was necessary to continually align into different waveguides. This is not required or desirable when using the final device so by bonding the input in place the device becomes alignment free during experiments. This is achieved using a v-groove purchased from SQS Vláknová optika consisting of a single mode 980 nm fibre bonded to a piece of fused silica. The v-groove array was positioned as shown in *Figure 3.12*. It was aligned by passing a 980 nm laser through the v-groove into a waveguide then measuring the power out of the opposite waveguide. There is a large loss between the waveguides when the channel is empty due to scattering from the surface and divergence in the channel. This is reduced by passing water through the channel to closely match the refractive index of fused silica. While we use 980 nm as one of our heating wavelengths the total absorption is only around 0.2% when passing through 35

µm of water which is insignificant compared to sources of loss in the channels when they contain air. Once optimal alignment was achieved, maximising transmission, the v-groove was bonded in place using Thorlabs N0A61 UV curing optical adhesive which is optically transparent at 980 nm and 1450 nm.
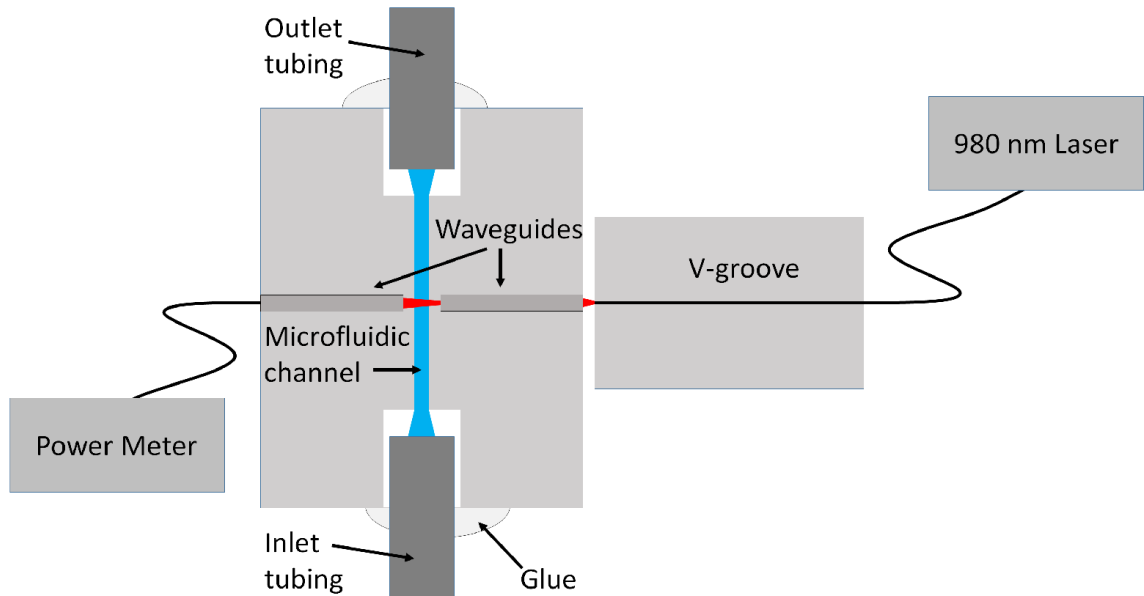
Figure 3.12: Alignment of v-groove fibre input to the microfluidic device.

3.4 Experimental Results

After completing fabrication of the microfluidic devices they were transported to the Universidad Autónoma de Madrid where, in collaboration with researchers there, we took advantage of their microscope systems to preform fluorescence thermometry experiments. The aim of the experiments was to demonstrate that we can use fluorescence thermometry to observe the effect of flow on temperature distribution in microfluidic devices.

Two microscope systems were used for these experiments. The first, a reflection/transmission microscope with a video camera to record fluorescence in the devices had fast acquisition time but could not provide accurately calibrated temperature readings as it did not record the wavelength of the emitted fluorescence. The second system was a confocal microscope connected to a Horiba Jobin Yvon iHR320 spectrometer allowing for both high spatial accuracy and the calibration of readings using

rhodamine 110 as a background level. These microscopes will be referred to as the video and confocal microscopes from this point onwards.

Using these systems, we first investigated our ability to measure temperature inside devices before looking at the effects of fluid flow on stabilisation time and temperature distribution inside devices. If the total change in temperature in the microfluidic channel is ΔT the stabilisation time is defined as the time taken to rise to 63% of this, the 1/e criteria.

Making use of the video microscope system we placed devices in it then pumped Rhodamine B through them using a syringe pump, NE-1002X Programmable Microfluidics Syringe Pump with rates between 8 pL.hr^{-1} to 2.5 mL.min^{-1}. The sample was illuminated using a UV lamp integrated into the microscope to excite the rhodamine B dye and suitable emission filters used before the camera so only the dye fluorescence was recorded. Readings were taken as videos then split into single frames as shown in *Figure 3.13*. (a) shows the fluorescence from the dye in the channel with no laser applied, (b) shows the dye when the laser is switched on with the dip indicating heating, (c) is the subtraction of (b) from (a) giving the change in fluorescence. As we only make use of one dye the readings are not calibrated but are sufficient to investigate the stabilisation time using arbitrary units of intensity.
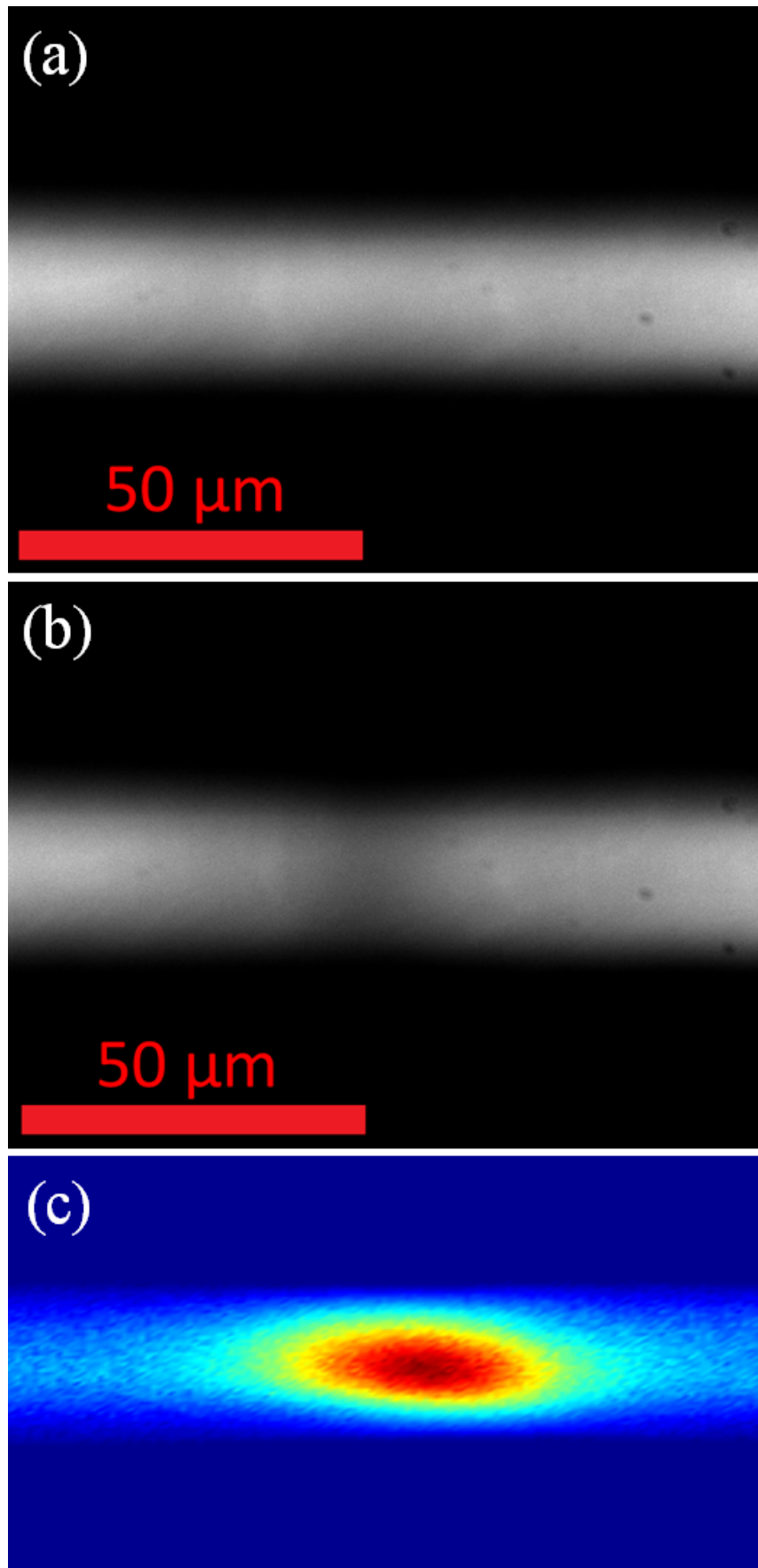
Figure 3.13: Fluorescence dip when the channel is illuminated by the laser. (c) heat map image is a background subtraction of (a) from (b) showing the relative change in intensity across the channel. The laser used was 1450 nm at 400 mA.

The video microscope system was capable of generating 2D maps of temperature quickly being limited only by the camera frame rate, 10 Hz in our case. In contrast the confocal microscope required the sample to be translated relative to the microscope objective to build up a 2D map of the channel with a fluorescence reading being taken at each point. This process takes several seconds per point with the total time being determined by the number of data points required.

The confocal microscope system is depicted in *Figure 3.14* and consisted of the confocal microscope, computerised xyz positioning stages and a 488 nm diode laser pump source to excite fluorescence in the rhodamine dye. The microfluidic devices were placed in this system and a mixture of Rhodamine B and 110 pumped through them. Monitoring the fluorescence emission of both simultaneously we can detect changes in temperature as the rhodamine B will decrease in emission intensity when heated while the rhodamine 110 will not so acts as a background signal to account for local changes in dye concentration or laser illumination. Calibration was conducted by adding a hot plate to the system and measuring the relative dye emissions at set temperatures. Comparing this to our data when heating with the laser gave temperature readings throughout the channel.
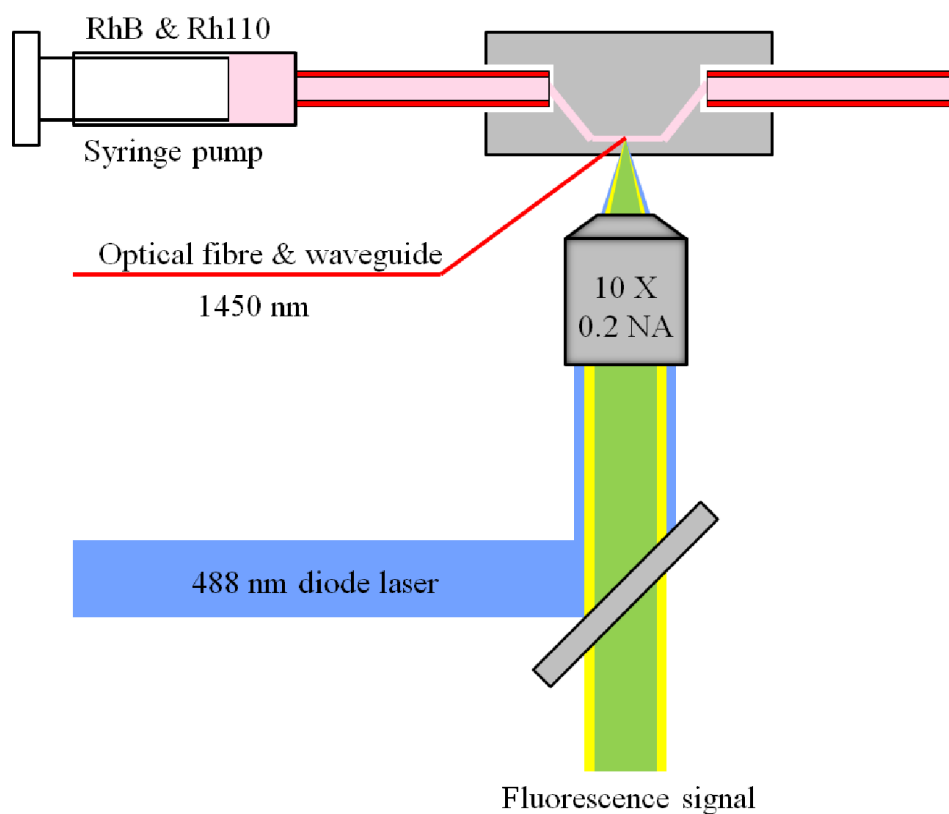
Figure 3.14: Diagram of the experimental setup for exciting the dye fluorescence.

We took a series of measurement of fluorescence while varying laser power then calculated the dye ratio for each reading. An example of our raw data can be seen in *Figure 3.15* where we see the dye emission changing with laser power. To calibrate our dye emission, finding the ratio for known temperatures, we used a hot plate to obtain the calibration curve shown in *Figure 3.16*. When using fluorescent dyes photobleaching is always a potential issue and in this case if could influence our results. If one of our dyes, rhodamine 110 or B, photobleaches more quickly than the other then this could result in a changing ratio between them. We do not believe this to be an issue due to the short exposure times with dye spending only a few ms in the focal region even for the lowest flow rates. Using our calibration curve to convert the emission ratio to temperature, as shown in *Figure 3.17*, gives a maximum heating of 19 °C for 230 mW of 1450 nm laser light. We see a linear relationship between laser power and temperature. This is the relationship we would expect until the temperature saturates at higher powers. 19 °C is a significant amount of heating enough to be of concern in any experiments using mammalian cell lines which must be maintained at 37°C [63]. Having demonstrated that we can use two dye fluorescence thermometry to measure temperature within devices we next decided to investigate the effects of flow rate on heating in a microfluidic channel.
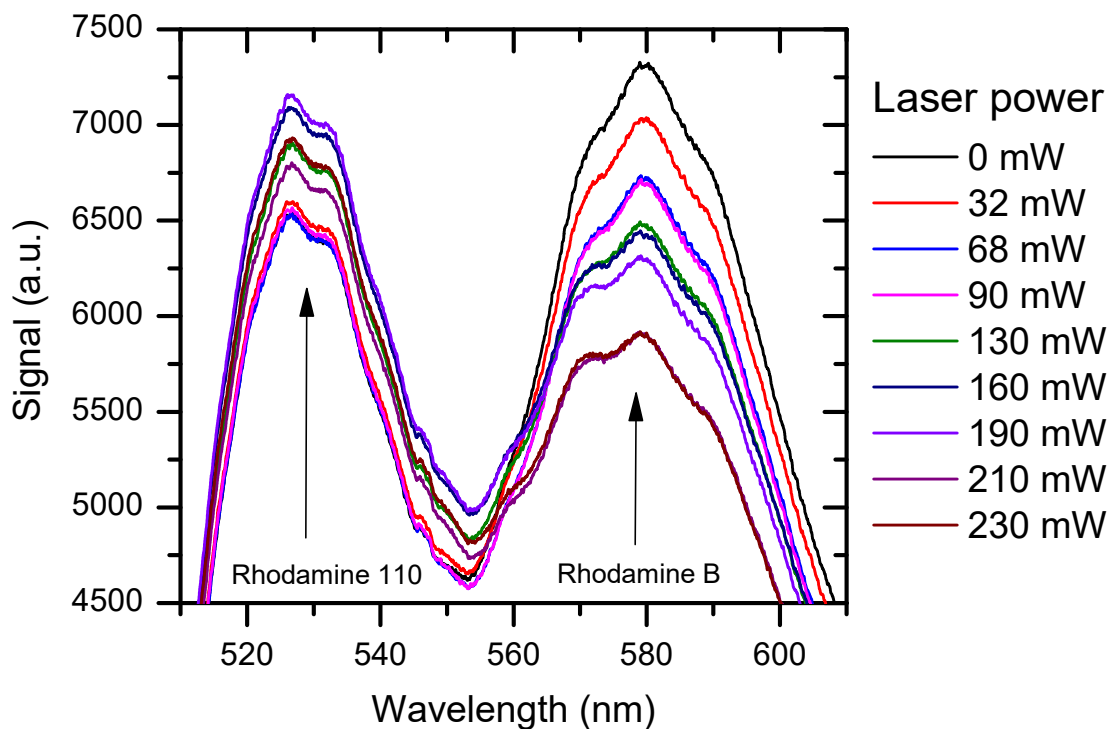
Figure 3.15: Rhodamine 110 and B emission for different input laser powers. The ratio between the two emissions can be seen to vary with power. Flow rate 0.5 µL.min^{-1}.
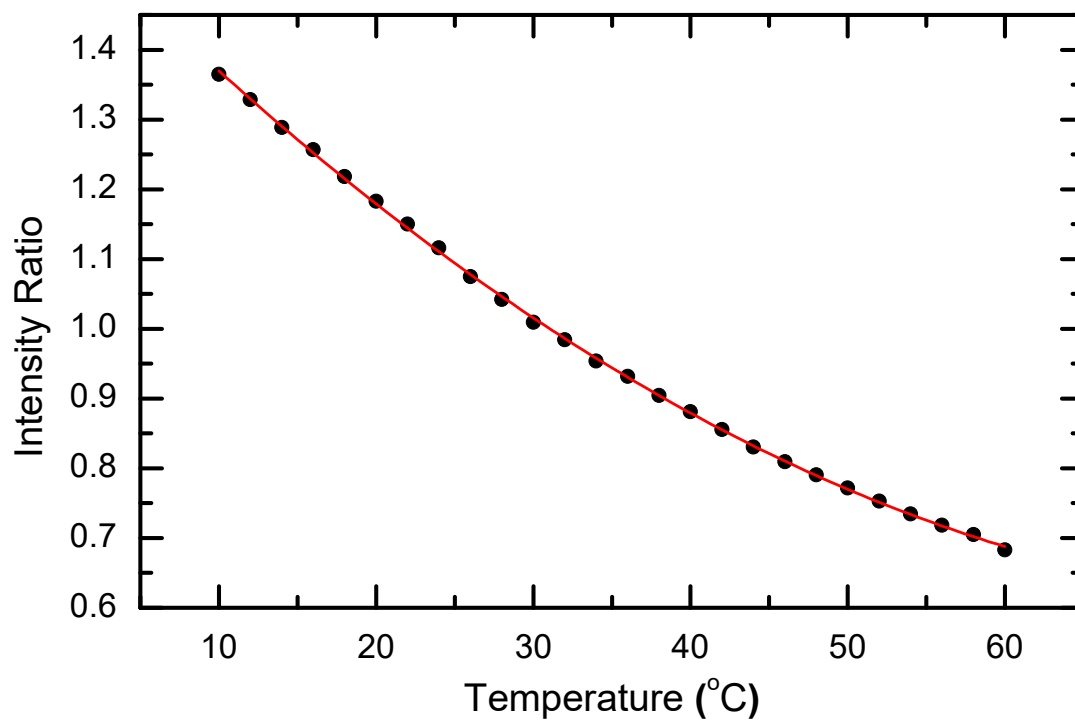
Figure 3.16: Temperature calibration cure used to convert dye intensity ratio to temperature.
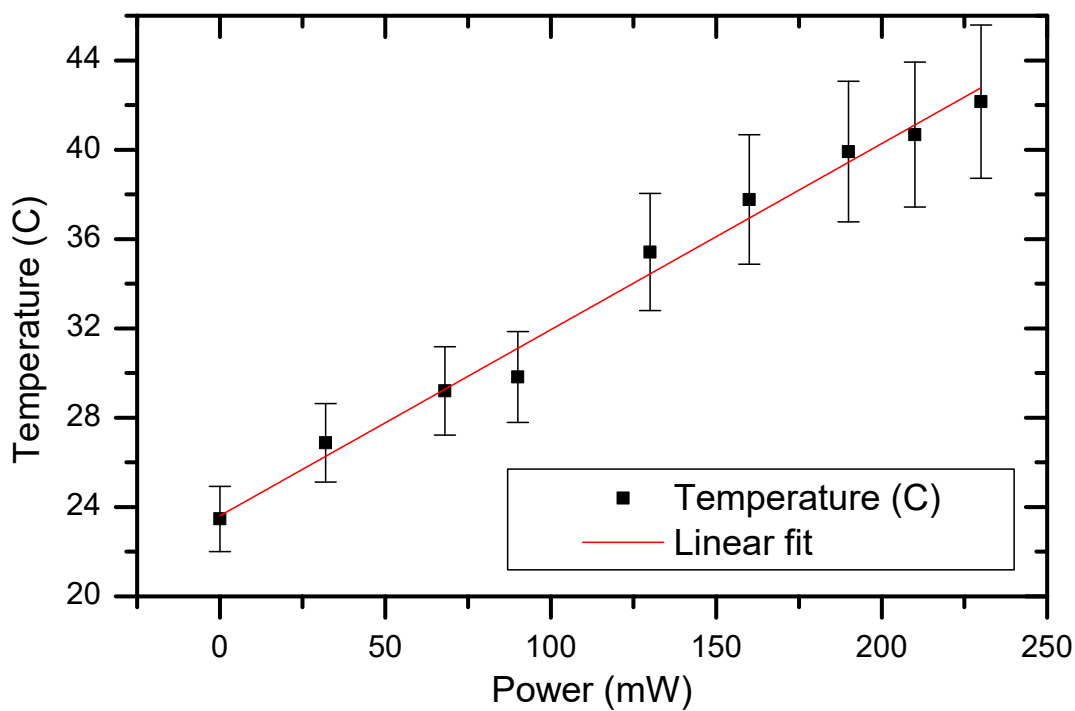
Figure 3.17: Temperature change as laser power is increased determined by the ratio between rhodamine 110 and B emission for a 1450 nm pump wavelength. Flow rate 0.5 µL.min^{-1}.

Stabilisation time is one of the most important properties we would like to know for a microfluidic device. Taking readings before temperature has stabilised inside a device is likely to lead to inconsistent results. This will be especially important in devices where there is constant heating and cooling such as optical cell sorters, where a laser is used to divert the path of cells. In such devices a laser is repeatedly switched on and off causing constant changes in temperature and fluidic currents inside the channel which may affect sorting efficiency. To investigate this, we used two PDMS single channel devices, bought commercially to both save time in fabrication and demonstrate measurement in an additional material. The time taken for the channel to thermally stabilise is predicted by:

$$t_T = \frac{L^2}{K}$$

<div align="right">Equation 3.1</div>

where t_T is the time required for temperature to rise to 63% of the final steady state temperature, L is the characteristic size of the system, the channel width or height, and K the thermal diffusely of the medium, 1.43×10^{-7} m^2.s^{-1} for water. This equation assumes no convection currents or changes in contour conditions [71].

Using two devices with channel width of 100 μm and 200 μm we apply 980 nm light to the channel through 50x objective, as the devices do not have embedded waveguides, and record the temperature at the focal point of the objective. *Equation 3.1* predicts that for these devices we should expect stabilisation times of 70 ms and 280 ms for 100 μm and 200 μm channels respectively, a ratio of 4:1. Our experimental results in *Figure 3.18* show the expected trend of smaller channels stabilising more quickly with 180 ms and 790 ms for the 100 μm and 200 μm channels respectively. The data do not match the predicted values though the ratio of 4.4:1 is in good agreement. Looking at the fitting of the data we see that the best fit is given by a double exponential as shown in the insert. There is both a fast and a slow component implying two processes are present.
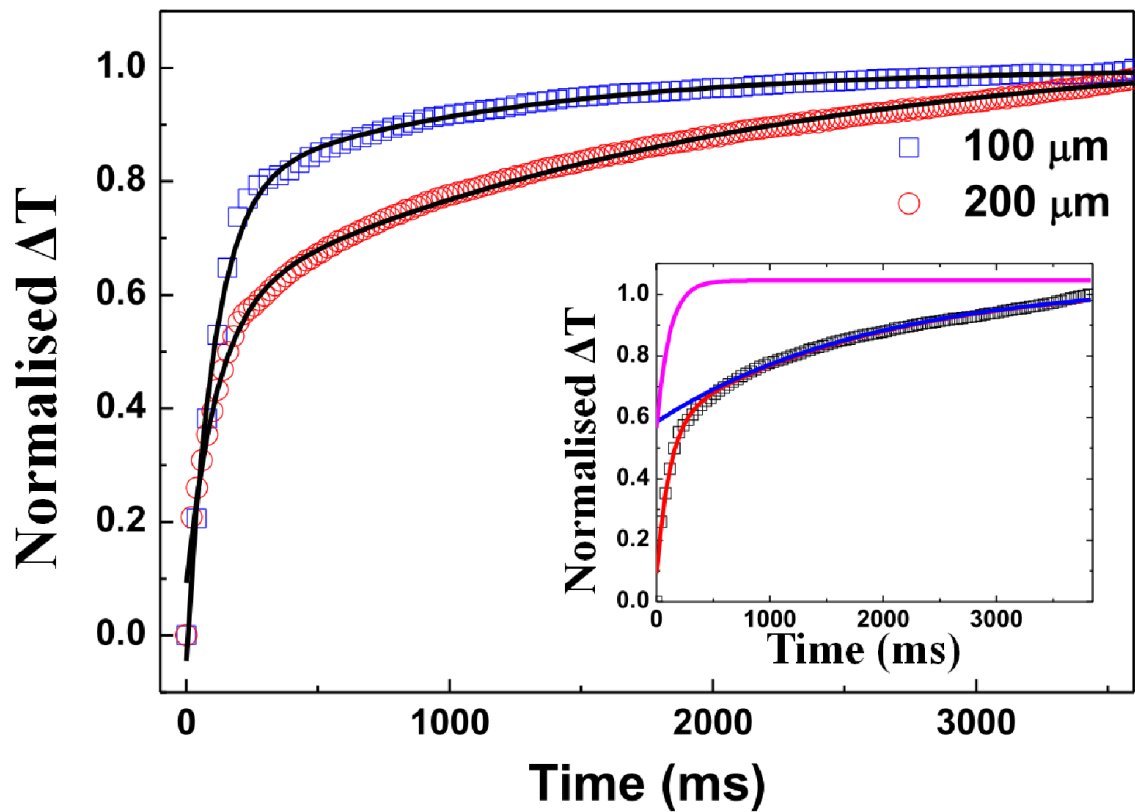
Figure 3.18: Temperature inside microfluidic devices when heated with a laser beam. Data points are experimental readings while solid lines are double exponential fits. Inset, the two exponential components, pink and blue, of the 200 μm channel fit, red.

Investigating this further we looked at the effect of flow rate on the stabilisation time. Varying the flow rate in the 100 μm channel we see in *Figure 3.18* that the stabilisation time decreases as flow rate is increased and that the weighting of the two exponentials fitting the data changes. The relative weighting of two exponentials used to fit the data changes with flow rate as seen in the inset. At fast flowrates a fit using only the fast exponential can be used giving a stabilisation time of 80 ms closely matching our prediction from *Equation 3.1* of 70 ms. From these results we conclude that the two exponentials in our fits represent the thermalisation time of the fluid for the fast component and the slow component is due to convection currents in the channel and changes in temperature contour conditions. Fast flow rates then minimise the components from convection currents and contour changes leaving only the fast component. These results are of relevance for our future choice of channel size and flow rate as they have a significant impact on stabilisation time.
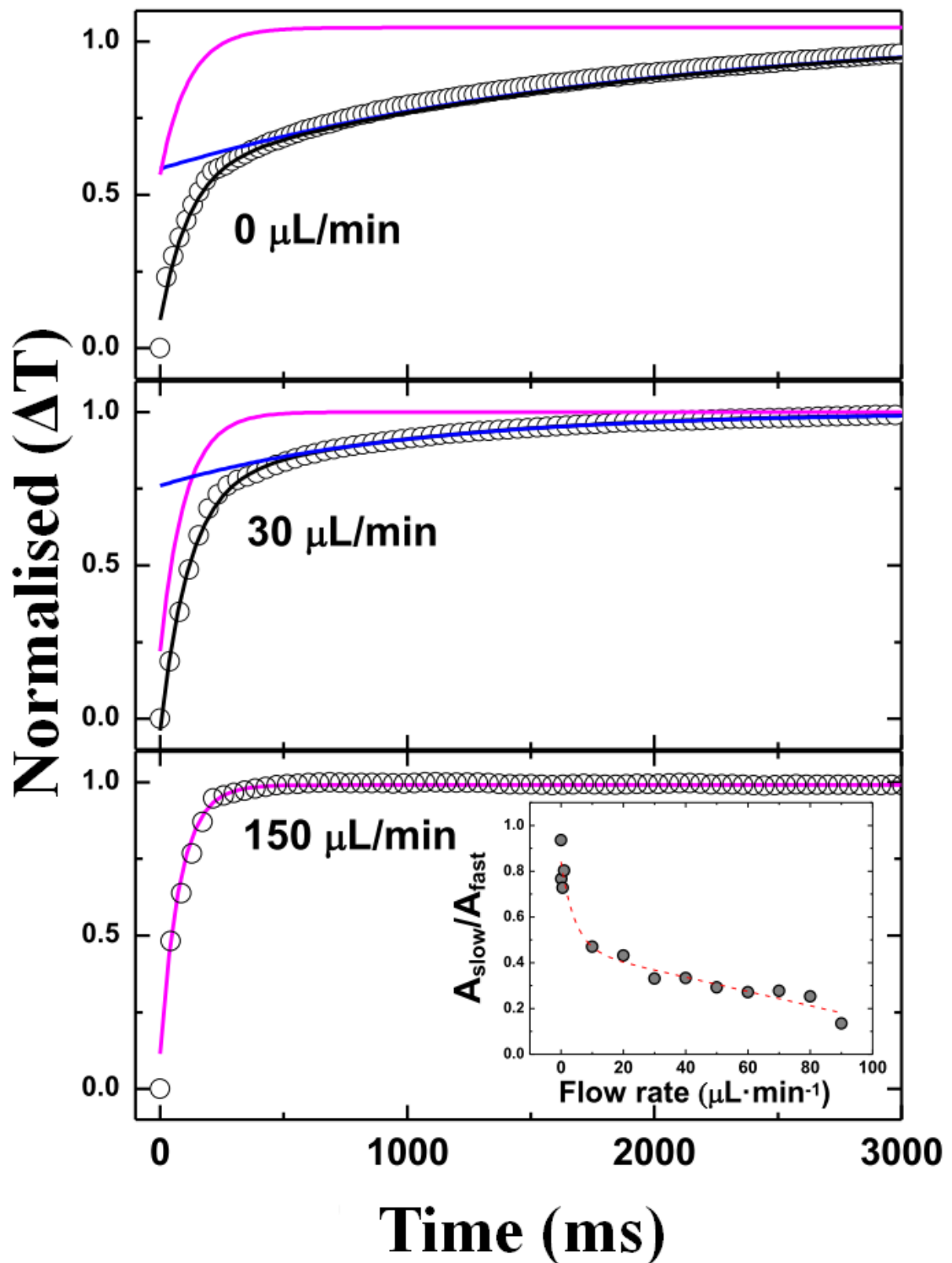
Figure 3.19: Stabilisation time for varying flow rate. At high flow rates data can be fit by a single exponential. Inset shows the contribution from the fast and slow exponentials.

We next look at devices with more complex channel structures to see how our temperature measurement technique works for such devices and investigate how they behave under normal operating conditions. The device chosen is designed for the sorting of particles using an optical fibre to divert samples between two channels with the scattering force of

photons on the particles. Using 450 mW of 980 nm light we achieve a maximum sorting efficiency of 75% for microspheres as seen in *Figure 3.20*. Using these conditions, we examined temperature distribution over time using the confocal microscope system. The results, seen in *Figure 3.21*, show a maximum temperature change of 5 °C, enough to be of concern depending on the type of particle being sorted. We also see a significant change in temperature distribution depending on flow rate with it being localised to the area of laser illumination at 0.01 μm.min^{-1} but becoming asymmetric at 1 μm.min^{-1}. This change in temperature distribution with flow rate is an interesting result we investigated further through the use of computer simulation.
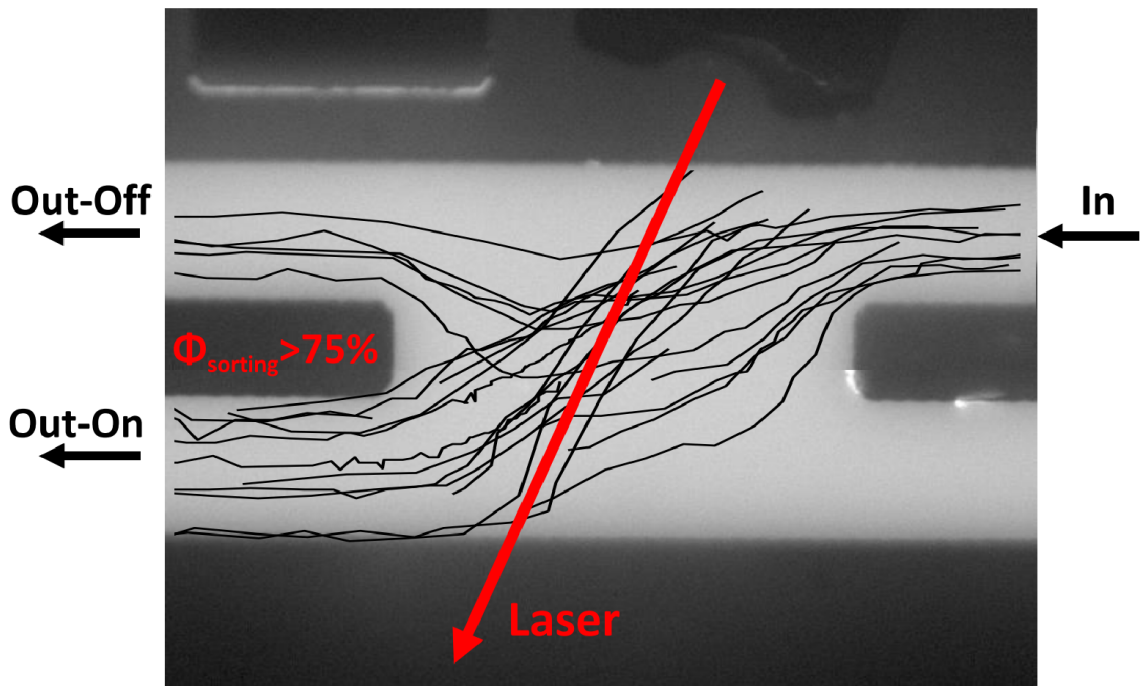
Figure 3.20: Optical cell sorter showing the trajectories of particles as they pass through the device. The fibre providing the optical force can be seen in the top of the image.
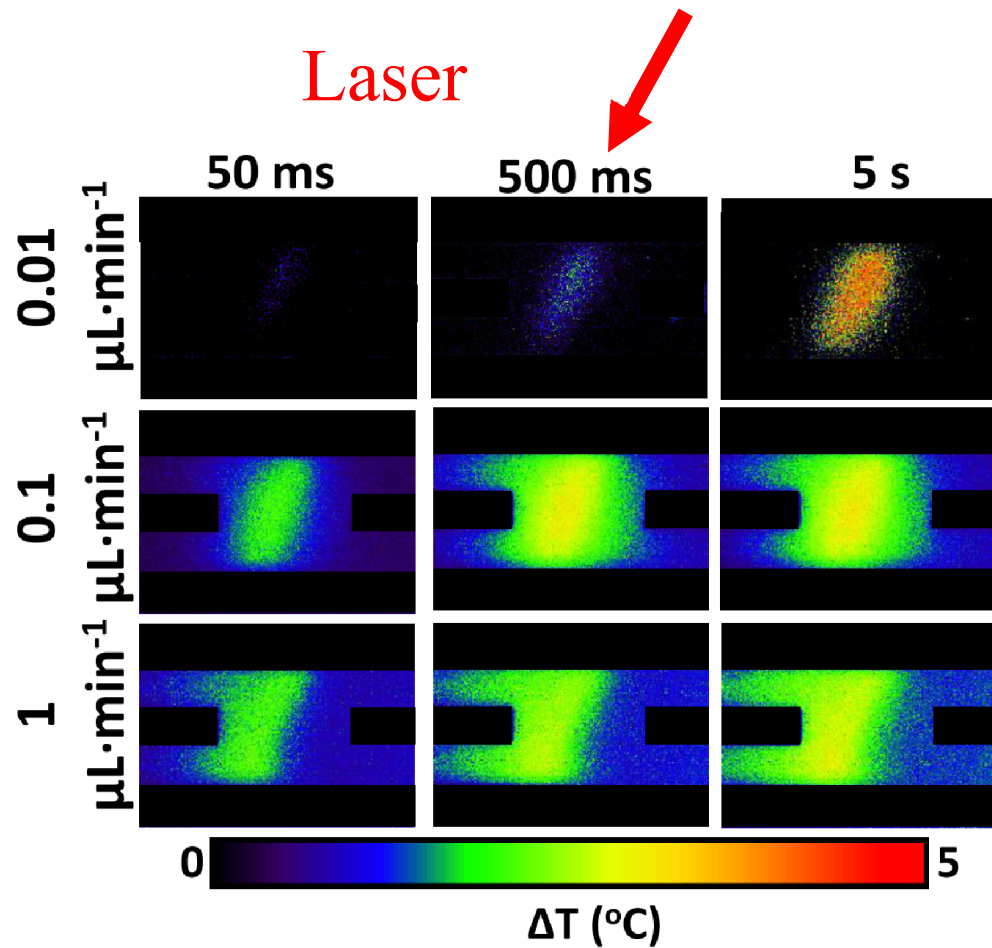
Figure 3.21: Time evolution of temperature distribution in an optical cell sorter for several flow rates.

The effect of flow rate on temperature distribution was modelled using COMSOL Multiphysics 4.3 conjoined heat transfer module. The Navier–Stokes equation, the continuity equation and the heat transfer equation were coupled in COMSOL to solve the problem. Assumptions were that material properties were constant over the temperature range investigated, there was no slip at the walls and the fluid was incompressible. The purpose of this modelling was to predict what changes in temperature distribution would be expected through theory and to see how closely our experimental data matched this prediction. The experimental data for this comparison was taken using a 300 mW 980 nm laser with flow rates between 0 and 300 $\mu L.min^{-1}$. The temperature measurements, seen in *Figure 3.22 (a)*, show a decrease in heating with flow rate as more water passes the laser spot in a given time distributing its power over a larger volume. A notable effect which may not be expected is that the position of maximum intensity also changes with flow rate moving further down the channel as the rate is increased. This is of interest in experiments involving trapping of particles as it will impact particle heating.

Comparing experimental results to the model we see in *Figure 3.22 (b)* that the predicted and measured temperature changes are the same within the errors of our measurement. We also see that our measurement of maximum intensity position matched that predicted by the model within error, *Figure 3.22 (c)*. It moves downstream by up to 30 μm for a flow rate of 300 μL.min^{-1} which is larger than many of the samples we will look at in future experiments though smaller than some biological cell types.
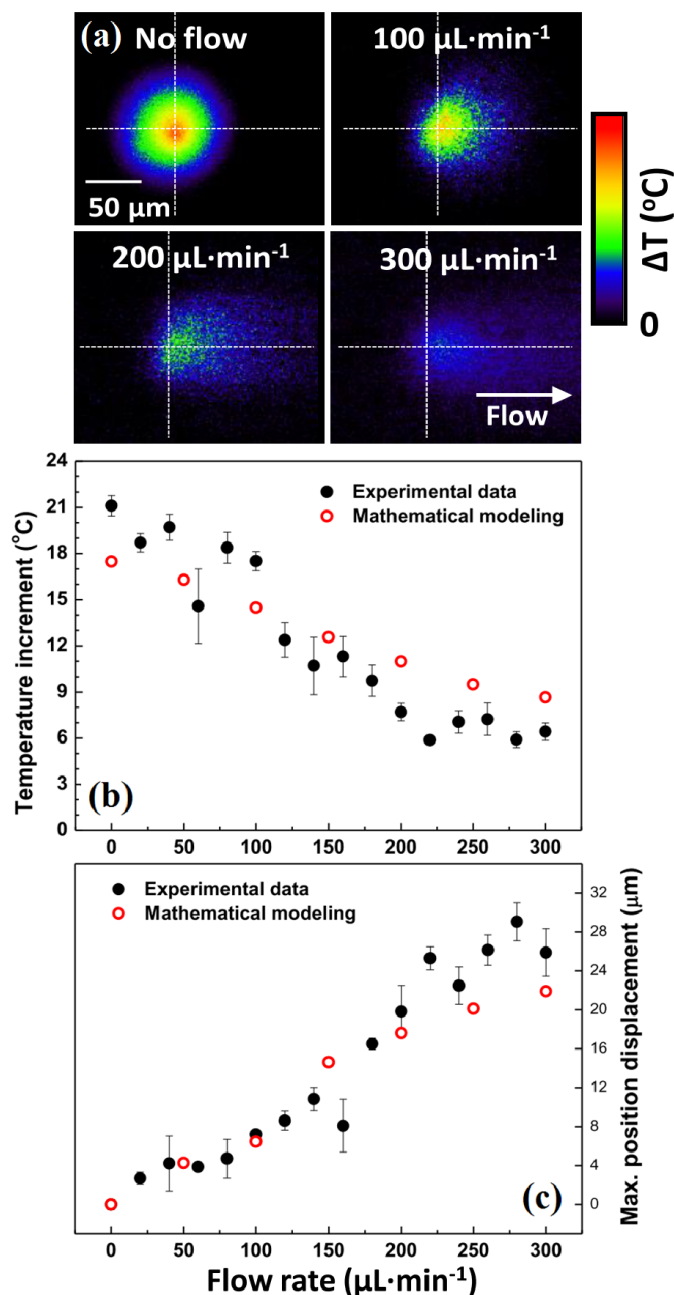
Figure 3.22: Temperature inside a single channel microfluidic device illuminated with 300 mW of 980 nm light. (a) experimental data showing temperature change with flow rate, (b) comparison of predicted and actual temperature, (c) change in position of maximum intensity with flow rate.

3.5 Conclusion

We are interested in understanding the microfluidic devices we fabricate, specifically how temperature distribution is affected by the flow rate inside them. To investigate this we used two dye fluorescence thermometry to measure the temperature inside devices fabricated in fused silica through ULI and HF etching and PDMS devices purchased commercially. We found the method to be effective in producing measurements with a high degree of temporal and spatial accuracy limited only by the microscope systems being used to conduct the reading. A comparison was made between experimental measurements of temperature in a microfluidic device and a COMSOL model. The prediction and measurement matched within experimental error indicating that the measurement technique is effective.

Having established the technique worked we examined the effects of flow rate and observed, as would be expected, that the maximum change in temperature decreases as flow rate increases. The maximum change under typical operating conditions was 5 °C, enough to cause changes in biological cell function [63]. As this device is a cell sorter this result may be of concern for example for any human cell line which is intended to be separated then cultured as not maintaining a temperature of 37 C, or the cell experiencing over 40 C for a short period of time will decrease cells' viability. Other conclusions are that the position of maximum intensity is not fixed at the point of maximum optical intensity but can actually move down the channel which may be of interest in any experiments involving optical trapping and heating of the trapped sample. From our results we see that the system can take up to a second to stabilise after laser power is changed, depending on channel size and flow rate. Readings taken in this time will vary depending on how far the process has progressed so the measurement should be taken several seconds after laser power or flow rate has been changed to allow the device's temperature to stabilise.

These results, showing our ability to measure temperature in microfluidic devices, will be of significant use in any future work involving biological samples, where heating may cause damage, or where temperature control is critical. This will also be of interest in devices which depend on well controlled fluid flow such as cell sorters where heating may affect the sorting efficiency through the creation of currents within the device.

4. Imaging Flow Cytometry

4.1 Introduction: High Throughput Medial Diagnosis

4.1.1 Flow Cytometers

Flow cytometers are a well-established and widely used tool in both biological research and in commercial applications. They were first proposed in the 1960s [72] and as the name implies flow cytometers look at cells, or particles, in flow. A schematic of such a device is shown in *Figure 4.1* where cells flow through a channel and are illuminated with a laser. To count cells and give an indication of their size the forward scattered light is recorded for each cell. To give an indication of cell complexity side scattered light is recorded. Through this simple technique it is possible to rapidly count and differentiate between cells in a population. For biological research additional analysis is conducted by making use of fluorescence stains, in the cell or on the cell surface, which are illuminated by the laser and recorded using optical filters before a detector. Many stains have been developed which bind to or are taken up by specific bacteria or cells and the stains can give an indication of cellular properties such as membrane integrity or glucose uptake [73]. Using these stains, it is possible to extremely accurately identify specific cells or properties of cells in a population with count rates as high as 100,000 cells per second [1].

Flow cytometers have been used for inspecting water quality where samples taken after each purification step in a purification system gives an indication of how effective each step has been. In one specific example flow cytometry was used to measure a decrease in cell population from 1×10^6 cells.ml^{-1} to below the experimental detection limit of 200 cells.ml^{-1} [74] illustrating how flow cytometers can accurately count both large and small concentrations of cells in samples.

Incorporating a microscope into a flow cytometer in addition to scatter and fluorescence measurements adds further functionality. Imaging flow cytometers, first proposed in 1979 [75], give additional information about cell orientation, morphology and fluorescence location inside cells.
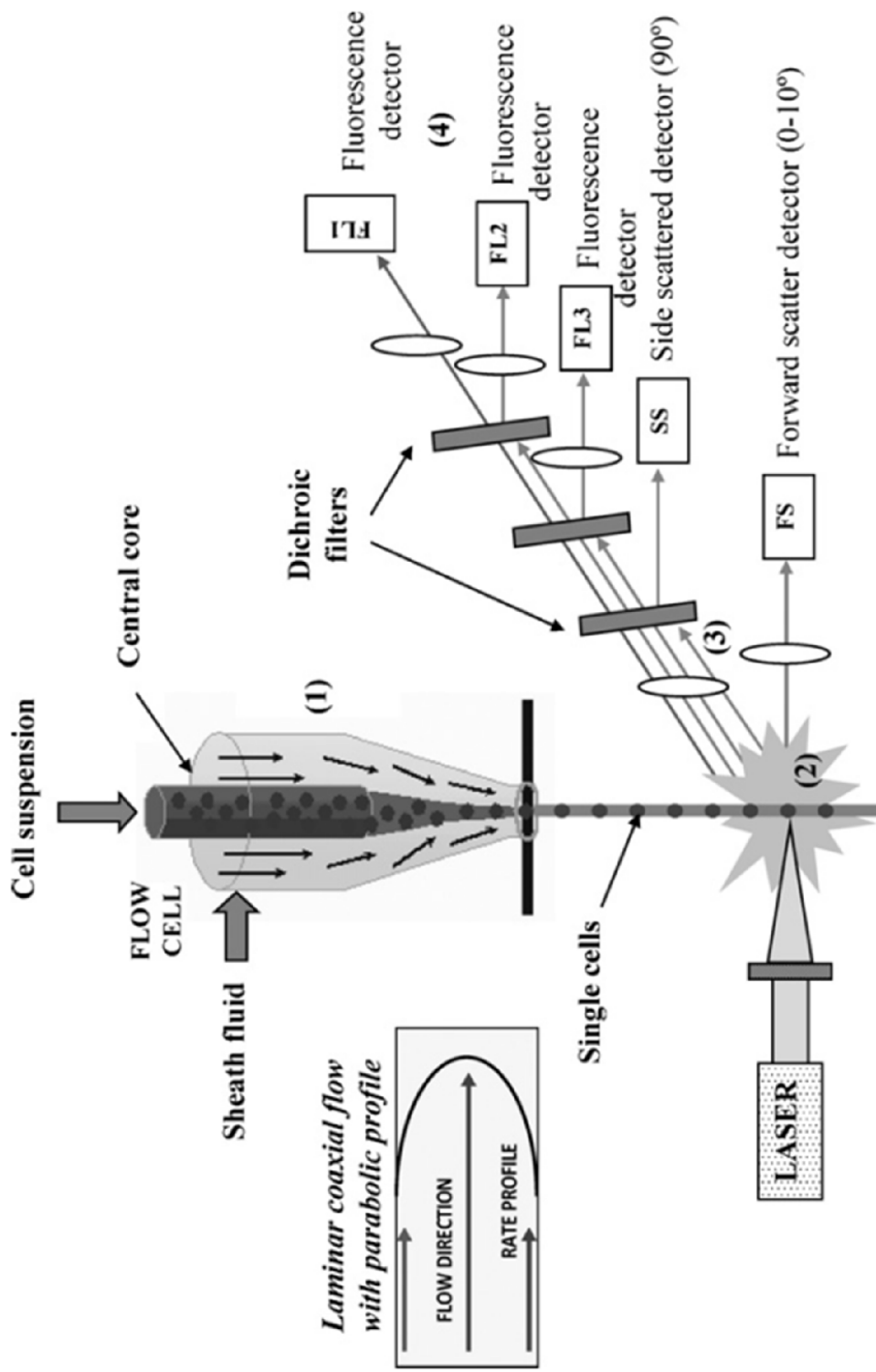
Figure 4.1: Schematic representation of a flow cytometer with cells flowing past an excitation laser. Detected parameters are forwards scatter, side scatter and fluorescence [1].

4.1.2 Microfluidic Flow Cytometers

The fabrication of microfluidic devices which mimic or exceed the capabilities of current experimental equipment has been one of the aims of the field since its beginning. Applying microfluidics to flow cytometers has the potential to decrease their cost and size opening up their use to every research laboratory and to clinical point of care.

Demonstrations to date have mostly made use of PDMS due to its widespread availability and ability to fabricate highly defined channels. Demonstrations of imaging flow cytometers manufactured using PDMS have achieved throughputs of up to 20,000 cells per second [76].

We are interested in using ULI to fabricate imaging flow cytometers in fused silica. The advantage of this over current examples is that fused silica is a more reusable and durable material than PDMS and therefore making use of fused silica could increase the viability of microfluidic flow cytometers in real world settings. It is more reusable as PDMS, unlike fused silica, absorbs some small molecules making them impossible to sterilise contaminating future experiments [77, 78].

Our proposed design for such a device is shown in *Figure 4.2* where we have 2 inlets and 8 channels. The use of multiple channels allows for multiplexing of imaging depending on how many channels fit within the field of view of the imaging microscope. We chose 8 channels as, with our current channel separation, this is more than can be imaged by most high magnification objectives.
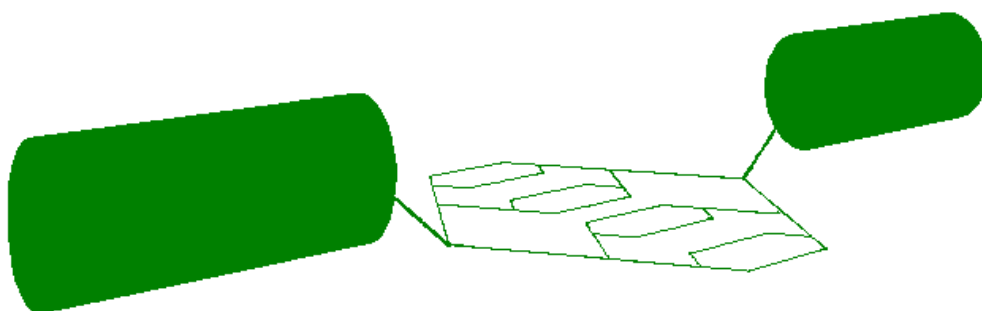
Figure 4.2: Wireframe design of microfluidic flow cytometer.

After fabricating the device, we tested its ability to capture images of cells. Using red blood cells, we achieved throughputs of up to 4,700 cells per second. In order to confirm

that our chosen material was more reusable than PDMS we made use of rhodamine dye flowing it through two similar devices then flushing with water. The residual fluorescence in the PDMS device was significantly greater convincing us that our reasoning was correct.

4.1.3   3D Cell Imaging

Having fabricated a microfluidic imaging flow cytometer and seen that it effectively counted and imaged cells we next considered how we could incorporate more features into the device, increasing its usefulness and further increasing the compactness of current diagnostics. 3D focal stack collection is such a feature which can be integrated into the device with only slight modification.

The 3D imaging of cells, and also of cell clusters, is of use in a wide variety of applications where variation in shape can give information about cell health or where fluorescent stains have been added and it is necessary to observe its distribution throughout a cell. 3D images are typically built up using a series of points or sections of a cell such as in a confocal microscope system which rejects out of focus light. By scanning a cell in a 3D raster pattern an image is built up point by point. This process can be automated and provides a high degree of accuracy but is a slow method, relative to others which are available, potentially taking several minutes to image a single cell depending on the system used [79]. An alternative is the light sheet microscope where structured illumination is used to illuminate an entire plane of a cell or structure at once thereby only requiring the sample to be translated in one dimension to create a 3D image of the sample. This method has proved successful, and can be applied to wide fields of view, but sample preparation can also prove difficult and non-standard microscope systems are required. A third method, and the one we are interested in is to flow cells past a microscope system at an angle so that the cell transverses the focal plane. Multiple frames therefore show different planes of the cell which can be combined into a 3D focal stack. This method has been successfully demonstrated using blood samples to produce focal stacks of red blood cells and leukaemia cells with a sectioning resolution of 675 nm [80, 81].

This method, using tilted microfluidic channels, has the potential for high throughput automated generation of 3D focal stacks of cells. To date these devices have made use of microfluidic channels which are parallel to the overall microfluidic device, requiring the entire device to be tilted relative to the imaging microscope system. This is a small but

significant limitation as it requires the addition of rotation control to the microscope system which is not a standard feature and could potentially be costly or impossible to introduce depending on the manufacturer.
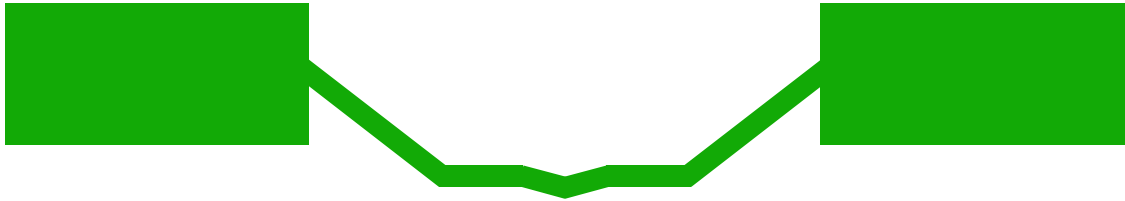
Figure 4.3: Angled channel wireframe design of microfluidic device.

Using the 3D freedom inherent to ULI device fabrication we can modify our device with an angled channel relative to the device surface allowing it to be flat mounted onto a microscope system. Our proposed modification is shown in *Figure 4.3* where we introduce a small tilt to the central section of our device. Our device has multiple channels and it is possible to introduce a different tilt into each one. As the ideal case is one where a cells move its own height as it transverses the microscope field of view a device with multiple channel tilts would be of use if multiple sized cells are to be used.

We fabricated devices using the new design then inspected their ability to create 3D focal stacks first using microspheres, which we know to be spherical with a diameter of 4 μm. This being successful we then imaged the nucleus of bovine sperm cells, measuring approximately 7 x 3 x 1 μm [82], producing 3D images with a vertical step size of ~15 nm.

4.2   Device Design and Fabrication

Our design for a flow cytometry device is shown in *Figure 4.2*. This was fabricated in fused silica through ULI and HF etching to take advantage of the chemical resistance of the material and 3D capabilities inherent to the method. The use of 8 parallel channels in the device allows us to record all simultaneously, in order to increase the throughput of the device. Depending on the field of view of the imaging objective used, the number of channels visible will vary and it was decided 8 channels were sufficient for most of the objectives we would use. The channels were angled to approach the surface so that objectives with low working distances could be used.

As this work was conducted in collaboration with researchers at the Indian Institute of Science (IISc) we decided to look at red blood cells as Sickle cell disease is a disease is

relatively common in India compared to other countries, affecting up to 20% of people in some areas. Sickle cell disease is an inherited condition which affects the shape of red blood cells causing them to become misshapen, reducing their ability to carry oxygen and increasing risk of infections. It is currently diagnosed by either an automated full blood count using flow cytometry or manual inspection of a blood film on a microscope slide. The former method results in high throughput and provides histograms of cell shape while the latter method is able to identify abnormal cells with specific shapes but is much slower. The use of microfluidic imaging flow cytometry has the potential to provide high throughput, analyse the shape of cells providing additional information compared to normal flow cytometry, reduce costs and reduce the sample sizes required. Red blood cells have an average diameter of 7 μm so our channels should be slightly larger than this.

A parameter scan was performed to find those parameters which produced the highest etching selectivity as described in, *Section 2.5*. The laser used was a Fianium HE-1060-1J femtosecond laser and for the parameter scan a series of straight lines were inscribed in a fused silica substrate then etched in HF. From our previous work we know that a repetition rate of 500 kHz, pulse length of 330 fs and 0.4 NA objective will give the optimal results leaving power and translation speed to be investigated. Doing so we found the optimal parameters for etching to be:

Inscription Power -	250 mW
Writing Speed -	1 mm.s^{-1}
Repetition Rate -	500 kHz
Pulse Length -	330 fs
Objective NA -	0.4

Table 4.1: Optimised inscription parameters for etching using a Fianium laser system.

Using these parameters, devices were inscribed then etched for approximately 20 hours in 5% HF with the exact time varying between devices. Each device was removed when it had completed etching in order to achieve the desired central channel size. The devices are shown post etching in *Figures 4.4* and *4.5* where the multiple channels, *4.4*, and how they approach the surface, *4.5*, are visible.
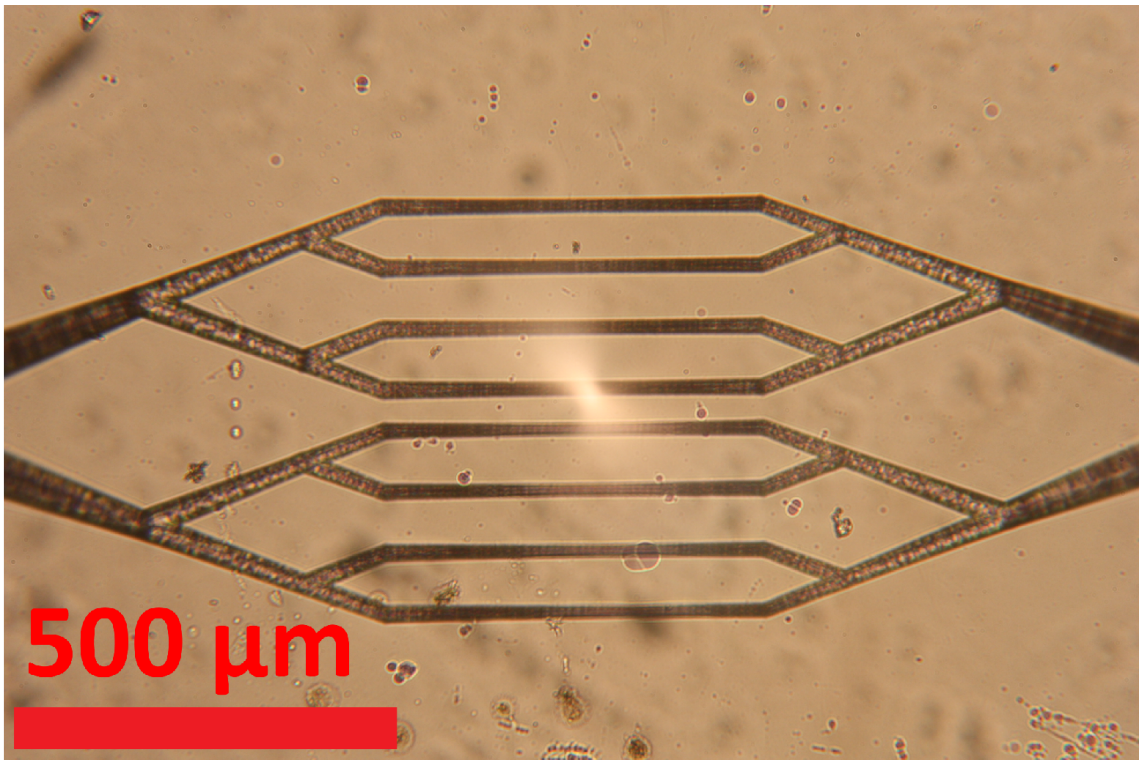
Figure 4.4: Top view of etched microfluidic device with 8 parallel channels.
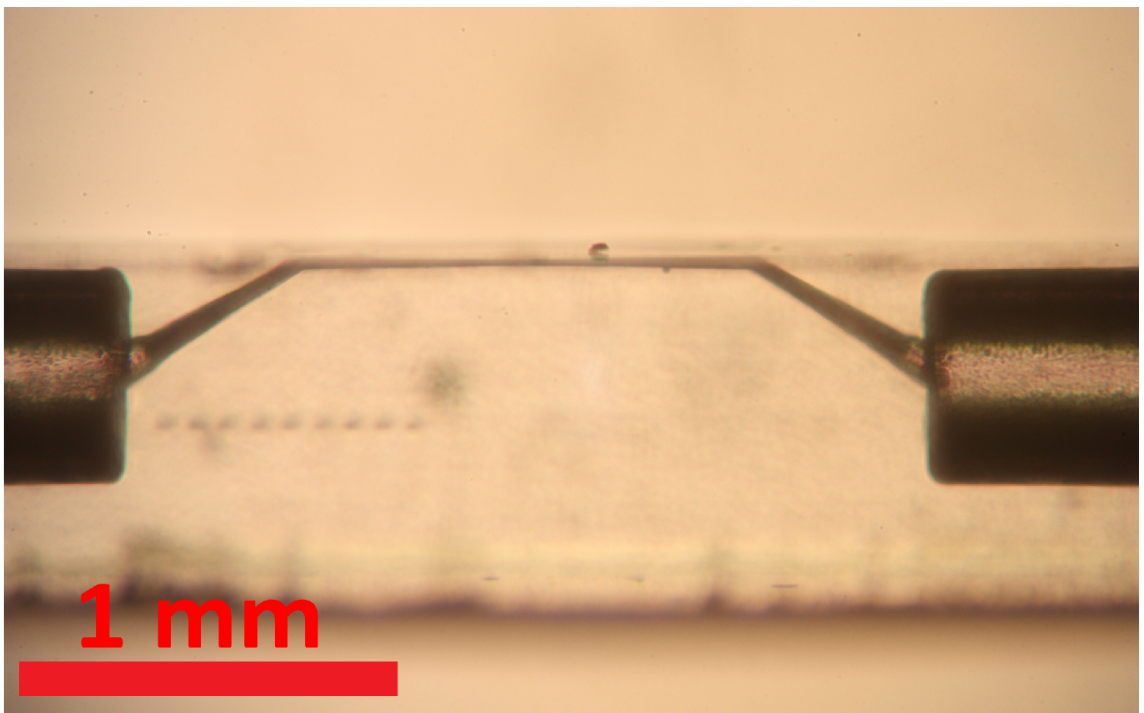
Figure 4.5: Side view of etched microfluidic device showing the channel approaching the surface.

Taking advantage of the fast prototyping abilities of ULI we varied the dimensions of each device to obtain a range of channel sizes after inscription. This was done by varying the number of scans in which make up each channel. There is additional variation due to the unique etching of each device. The final channel sizes were:

Parameter	Minimum (µm)	Maximum (µm)
Channel Height	16	35
Channel Width	2	22

Table 4.2: Channel sizes after etching.

The majority of devices meet the requirement of a diameter over 7 µm necessary for red blood cells. While this is the minimum size we also wanted to limit the maximum size as well to reduce the variation in cell position relative to the focal plane of the imaging microscope. After etching, microfluidic tubing was bonded to the inlets of the device so it could be used with a syringe pump. The tubing was made from PEEK with an inner diameter of 100 µm and outer diameter 360 µm. For bonding we made use of Thorlabs MIL-A-3920 UV curing optical adhesive which is pulled into the inlets in its liquid state through capillary action before being set with a UV lamp.

4.3 3D Focal Stack Microfluidics

The initial devices shown in *Figures 4.4* and *4.5* have a straight channel in their centre. These devices were used to perfect our flow cytometry technique and are not suitable for generating 3D focal stacks despite a portion of the channel connected to the inlet being angled. This is because it is inclined at a high angle meaning the cells would pass through the focus quickly limiting the number of sectional images that could be taken. Ideally a cell should move a distance equal to its own height vertically as it crosses the microscope field of view to maximise the number of imaged slices taken through the cell.

In order to obtain the desired degree of movement for cells traveling through the central section of the device they were modified with a tilt as seen in *Figure 4.3*, this being 1°, 2° or 5°. As before, a parameter scan was conducted, using an IMRA µ-Jewel femtosecond laser to determine optimal etching parameters. These were found to be:

Power -	350 mW
Repetition Rate -	500 kHz
Pulse Length -	360 fs
Translation Speed -	1 mm.s^{-1}
Objective NA -	0.4

Table 4.3: Optimal inscription parameters for etching using an IMRA laser system.

The inscription laser spot size is smaller than our desired channel size so multiple parallel scans are used to construct it. It was observed that after etching this resulted in a residual set of lines being visible in the channels which hampered imaging. While increasing etch time would remove this as the acid moved into unmodified areas it would also result in larger channels which would be undesirable. To solve this, we investigated the effect of increasing the number of scans and found that increasing them removed the residual lines after etching. Having learnt this the change was incorporated into all future devices, where imaging or reducing scattering is important. Two other improvements were made for ease of device use. An inscription line was made below the centre of the channel to mark its position and lines numbering the device were added. This was previously done using a label attached to the inlet tubing but was found to occasionally become detached.

Using our optimised etching parameters and incorporating these improvements into the devices we inscribed then etched them in 10% HF for approximately 13 hours. The resulting devices are shown in *Figures 4.6* and *4.7* where the changes described above can be seen. The channel sizes varied and were measured to be:

Parameter	Minimum (µm)	Maximum (µm)
Channel Height	10	19
Channel Width	40	43

Table 4.4: Channel dimensions after microfluidic devices have been etched in 10% HF for approximately 13 hours showing the variation in channel size.

As before PEEK tubing, inner diameter 100 µm and outer diameter 360 µm, was bonded to the inlets using Thorlabs MIL-A-3920 UV curing glue. It was necessary to use the minimum amount of glue possible so that the devices would sit flat on microscope translation stages. Excess glue extending beyond the base or top surface would result in

a random tilt and instability. To give an indication to the reader of the scale of completed devices one is shown in *Figure 4.8* next to a ruler and 10 pence coin.
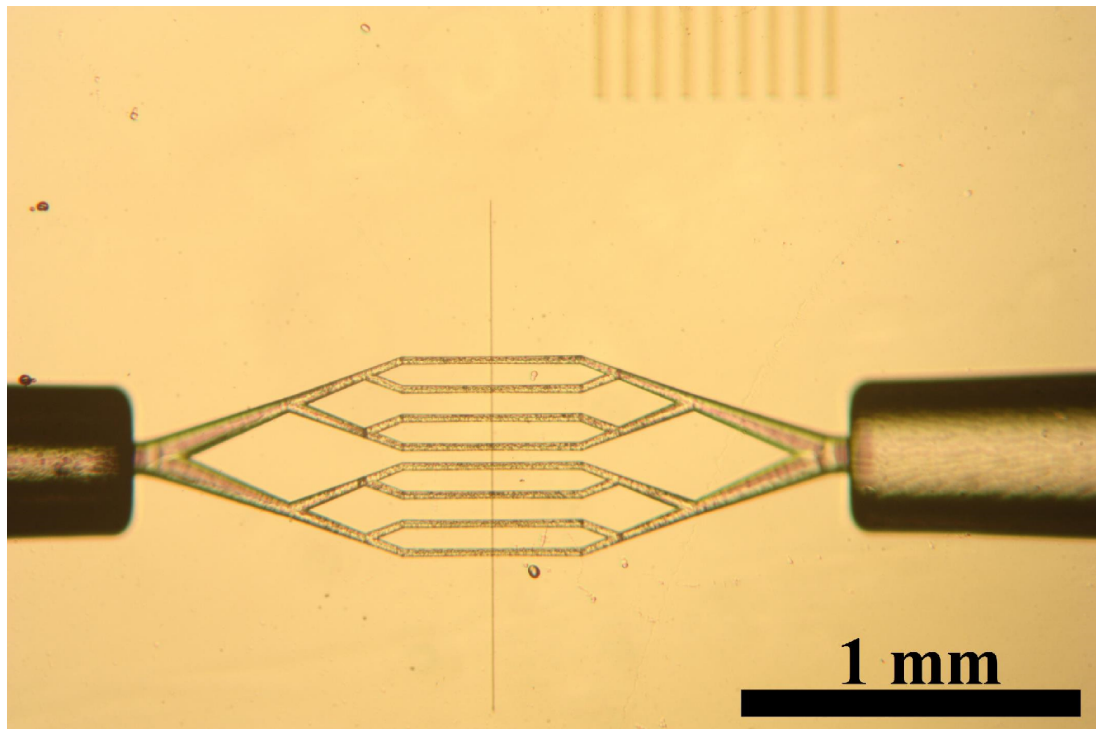
Figure 4.6: Top view of etched angled microfluidic device. The vertical line in the middle of the diagram is below the channels to indicate the centre.
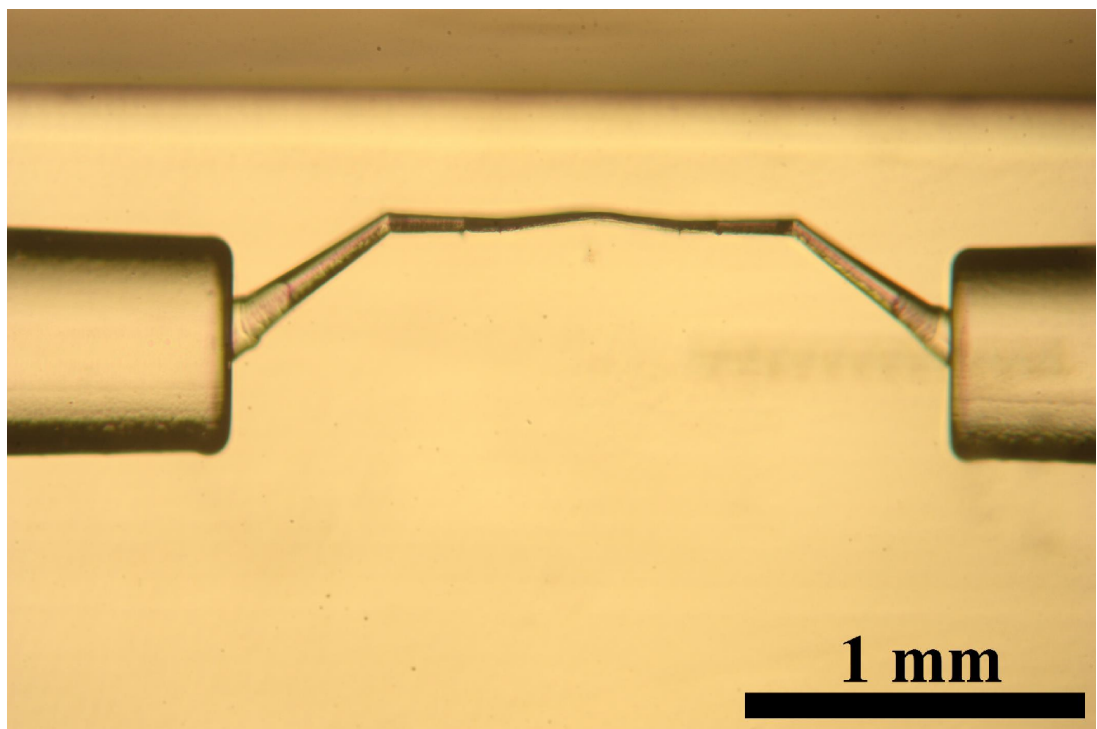
Figure 4.7: Side view of etched angled microfluidic device. The tilt of the central region is 5°.
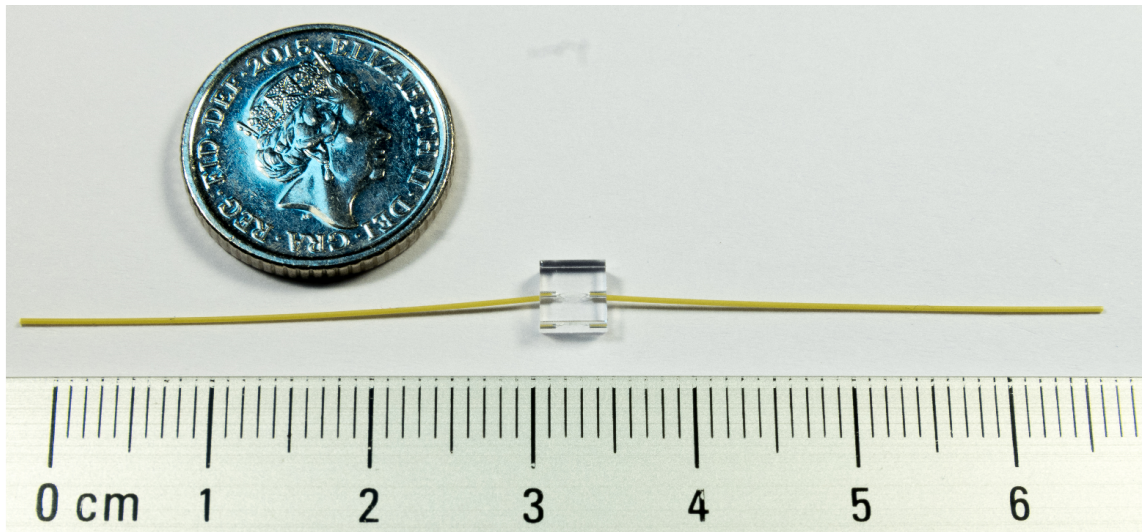
Figure 4.8: A completed device with ruler for scale. The coin is a British 10 pence.

4.4   Experimental Results

The completed devices were transported to the IISc and further investigations conducted in collaboration with researchers there to take advantage of their microscope facilities and expertise in image analysis. The aim of these experiments was to evaluate the device's effectiveness for use in flow cytometry and 3D imaging.

The flow cytometry devices were imaged using a simple microscope system as shown in *Figure 4.9* consisting of an illumination system and microscope objective coupled with an imaging sensor. The goal in keeping this system as simple as possible was that it could be mass produced and distributed widely making use of disposable microfluidic chips to increase the availability of flow cytometry diagnostic techniques. Illumination was provided by an LED making use of Köhler illumination, which is a method that ensures the illumination source is defocused at the imaging plane to ensure an even illumination.
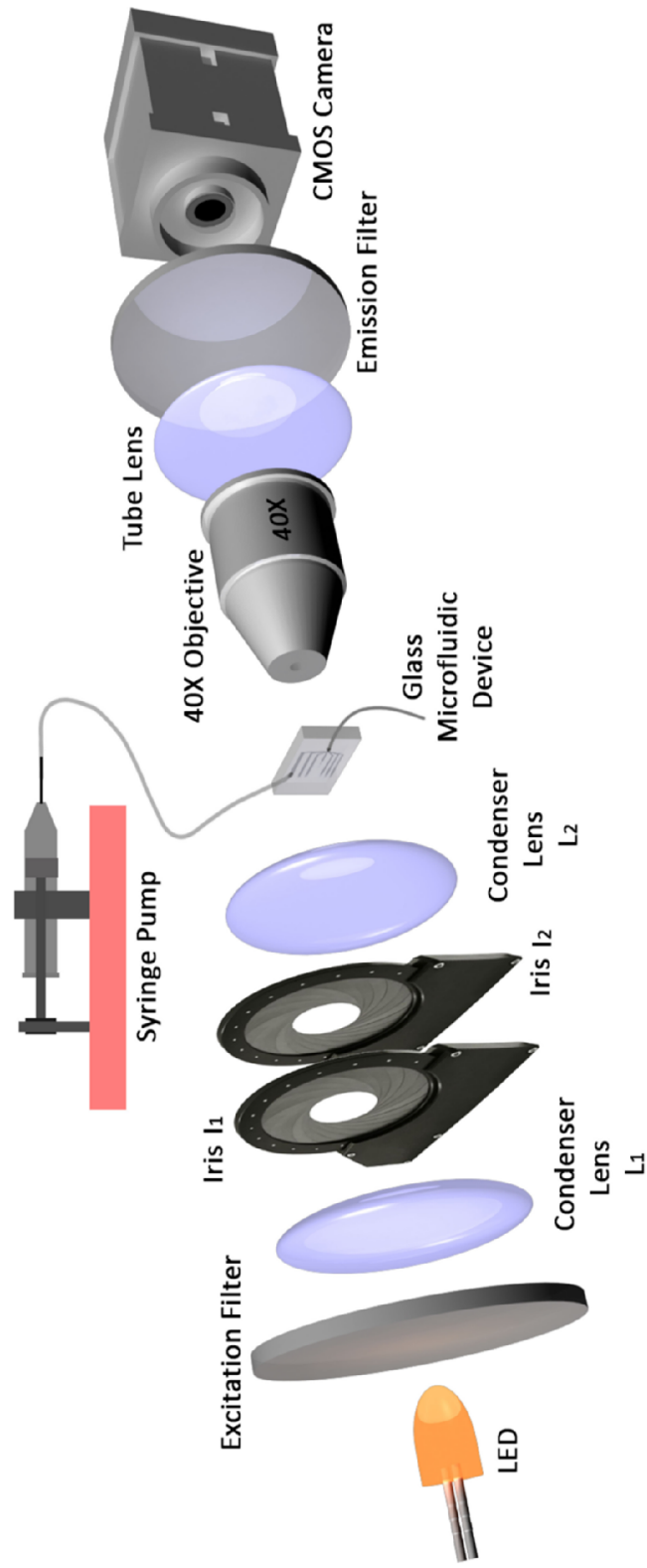
Figure 4.9: Experimental setup with microfluidic device and simple microscope system. Excitation and emission filters are only needed when examining fluorescent samples.

We made use of red blood cells in our investigation flowing samples through the device and recording videos using sensors. The cells were separated by centrifuge from whole blood obtained from the IISc health clinic. These samples were from healthy donors; further studies will examine blood from unhealthy donors for disease detection. Samples were pumped through our microfluidic device using a syringe pump, NE-1000 New Era Pump Systems. Device clogging proved to be an issue when passing thousands of cells, which had not been predicted. It was found that mounting the device vertically prolonged the lifetime of devices as when mounted horizontally gravity caused cells to fall and collect at the inlet and outlet. In future devices we will consider more thoroughly how they will operate over long periods of time with large numbers of cells or particles passing through them.

The devices were imaged using the simple microscope system shown in *Figure 4.9* and a number of imaging sensors utilised to see if we could meet the aim of producing a low cost, simple system. Projecting the images onto a screen was effective for aligning the system and the use of a standard Samsung camera, EK-GC100, was sufficient to capture videos of cells in flow. For the highest possible throughput of we made use of a Mikrotron EoSens MC1362 CMOS camera which has a framerate of 500 Hz, increasing if fewer pixels are read out.

Videos were taken of cells in flow then transferred to a computer and separated into individual frames for use with MATLAB. Analysis consisted of preforming background subtraction on the frames to highlight cells then using thresholding to automatically identify them and determine their dimensions. To differentiate between cells and any debris present a minimum and maximum threshold for cell area was used, this being determined by measuring the average area of several hundred cells. A manual check showed that this method correctly identified around 95% of cells with the majority of errors being due to clumps of cells being misidentified as individual cells. This could be corrected in future work through the use of more sophisticated computer algorithms using edge detection [83].

The process is demonstrated in *Figure 4.10* where we have an image without cells (a), an image with cells (b) and the subtraction of one from the other (c). A selection of different cells is given in (d) showing the slight variation in their size and shape. Red blood cells are expected to have a doughnut shape which we would expect to appear as either circular or oval in our frames depending on their orientation relative to the imaging objective but instead our images all appear circular. This may indicate that our cells are in non-ideal

conditions or that our microfluidic channels preferentially orientate the cells in a particular direction.
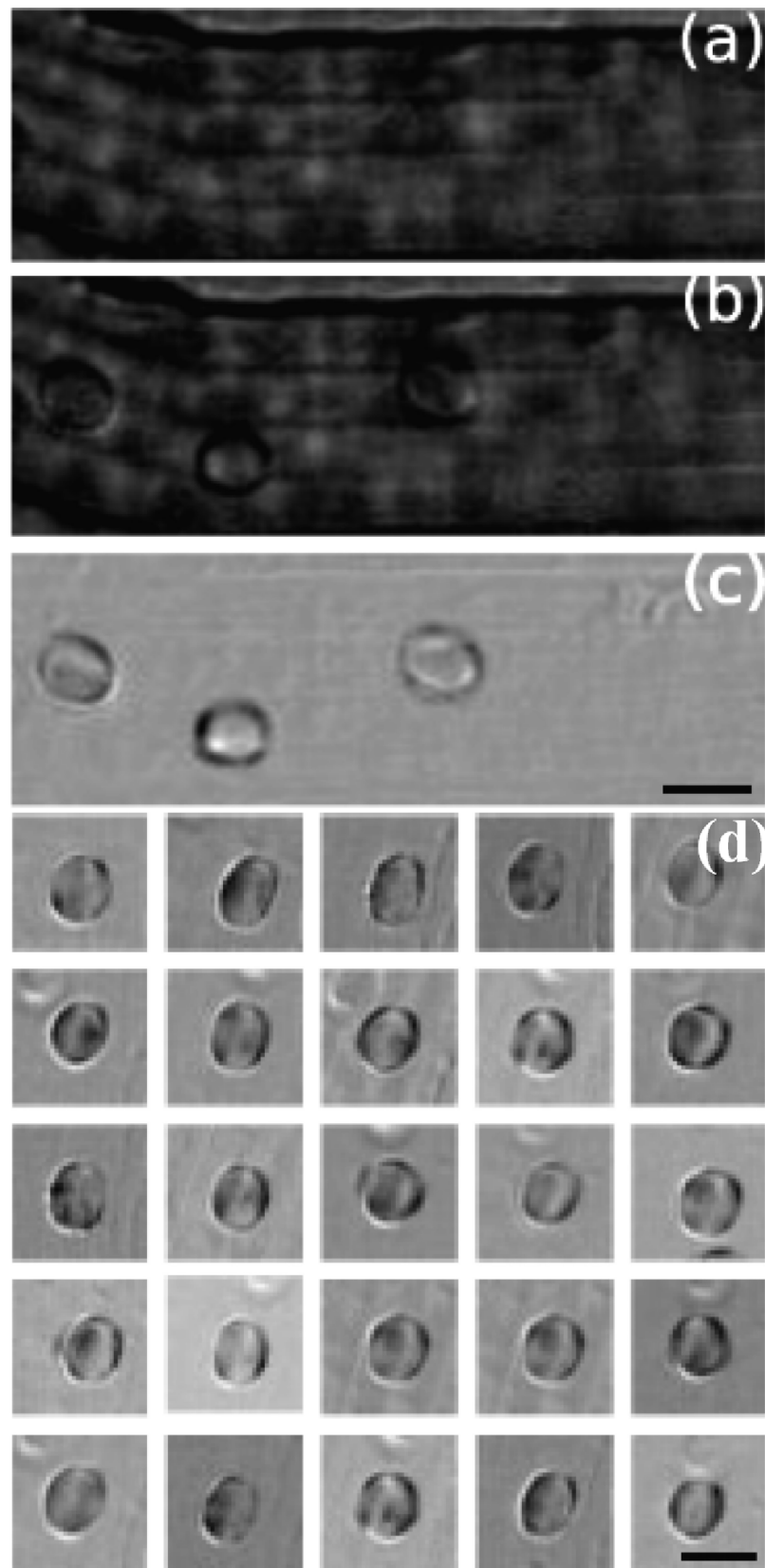
Figure 4.10: Cells identified through image analysis. Scale bars are 10 μm. (c) is the resultant image obtained by subtracting (a) from (b). (d) is a selection of different cells.

As the frame rate of the camera used is dependent on the number of pixels read out we reduced the number of pixels to only those which showed the channel and ignored the surrounding areas. The flow rate of the syringe pump was then increased to the maximum rate which did not result in cells being missed between frames or blurred. Doing this we obtained a maximum count rate through a single channel of 4635 cells per second with a framerate of 2550 fps, exposure time of 10 µs and flow rate of 400 µL.hr^{-1}. This is comparable to PDMS flow cytometry devices which have count rates of up to 20,000 cells per second [76].

As we had achieved our aim of fabricating a fused silica flow cytometer we next moved on to a direct comparison of fused silica and PDMS looking at reusability and chemical resistance. During our experiments we found that after tens of thousands of cells have passed through a device it typically builds up some debris in the channel. This contamination would render the results from any repeat experiment using the same device invalid due to contamination. To remove the debris, we used hydrochloric acid though any chemical which does not react to glass but dissolves cells could be used. This is not possible in PDMS as it can absorb small molecules [77, 78]. To demonstrate this, we made use of two similar devices, one fused silica and one PDMS. Rhodamine B dye was pumped through each device as shown in Figure *4.11* where (a) and (b) show rhodamine B in the PDMS and fused silica device respectively. After pumping the rhodamine through the devices for several minutes the feed was replaced with water and flushed to clear the channels. The fluorescence of the devices was then observed to see if dye remained in the channel as seen in (c) PDMS and (d) fused silica. There is a clear difference in residual fluorescence indicating the PDMS device has absorbed dye into the material surrounding the channels. This convinces us that fused silica is indeed the more suitable material for this type of experiment and we will continue its use for long term experiments or multiple repeat experiments.
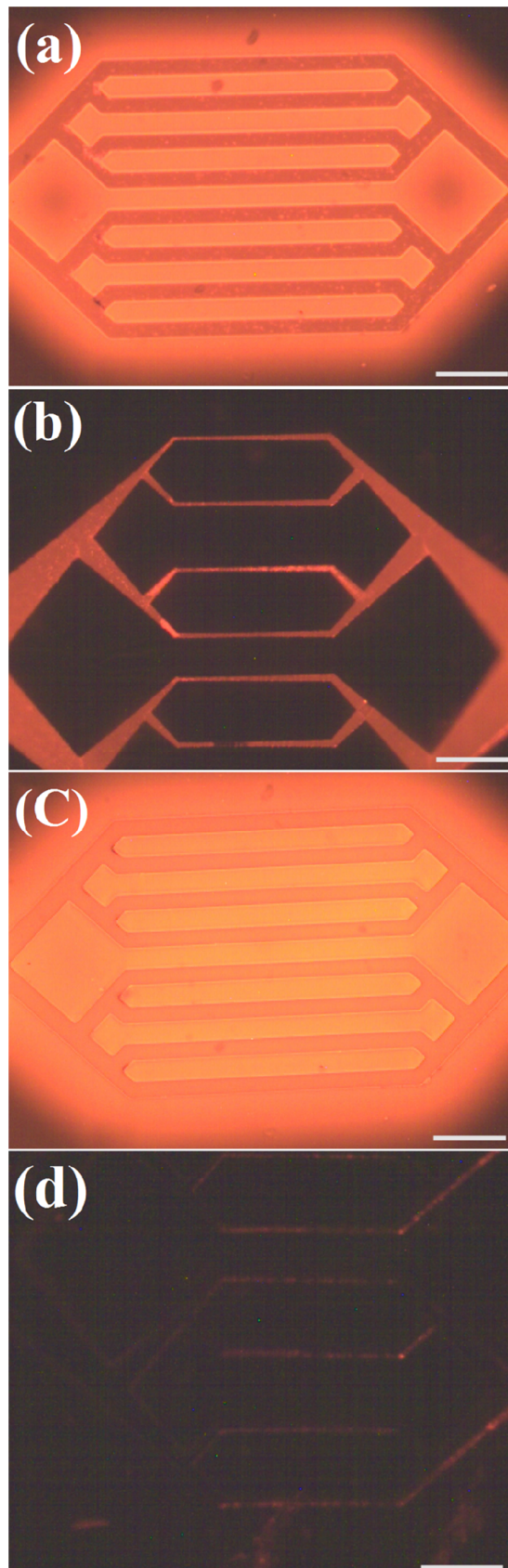
Figure 4.11: Fluorescence from fused silica and PDMS devices with Rhodamine B and after being flushed with water. (a) PDMS with dye, (b) Fused silica with dye, (c) PDMS flushed and (d) Fused silica flushed. Scale bars are 500 μm. There is a blockage in one of the channels in (b) due to cell debris.

Having found our microfluidic imaging flow cytometer was effective at counting cells we next decided to modify it to collect 3D focal stacks by angling the central channel. To determine if our device was effective we first made use of particles with a known shape and size. These were 4 μm microspheres, labelled with Fluorescence Isothiocyante (FITC), pumped through the device using a syringe pump, NE-1000 New Era Pump Systems. Flow rate was minimised to maximise the number of frames taken of each microsphere as it moved through the focus. Videos were recorded using a Zyla 5.5 camera set to 200 fps and 500 μs exposure. Videos were separated into individual frames, a small number of these are shown for a single microsphere in *Figure 4.12* (a). In these images it is possible to see a slight change in shape as the microsphere moves through the focus but the presence of out of focus light distorts the image making the change difficult to see.

It is assumed that the cells do not rotate during the short time in which images are taken. Microfluidic devices typically operate in the laminar flow regime so there is no turbulence in the channel which could cause the target particle to rotate. If there were some rotation this would lead to a distortion of the shape when separate images are combined into a single object. While it was not investigated at the time it could be determined if our assumption, that the particle does not rotate, is correct by increasing our field of view and using an asymmetric target such that any slight rotation would be detected over a larger distance of travel.

To improve our raw images, we made use of blind deconvolution. This process estimates both the distortion due to the point spread function of the fluorescence microscope and the contribution from out of focus fluorescence [84]. The resulting images are shown in *Figure 4.12* (b) where the change in radius as the microsphere moves through the microscope focus is now clearly apparent. A final step to remove artefacts generated by the deconvolution step gives our final images in *Figure 4.12* (c).

The resulting images were combined into a 3D focal stack by finding the centre point of each slice. This gives us an image of the microsphere as shown in *Figure 4.13*. Measuring the size of a group of several microspheres as shown in *Figure 4.14* we determine their size to be 4.1±0.2 μm which is in good agreement with the manufacturers datasheet which gives a value of 4.2±0.2 μm. These results convince us of the accuracy of our imaging system.
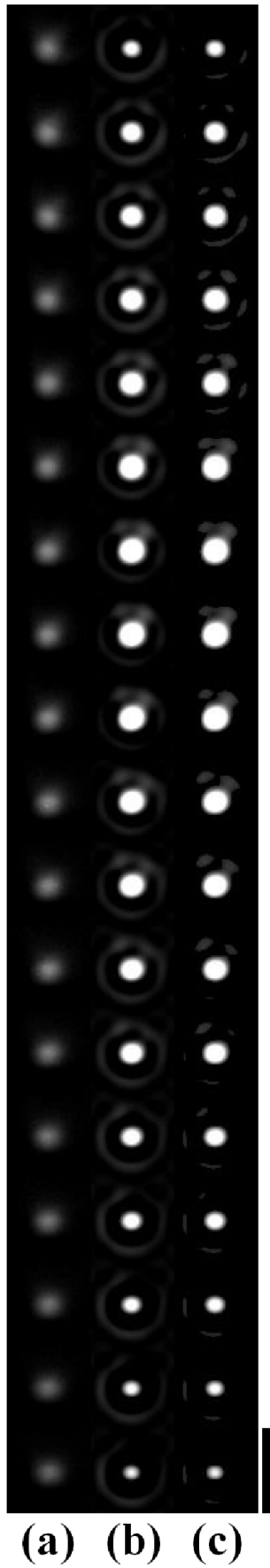
(a) (b) (c)

Figure 4.12: (a) Raw images of fluorescent microspheres. (b) Deconvoluted focal stack. (c) Imaged after removal of artefacts. Scale bar 10 μm.
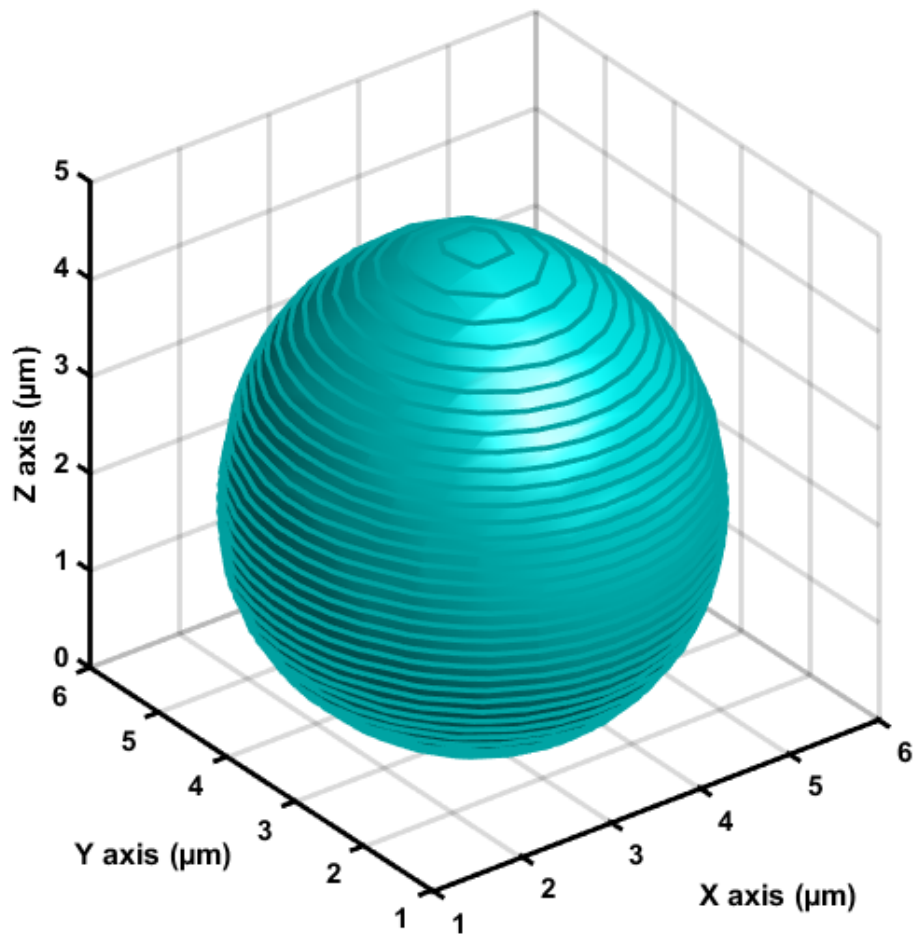
Figure 4.13: Composite image of 4 μm microsphere constructed from multiple imaged slices.
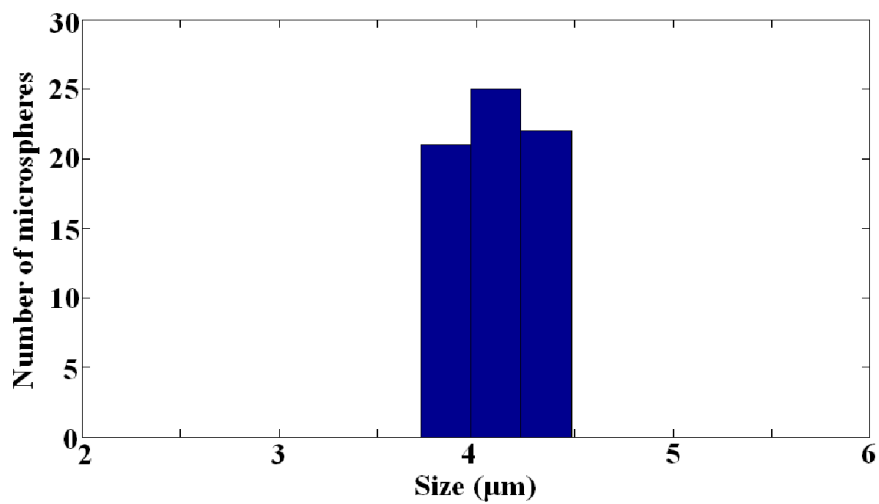
Figure 4.14: Histogram of microsphere size as measured by our system. The measured size of 4.1±0.2 μm is in good agreement with the manufacturers datasheet which gives a value of 4.2±0.2 μm.

The cell we choose to image next is bovine sperm cell nuclei stained with 4',6-diamidino-2-phenylindole (DAPI) with relevance in animal research. These were flowed through the device and videos recorded as before. Analysing the data produces focal stacks with a separation between slices of ~15 nm with 226 slices making up a single nucleus as seen in *Figure 4.15* . The expected size of bovine sperm cell nuclei is approximately 7 x 3 x 1 µm. The resulting image matches our predicted structure and demonstrates that our device is capable of imaging biological cells with a high resolution.
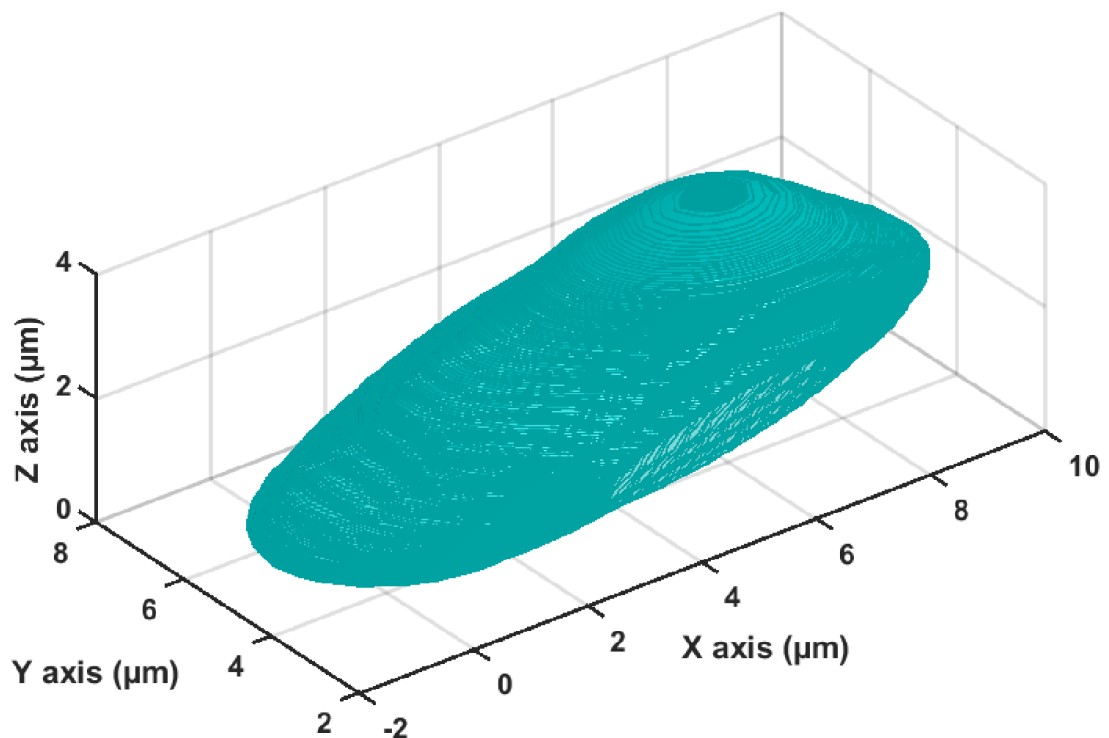
Figure 4.15: Composite image of 3 µm bovine sperm cell nucleus constructed from multiple images at different focuses.

4.5   Conclusion

The field of microfluidics offers the capability to improve upon current experimental equipment; miniaturising it, making it cheaper and improving availability. With this in mind we have applied our ULI fabrication techniques to flow cytometry which is widely used for cell counting, size analysis and investigation cell populations using fluorescent stains.

We fabricated a device consisting of channels optimised for use with red blood cells and using a basic microscope system observed count rates of up to 4635 cell per second. It is our hope that such devices may become available widely due to their low cost and ease of use compared to traditional flow cytometry systems. Our choice of fused silica was made as it is a more reusable and robust material than alternatives such as PDMS. We confirmed that this was the case using rhodamine dye and observed that a PDMS device suffered from significantly more staining that once made from fused silica. This convinces us that our choice of material is correct and that we should continue using it in future devices.

To improve the usefulness of our device and demonstrate how microfluidics can miniaturise current experimental equipment we integrated another function, 3D focal stack collection, into our device. Using ULI we made use of its 3D capabilities to create angled channels which cause cells to move through the focus of a microscope system allowing image stacks of a particle in different focal planes to be collected. Using microspheres and bovine sperm cell nuclei we obtained focal stacks with resolution of ~ 15 nm. This method of collecting focal stacks is faster and cheaper than current confocal and light sheet microscopy systems showing us the benefits of microfluidics in biological research.

5. Manipulating Objects with Dimensions Beyond the Resolution Limit of Light

5.1 Introduction: Fluorescence Imaging and the Manipulation of Single Particles

The use of fluorescent stains in biological imaging has added colour to what can at times seem like the monochrome world of the cell. Over time fluorophores have been developed which target specific areas of cells allowing objects of interest for example proteins to be tracked. Other fluorophores react to indicate cell health or behaviour for example monitoring calcium levels by changing emission intensity or wavelength. Methods have even been developed allowing us to gain information from below the diffraction limit, a possibility once thought impossible, through methods such as FRET and STED [39, 40]. For the above applications numerous fluorophores have been developed; dyes, proteins and quantum dots with emissions spanning the visible and near IR. While these are of tremendous use there are drawbacks which must be considered when deciding which to use. Dyes and proteins photobleach over time limiting the duration of experiments. They typically have broad emission spectrums which can hinder multi-colour labelling and they can only be excited in the UV or visible. The use of UV light can be damaging to cells and there are issues with scattering of light in the visible [85]. Qdots have narrow emission spectra and long lifetimes but are still excited in the UV and have additional problems with phototoxicity. While techniques have been developed to address the above issues, such as light sheet microscopy which can limit exposure times reducing photobleaching and the use of multi photon excitation to excite fluorophores using the infra-red light, these add complexity to experiments.

Upconverting materials are an alternative to the fluorescent stains described above [86]. They have narrow emission spectra and low photobleaching like Qdots but with the advantage of being both biocompatible and excited in the infrared. While it is possible to excite visible fluorescence through two photon absorption in the infra-red but this requires high intensities potentially damaging the sample being examined. Instead of this upconverting materials convert the light through excited state absorption allowing lower intensities to be used while taking advantage of the transparency of cells at these wavelengths and low auto-fluorescence being generated in the sample [87].

Fluorophores in general are too small to image directly due to the diffraction limit. Upconverting nanorods are a subset of upconverting materials with non-uniform shape which may make it possible to determine their orientation though indirect means

overcoming this problem with applications in imaging and manufacturing, such as the labelling of products [87]. The shape of nanorods can lead to polarised emission. This process is not present in all types of nanorods and the mechanism can vary. For nanorods smaller than the wavelength of light being used for illumination there is attenuation of light polarised perpendicular to the long axis of the nanorods but not that parallel to it [88, 89]. For nanorods with a diameter less than ~10 nm there may be additional effects due to quantum confinement [90, 91]. For materials where these effects are present it has been shown that their orientation can be determined through methods such as frequency doubling, though to date these methods have been difficult to implement, limiting their use [92].

We hypothesised that it would be possible to use a simpler method to determine nanorod orientation through examining their emission using a polariser and spectrometer. To investigate if this was the case we obtained samples of $NaYF_4:Er^{3+},Yb^{3+}$ nanorods from collaborators at Universidad Autónoma de Madrid and Wrocław University of Science and Technology, *Figures 5.1* and *5.2*. They had lengths of 1100±200 nm and diameters of 140±20 nm. As their diameter is much greater than 10 nm the dominant effect resulting in polarised emission will be the attenuation of light polarised perpendicular to the long axis of the nanorod. In more detail, as set out in [88], it is possible to imagine the nanorod as an infinite cylindrical wire. If the wire is placed in an electric field the component parallel to it will not be attenuated at the interface, *Equation 5.1*, while the component perpendicular to the wire will be attenuated according to *Equation 5.2*. where E is electric field and ϵ the permittivity.

$$E_{\parallel} = E_{0\parallel}$$

<div align="right">Equation 5.1</div>

$$E_{\perp} = \frac{2\epsilon_0}{\epsilon + \epsilon_{\perp}} E_0$$

<div align="right">Equation 5.2</div>

Our first experiments made use of a single beam optical trap to demonstrate that we could trap single nanorods. Although this was successful we found that the nanorods orientated with their long axis parallel to the optical axis resulting in a uniform spectrum when sampling the emission, viewed through the objective, with a polariser. Moving to a dual beam optical trap, we were able to control their orientation of the nanorods in 3D. This in itself is important if we are to use the nanorods in experiments as it allows us to arrange

them in a controlled, pre-determined manner. Having rotated the nanorods in 3D we then observed that their emission varies when they are rotated relative to a polariser. This demonstration of a simple method of both rotating and determining the orientation of upconverting nanorods makes their use in both fluorescence imaging experiments and manufacturing much easier to implement.
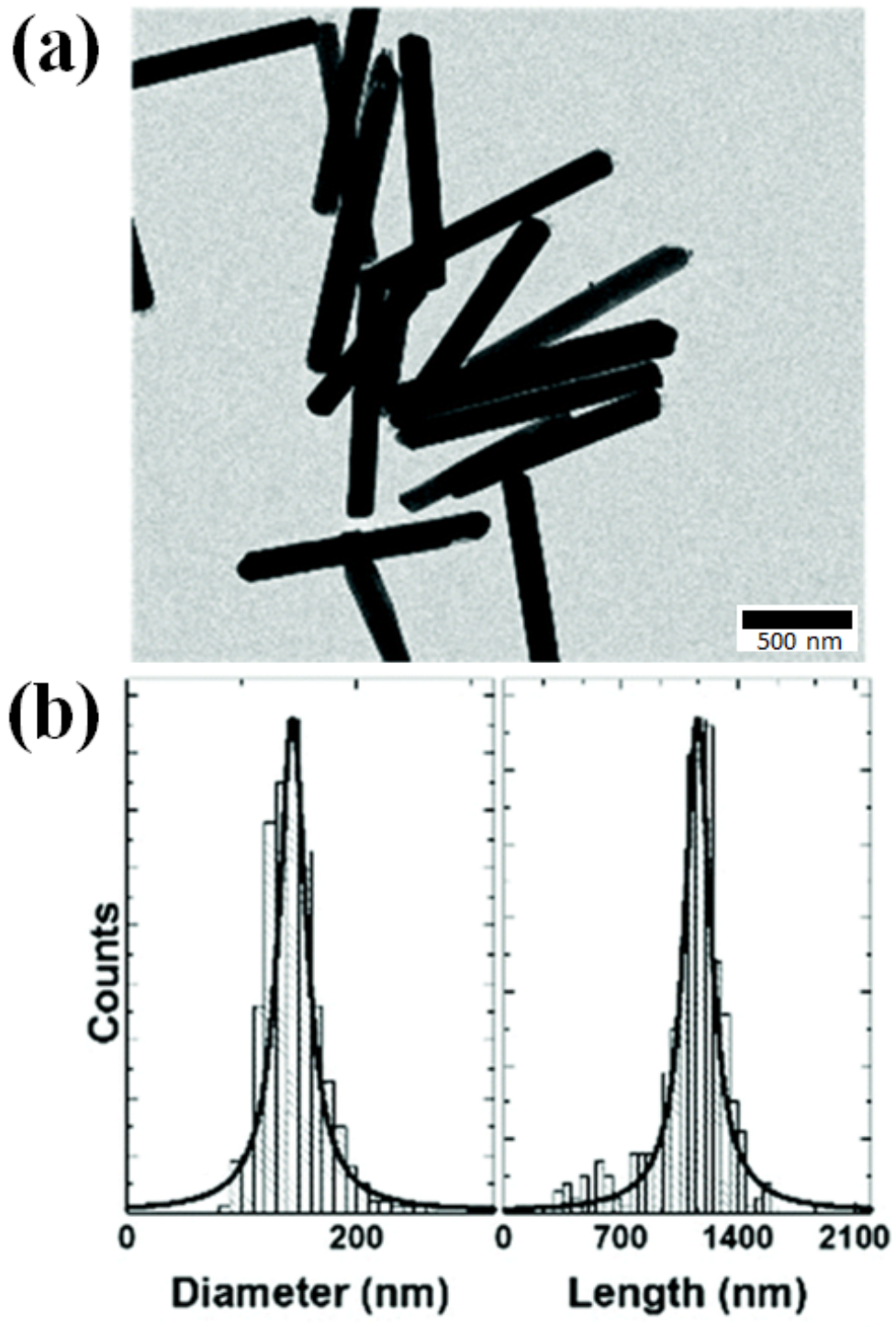
Figure 5.1: NaYF4:Er^{3+},Yb3$^+$ nanorods. (a) SEM showing the asymmetric shape of the particles, (b) histograms showing the size distribution of our nanorod sample [93].
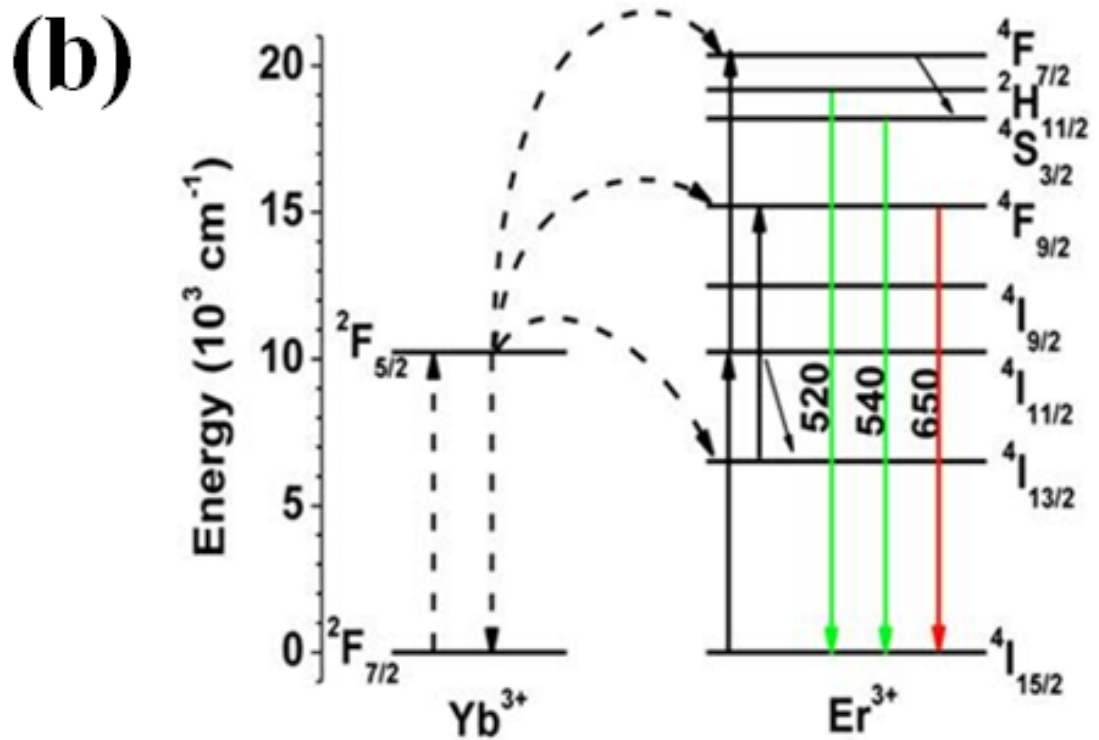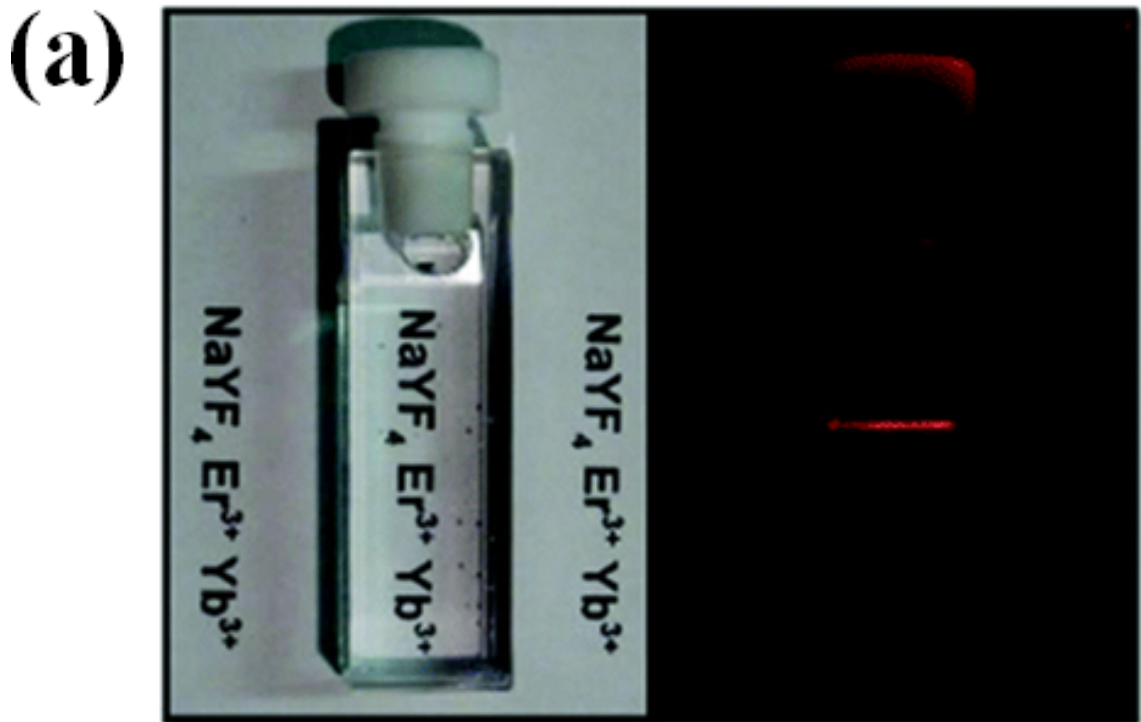
Figure 5.2: NaYF4:Er3+,Yb3+ nanorods. (a) fluorescence emission of the nanorods when illuminated by a laser and (b) the excitation and emission wavelengths which are available from the Yb3+ and Er3+ ions [93].

The NaYF$_4$:2%Er^{3+},18%Yb^{3+} nanorods were synthesised through a published protocol [94]. First a lanthanide nitrate precursor salt (1.2 mM) was prepared by hydrothermal processing using microwave radiation. This was mixed with 14 mL deionised water, 0.7 g, (17.5 mM) of NaOH, 7.1 g, (22.6 mM) of oleic acid (90 wt%), 10.0 g (21.7 mM) of ethanol and 0.3 g (7.2 mM) of NaF. This was stirred at room temperature for 30 minutes then placed in a microwave reactor for 8.5 hours hydrothermal processing at 250 °C at an average pressure under 25 atm, resulting in nanorod formation. These were collected through centrifuging the sample at 12,000 rpm for 15 minutes, the supernatant was removed and the particles washed with ethanol.

5.2   Tweezer Setup and Pump Sources

For manipulating nanorods we made use of two trapping setups, the theory of optical trapping is discussed in *Section 2.7*. Initially we made use of a single beam optical trap consisting of a 980 nm fibre coupled diode laser focused through a 100x 1.25 NA objective. This was sufficient to trap the nanorods but not to control them in 3D. For this we used a modified optical trap with two trapping spots. The modified design is shown in *Figure 5.3*. Our 980 nm laser did not have sufficient power to form two optical traps so a second laser was added, a 1064 nm Nd:YAG solid state laser, Ventus Laser Quantum Photonic Solutions.

To combine the lasers, first the 980 nm light was collimated with an objective, and the 1064 nm beam expanded using two lenses in order to match its beam diameter to that of the 980 nm beam. The 980 nm and 1064 nm beams were combined using a 50/50 beamsplitter, resulting in a 50% power loss for each beam. A second beamsplitter was then used to split the combined beam as shown in *Figure 5.3*. In this configuration only the 980 nm light excites fluorescence in the sample while both the 980 nm and 1064 nm light contribute to the trapping force. Reflecting the beams off two silver mirrors recombines the beams with the overlap controlled by the mirror angle. Thus when focused through an objective two traps will be formed with their relative separation controlled by tilting the mirrors. While this setup allows for the controlled positioning of two traps, and thus a nanorod, it only does so in one axis. To enable true 3D control we would require the addition of focusing optics to move the trap position perpendicular to the imaging plane of the objective.
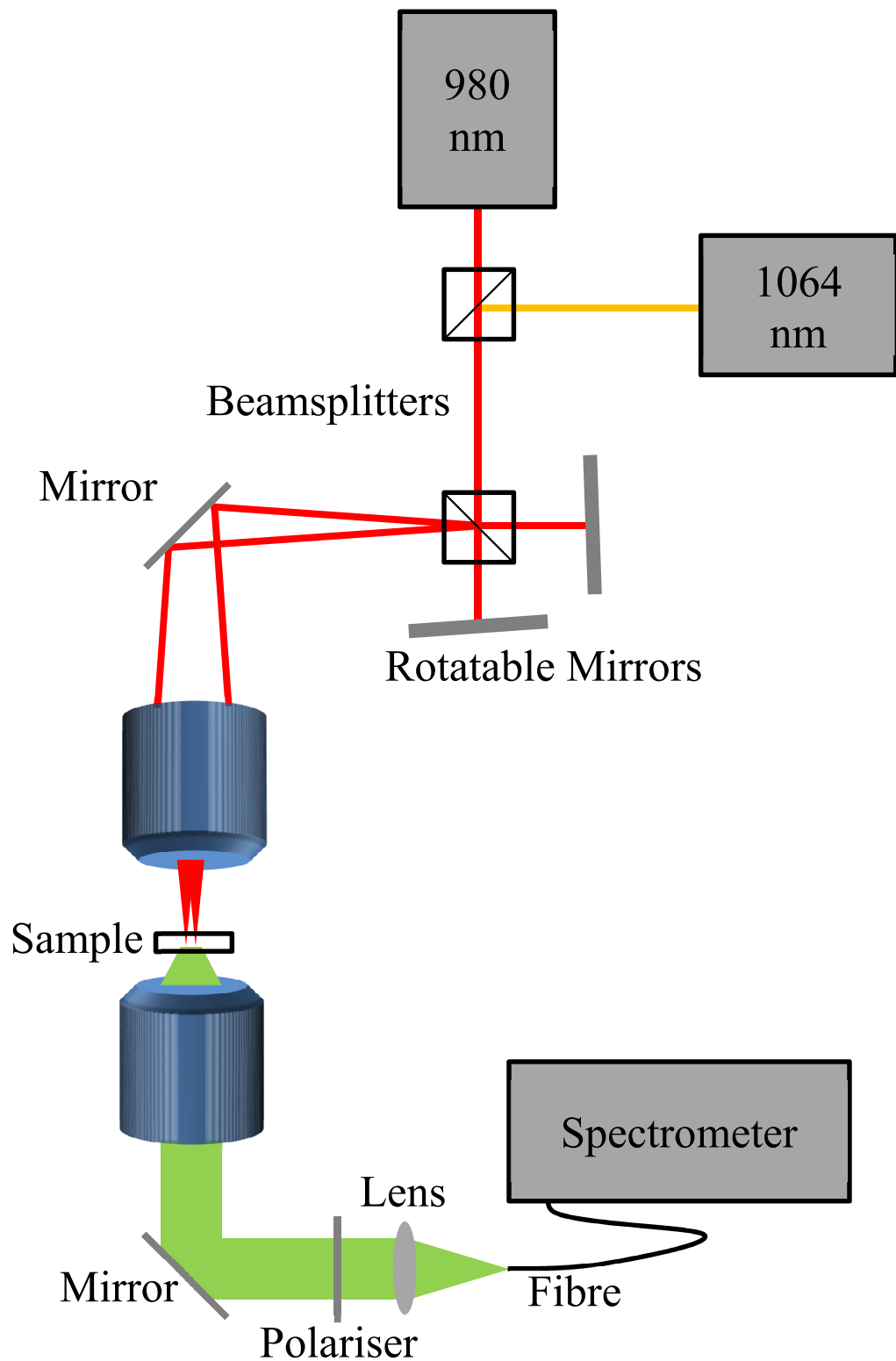
Figure 5.3: Dual beam optical trap with control over the position of each beam. The emission is detected using a polariser and spectrometer.

The laser beams were focused into the sample through a 100x 1.25 NA oil immersion objective and the fluorescence viewed using a second objective below the sample.

Analysis of the emitted light was performed using a linear polariser, Thorlabs LPNIR050-MP2, and spectrometer, HR2000, Ocean Optics. Not shown in the diagram are the camera, Thorlabs DCC1545M, and LED light source used for initial sample positioning

Samples were placed in a microchannel of height 100 μm, Ibidi μ-Slide I 80106 and positioned on an xyz stage. The nanorods were diluted from their stock concentration to $\sim5\times10^9$ NRs per cm^3 so that on average it took several minutes for a particle to enter the trap after the laser was switched on. This ensured that we could distinguish individual trapping events and that when using the dual beam trap a second nanorod was unlikely to enter the trap and disrupt out measurements over short timescales.

5.3   Experimental Results

In order to investigate the trapping of nanorods and determine their emission we must be able to detect single nanorods. This might prove difficult with some fluorescent dyes or proteins which can be faint or photobleach but the $NaYF_4:2\%Er^{3+},18\%Yb^{3+}$ nanorods give a very strong emission even from single particles. This in itself demonstrates why they are such good candidates for fluorescence imaging. To determine if we could detect individual nanorods we used a single beam optical trap with a power of 60 mW. Focusing this into the microchannel containing our nanorods and monitoring the emission we observed increases in fluorescence as shown in *Figure 5.4 (b)*. The step increase in fluorescence visible on both the camera and spectrometer demonstrates we can identify individual trapping events and determine the number of particles in our trap, enabling us to perform experiments on individual particles.
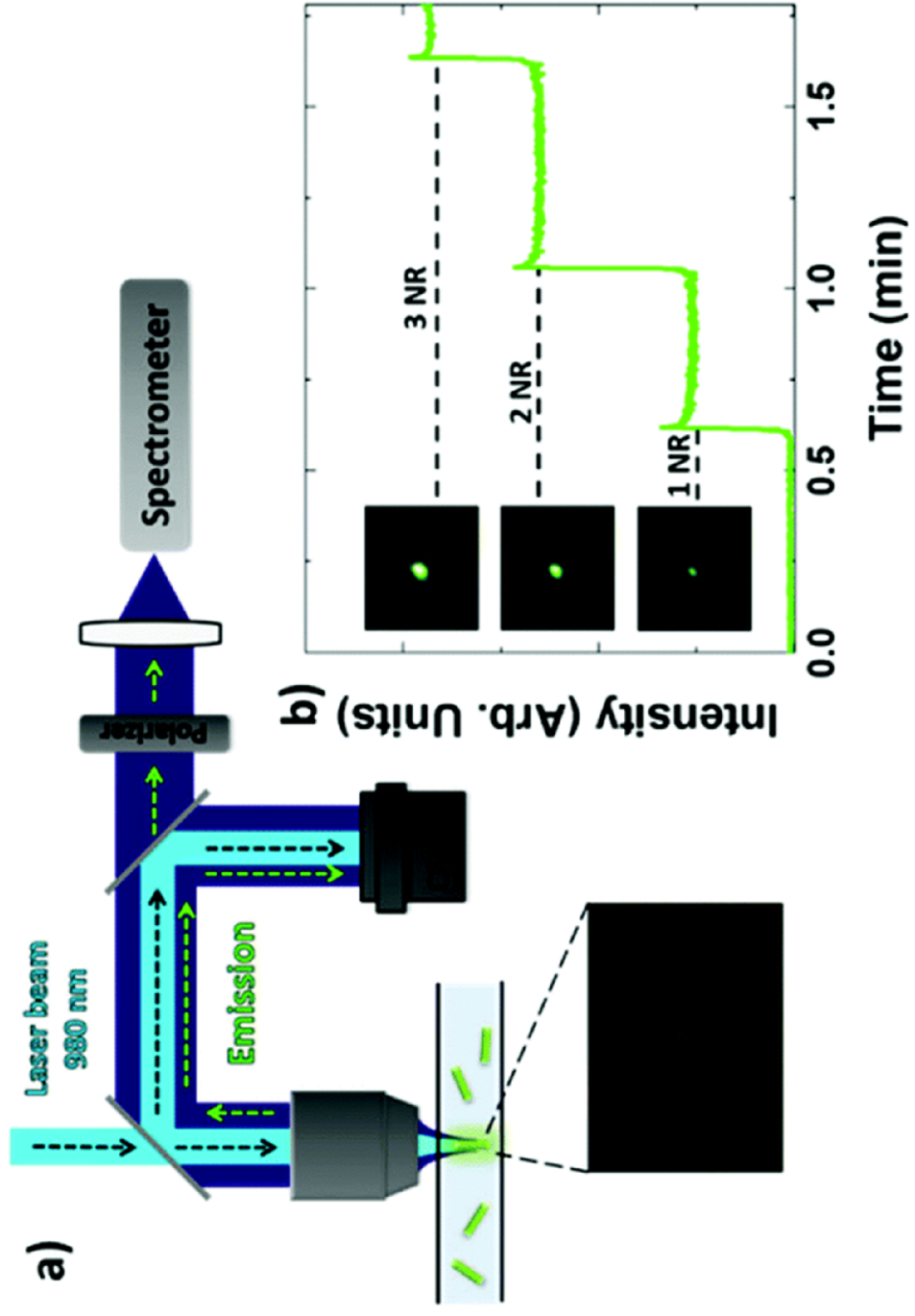
Figure 5.4: (a) single beam optical trap setup. (b) emission of particles in the trap showing that we can identify the trapping of single and multiple particles.

While the single beam optical trap allowed us to trap nanorods we were not able to observe changes in their fluorescence spectrum when sampling their emission with a polariser. The reason for this is that when the nanorods enter the trap they orientate so that their long axis is parallel to the optical axis so when viewed through the objective lens they look like a point and are symmetric around the optical axis. The emission from a nanorod in a single optical trap is shown in *Figure 5.5 (b)*.

To orientate the nanorods with their long axis perpendicular to the optical axis we used a dual beam optical trapping setup, as described above. Using this setup, we first waited for a nanorod to diffuse into one of our two traps. We then moved the second trap inwards until we observed a change in emission indicating that the particle had rotated and was now in both traps. This process is shown in *Figure 5.5*, which shows both experimental data and pictorial representation of what is happening to the nanorod. The change in the camera image is slight, but observations made using a spectrometer show a clear change in in the emission spectrum. This simple method of determining nanorod orientation is straightforward and inexpensive to implement allowing for it to be incorporated into further experiments. This, combined with the ability to control the nanorod using a dual beam optical trap allows for the controllable positioning and rotating of nanorods.

The emission seen in *Figure 5.5 (d)* is for when the polariser is aligned with the nanorod. The emission seen as the polariser or nanorod is rotated relative to the other is shown in *Figure 5.6*. In this figure we have rotated the nanorod perpendicular to the beam axis to demonstrate our control of its orientation. We found that for a trapping power of 80 mW per trap we were able to easily manipulate the particle. We are convinced by our results that we are able to control the particles' orientation and to determine it by recording its emission.
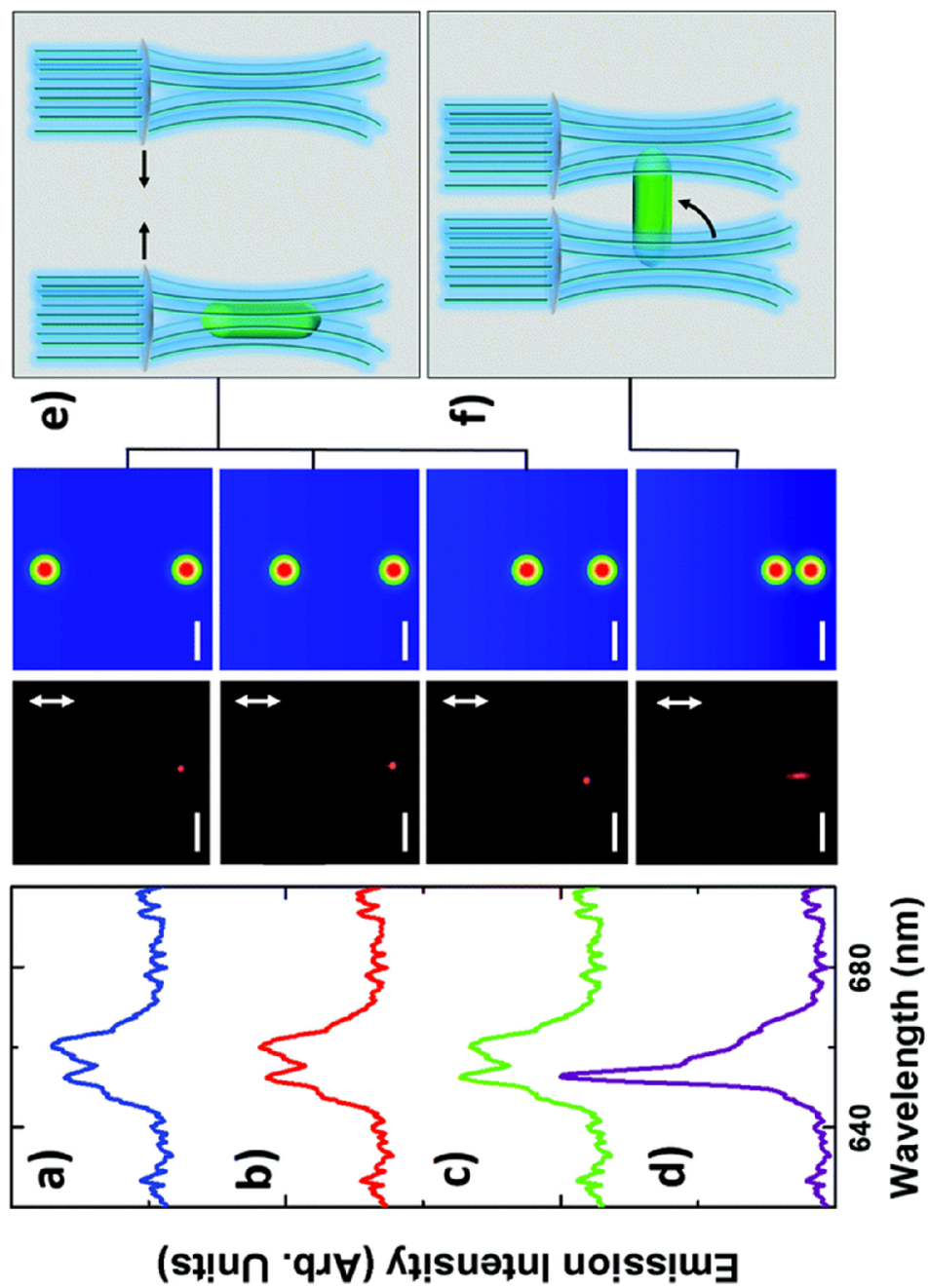
Figure 5.5: Nanorod emission as two optical traps are moved closer together and it rotates relative to the optical axis as observed using a polariser. Scale bar 1 μm. (a-c) nanorod in a single trap as shown in (e). (d) the nanorod in both traps rotating it as shown in (f).
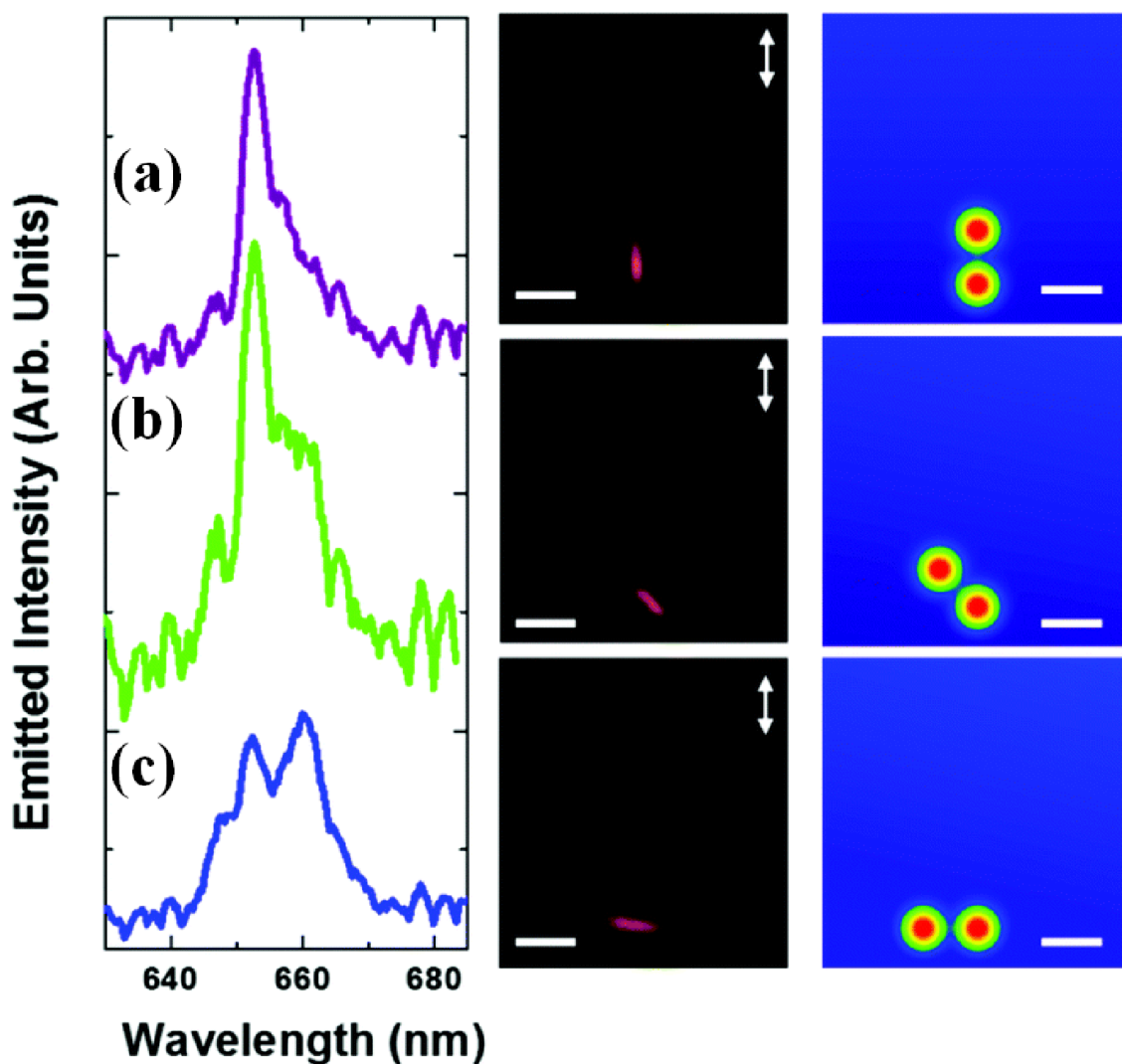
Figure 5.6: Nanorod emission as observed through a polariser as the particle is rotated. Scale bar 1 μm. (a) nanorod parallel to the linear polariser, (b) nanorod at 45 degrees to polariser and (c) nanorod perpendicular to polariser.

5.4 Conclusion

In much of the work we have undertaken in this thesis we have made use of fluorescent dyes and proteins. In doing so we have found that despite being excellent sources for performing a variety of studies in microfluidics they have drawbacks such as photobleaching, damage from UV excitation and broad emission spectra. The alternative, Qdots, is suitable in some cases but can prove toxic to cells.

In collaboration with others we were able to investigate the potential of $NaYF_4:Er^{3+},Yb^{3+}$ upconverting nanorods which do not suffer from these issues. Using a single beam optical trap, we were able to observe single trapping events over a long period of time thanks to

their bright emission and low photobleaching. Using a dual beam optical trap, we were able to rotate the nanorods in 3D and determine their orientation through their polarised emission. This is an improvement on other techniques of determining nanorod orientation as it is simply implemented using a polariser and spectrometer. This control of the particles and the ease with which their orientation can be determined convinces us that they will have applications in both fluorescence experiments and potentially in manufacturing.

6. Biological Laser

6.1 Introduction: Sensing Using Living Lasers

The first laser in 1960 made use of a ruby crystal and since this first demonstration the laser has taken many forms with each new type of laser leading to new applications. For example, the invention of the fibre laser led to a revolution in telecoms, the diode laser is used in projectors and gas lasers in manufacturing. Using a biological cell containing a gain medium to form a 'living' laser is a novel design first demonstrated by Gather and Yun in 2011 using HEK293 cells containing the florescent protein eGFP [26]. They demonstrated that a laser cavity made from such an unconventional object was possible and that the cell was unharmed by the lasing process. Different cells produced different transverse modes indicating that it may be possible to gain structural or even functional information about the cells through the lasing process. This initial demonstration made use of a plane-plane laser cavity, further investigations have demonstrated the use of microspheres inserted into cells [95, 96] or cells within liquid droplets forming whispering gallery mode resonators [97]. Living lasers and the nature of the fluorophores themselves are discussed in more detail in *Sections 1.1.4* and *2.6*.

We have investigated the fabrication and potential applications of living lasers. We formed a laser cavity containing HEK293 cells expressing the fluorescent protein eGFP, that was used as the gain medium, and used a femtosecond laser as the pump source. As the fluorescence lifetime of eGFP, along with most fluorescent dyes and proteins, is on the order of nanoseconds [41, 42] we used a shorter excitation pulse in order to create a large population inversion in the protein pre lasing. This has previously been shown to be successful for a 1D random laser containing the fluorescent protein DsRed [43].

From our initial experiments we achieved lasing but eGFP was not an ideal gain media due to rapid photobleaching, limiting the time lasing could be maintained. Switching to the fluorescent dye Calcein AM we found it photobleached more slowly, allowing us to form and characterise a laser. Our lasing threshold was 300 pJ lower than the previously reported values of 850 pJ [26] though it is impossible to make a direct comparison between cavity designs and fluorophores.

Traditional laser systems can be maintained for long periods of time, decades in the case of the humble HeNe laser. This is not the case in our laser, where we observed emission intensity decreasing rapidly over time with the longest recorded continuous emission

being 60s, at 1 kHz repetition rate, for HEK293 cells containing Calcein AM. This is an expected problem which hinders all fluorescence experiments and is caused by the dye photobleaching. To confirm that this was the case and not alternatively due to cell damage from the high peak intensities of our femtosecond pump source, we used a viability indicator, propidium iodide. This indicated that our cells were unharmed by the lasing process and that the reduction in emission is indeed due to photobleaching, where the fluorophore creates ROS damaging itself and the surrounding cell. Having identified the issue, we considered ways of improving laser lifetime. Vitamin C is an antioxidant capable of neutralising ROS. Adding this to cells we observed an improvement in lifetime, with the longest recorded emission lifetime being 140s; a significant increase. The fact that cells are not harmed by the lasing process, as indicated by our use of propidium iodide, is important if we are to use such lasers for gaining insight into cell behaviour. If the cells were damaged by the process, then clearly the results would be of significantly less or no use in understanding the behaviour of intact healthy cells.

Having achieved lasing and increased the lifetime of our laser we next considered potential applications. A common issue in fluorescence experiments is poor signal to noise ratio where very small changes in emission are being monitored. Lasers are easier to detect than fluorescence having their emission concentrated into a smaller physical area and wavelength range. From our investigation we see this is indeed the case with lasing cells having a 30 times higher peak emission compared to fluorescing cells, when viewed on a spectrometer.

Calcium levels inside cells are of interest as calcium ions are used in cell signalling. To monitor calcium levels, the fluorescent dye Fluo3 is used. Fluo3 increases in emission intensity as the level of calcium increases. We attempted to use HEK293 cells containing Fluo3 to investigate the effect lasing had on the detection of calcium level changes inside cells. Calcium levels were deliberately altered using caged calcium which is released upon exposure to UV light. While we were able to observe changes in fluorescence with calcium levels we were not able to achieve lasing from cells containing this dye. This is most likely due to its lower emission compared to Calcein AM and eGFP. From this we conclude that while it is possible to create cell lasers it may be more difficult to translate this into practical applications and that for such applications fluorophores must be found which meet the requirements of the experiments while also being good gain media.

6.2 Experimental Setup

In order to demonstrate lasing from cells we must consider how the cell's size impacts our choice of cavity. Traditional bulk laser systems have a variety of cavity configurations some of which are not suitable because of the size of our cell, being ~ 15 μm in diameter. While we may wish to use, for example, a bi-concave cavity design it would not be simple to place the cell at the focus of the mirror. Initial attempts to fabricate a cell laser made use of a plano-concave cavity with the cells resting on the plane mirror. It was found that aligning the cavity so that fluorescence was refocused onto the cell was difficult to achieve and we did not observe any lasing behaviour from them. Instead the final successful design we made use of consisted of a plane-plane cavity. This is in theory one of the most unstable cavity designs available, *Equation 6.1*. Setting the radius of curvature of the mirrors $R_1 = R_2 = \infty$ and the length to an arbitrary number gives a value of 1. Any slight misalignment of the plane-plane cavity will cause our resonating laser beam to 'walk' out of the cavity over time.

$$0 \leq \left(1 - \frac{L}{R_1}\right)\left(1 - \frac{L}{R_2}\right) \leq 1 \qquad \qquad \text{Equation 6.1}$$

While this is an issue it is not necessarily as significant as it at first appears. First, it has been shown that cells in such a cavity can act as focusing elements, increasing stability and giving rise to transverse modes [26, 98]. Second, by shortening the cavity length to the diameter of the cell we reduce the effect of this walk off increasing the number of bounces required before the resonating light no longer hits the gain media.

The laser cavity was formed by two plane dielectric mirrors, Layertec, with peak reflectivity of >99.9% at 532 nm. These were positioned with their surfaces horizontal to the lab bench to act as a holder for our cells, which contain the gain media. The cells are placed on the lower of the two mirrors and the second mirror is lowered on top. To prevent any cell crushing, the cells were mixed with microsphere 'pillars', to both hold the mirrors apart and define the cavity length. A custom mount is used to hold the mirrors, with screws to press on the mirrors thus controlling alignment. The whole cavity is translated on an xyz mount in a microscope setup shown in *Figure 6.1*. Pump light is focused into the cavity through a long working distance aspheric objective, Newport 5720, in order to image through our 6 mm thick cavity mirrors. The emission of the cells is separated from

the pump light by a dichroic mirror then split between a CMOS camera, Thorlabs DCC1645C, and a spectrometer, SpectraPro 500i with PI-MAX gain intensified CCD detector. This setup allows us to image cells in the cavity and detect both their pre-lasing fluorescence and lasing emission.
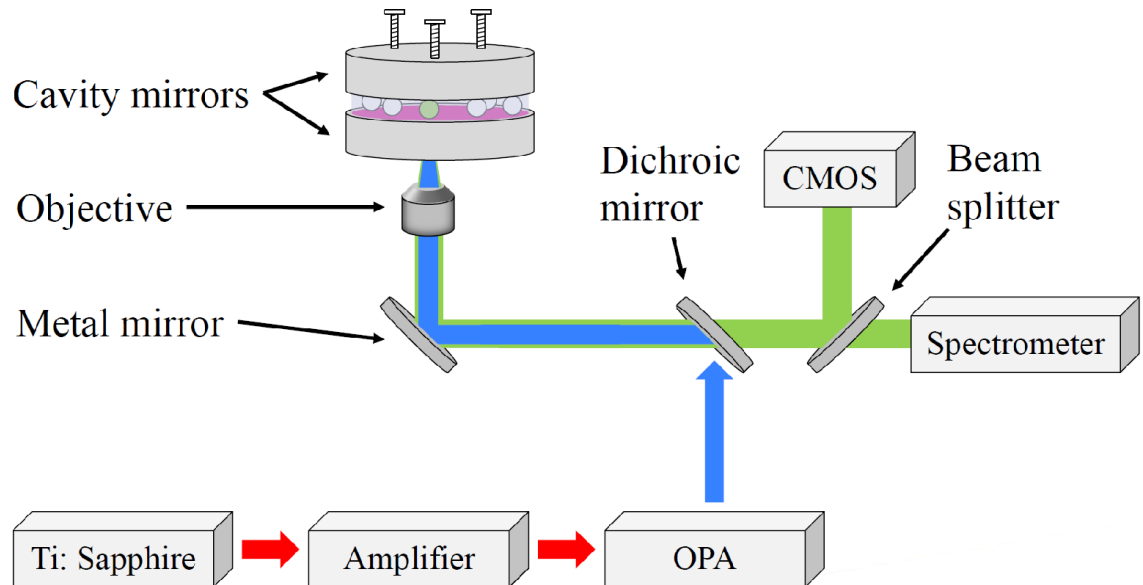
Figure 6.1: Simplified experimental setup where light is generated from an OPA system before being focused onto the laser cavity containing cells containing fluorescent dye.

The alignment of the laser cavity is crucial and as such it was measured by reflecting a HeNe laser off the mirrors as depicted in *Figure 6.2*. The reflections from each mirror interfere with each other, giving an interference pattern as shown, with the number of fringes indicating alignment. The cavity is adjusted so only one fringe can be seen in the interference pattern, meaning the mirrors are aligned to within one wavelength across the cavity; 633 nm. Assuming the entire cavity is 25.4 mm across (the diameter of the mirror), this gives a value of 25 µradians; equivalent to rotating the adjuster on a standard kinematic mirror mount by approximately 1/300th of a revolution. To obtain even greater precision in the measurement we allowed the light reflected from the cavity to travel a large distance until the two reflections separated then calculated the angle between them using trigonometry to give the mirror alignment. While this method did indeed give greater precision it was judged to be impractical, as a distance of around 30 m was required to achieve the same result as the interference pattern method. Improving on this would require this distance to be doubled for every halving in the measured angle.
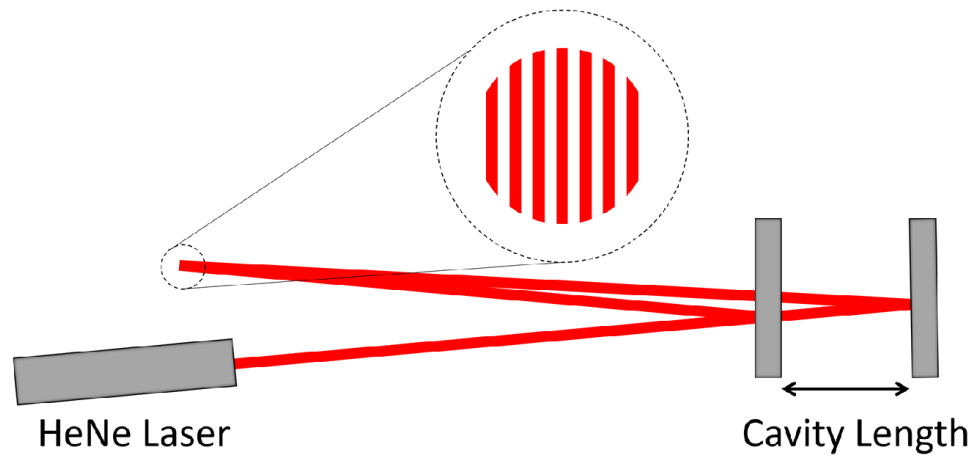
Figure 6.2: Cavity alignment using a HeNe Laser reflected off the cavity to measure the angle between the mirrors.

Our pump laser consists of an OPA system from Spectra Physics. A Tsunami Ti: Sapphire femtosecond laser is amplified by a Spitfire chirped pulse regenerative amplifier. An OPA, 800C, is then used to tune the wavelength to the desired wavelength to maximise the absorption by our fluorophore. To avoid damage inside the crystal of the amplifier, the pulse is stretched before amplification as shown in *Figure 6.3*. The input pulse makes a double pass on a diffraction grating. This first stretches the pulse spatially then recompresses it to a point in space with the effect of stretching it in time. After this stretched pulse has been amplified it makes another double pass on a diffraction grating reversing the process to give an output of ~120 fs 800 nm pulses at 1 kHz with a pulse energy of 1 mJ.

The OPA 800C performs difference frequency mixing in a β-Barium Borate (BBO) crystal to produce a signal and idler pulse as shown in *Figure 6.4*. The input pulse is split into three arms. The first is used to generate a white light supercontinuum. This is overlapped in the BBO crystal with the second pulse to form a seed for amplifications. This seed is overlapped in the BBo crystal on a second pass with the third pulse to give our final signal and idler. For our experiments we used the idler pulse operating at ~1900 nm. This was frequency doubled twice in further BBO crystals to give blue pump light at a tuneable wavelength ~475 nm with the exact wavelength depending on the absorption maximum of our fluorophore.
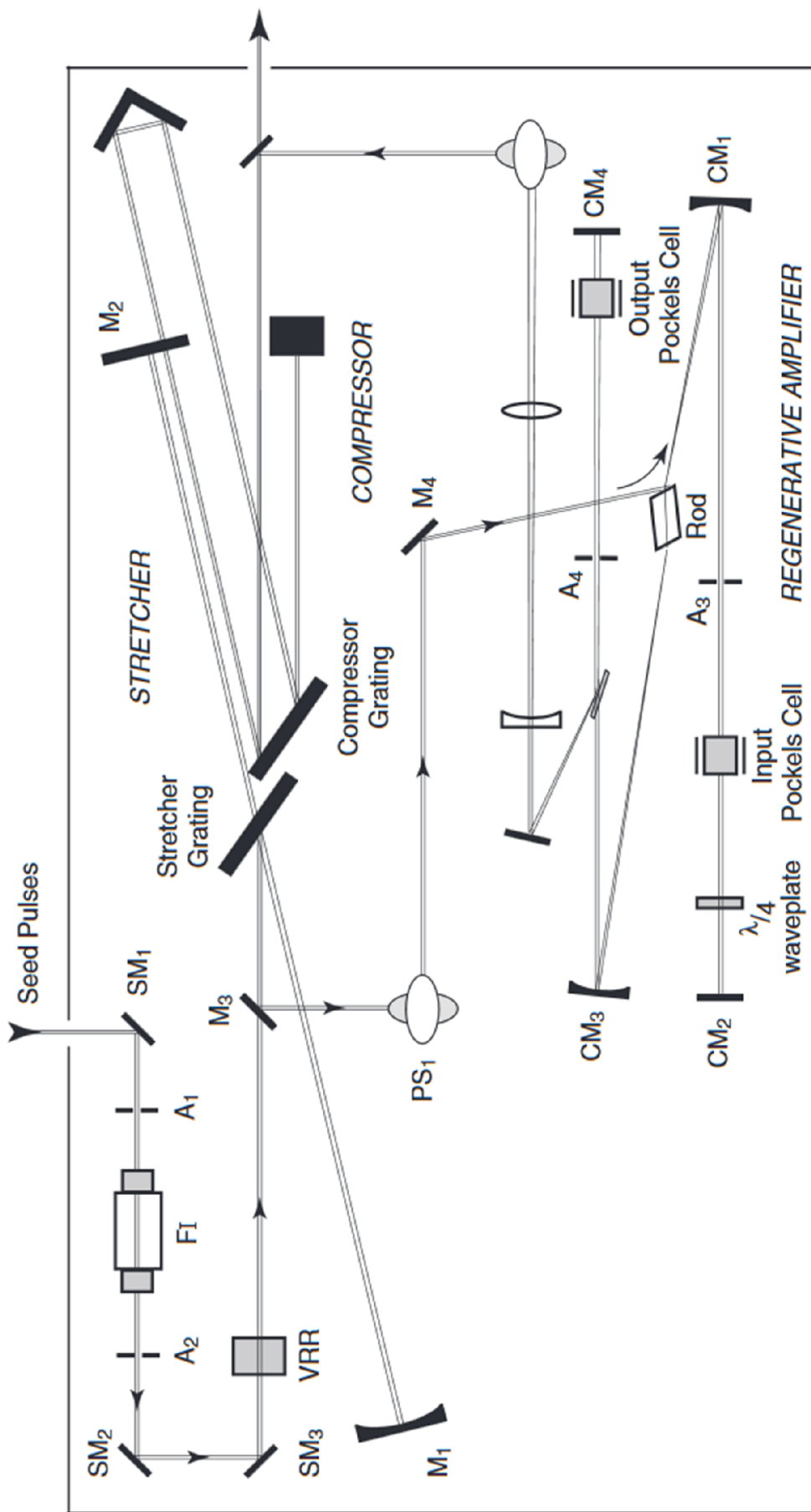
Figure 6.3: Spectra Physics Spitfire amplifier with repetition rate of 1 kHz and 1 mJ pulses at 800 nm.
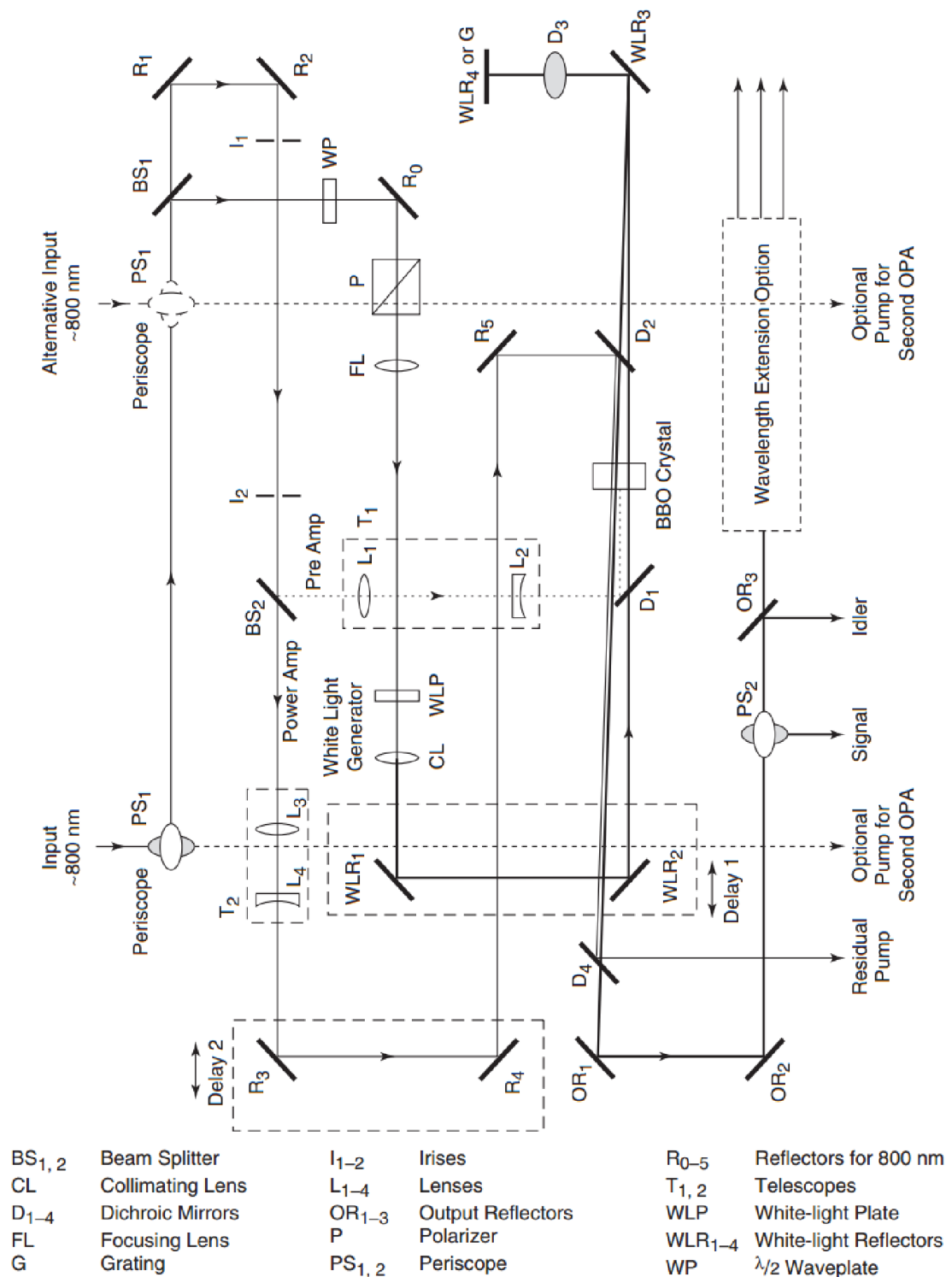
Figure 6.4: OPA 800 frequency conversion. We make use of the Idler output and BBO frequency doubling extension option to obtain visible pump light.

In the following experiments we made use of three fluorophores; eGFP, Calcein AM and Fluo3. The first is a fluorescent protein derived from WT-GFP as set out in *Section 2.6.1*. Calcein AM (Life Technologies, Paisley, UK) is commonly used as a viability marker. It is initially non fluorescent and uncharged allowing it to enter cells but once inside them

the AM group is cleaved by intracellular esterases. This results in a fluorescent, charged form of the dye which exits the cell at a much lower rate than the uncharged form, resulting in accumulation inside the cells and a much lower concentration in the surrounding media. As intracellular esterases are only present inside living cells the dye acts as a viability marker showing us that cells are healthy, at the time the dye is added. Fluo3 is a calcium sensitive fluorescent dye which changes emission intensity, becoming brighter, in the presence of calcium. The absorption (dashed line) and emission (solid line) spectra for each of these fluorophores is shown in *Figure 6.5*. They generally absorb blue pump light and emit in the green.
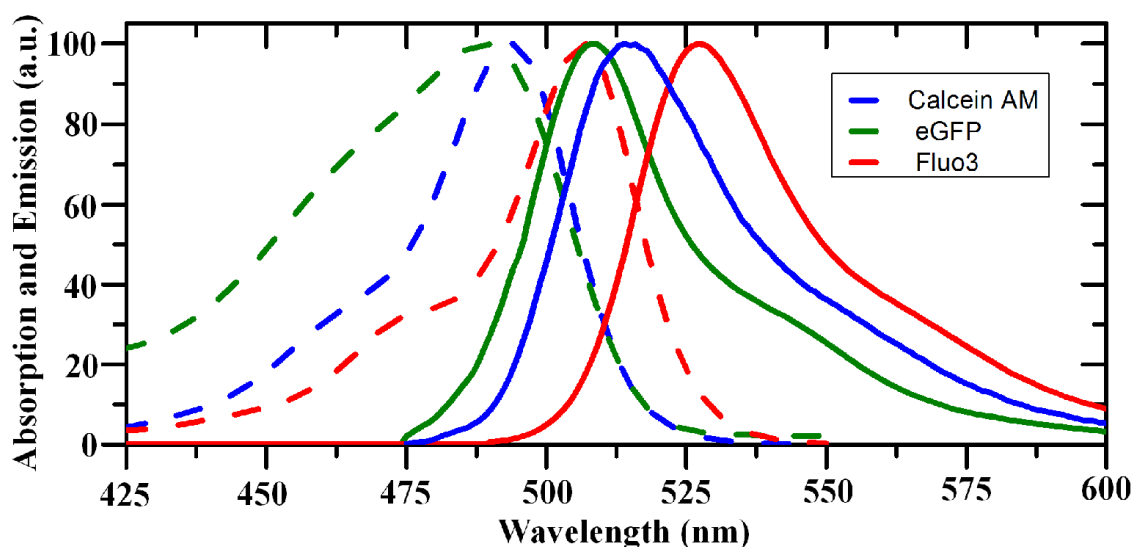
Figure 6.5: Absorption and emission spectra for the fluorescent dyes used in our experiments. Data from ThermoFisher Scientific. Dashed lines are absorption and solid lines are emission.

To prepare cells with our chosen dye we used a variety of protocols initially based on manufacturers recommendations, then customised over time to improve cell brightness and viability. Our final protocols are given below though for any given experiment the exact concentrations and media used varied. For cells containing Fluo3 we also included caged calcium to control calcium levels as explained previously.

HEK293 cells were typically plated, using a 6 well plate, and allowed to grow for between 24-48 hours at 37 °C and 5% CO_2 until optimal confluency was reached. The preparation of each fluorophore then varied:

HEK293 cells containing eGFP:

Prepare 4µg GFP DNA in 250µl media and 10µl lipofectamine in 250 µl media in separate Eppendorf tubes. Leave these for 10 minutes at room temperature then mix together. Leave for an additional 30 minutes. Remove 500 µl medium from the wells and add the 500 µl of DNA/Lipofectamine. Incubate for 48 hours.

HEK293 cells containing Calcein AM:

Solubilise 50 µg Calcein with 25ul DMSO to produce a 2 mM stock. Dilute 10 µL of 2mM Calcein in 2 mL of Versene producing a final concentration of 10 µM. Remove culture media from cells then add 2 mL of 10 µM Calcein per well. Incubate for 30 minutes. Collect cells and centrifuge for 3 minutes at 500 g before re-suspending in 200 µL EBSS.

HEK293 cells containing Fluo3 and caged calcium:

Rinse cells with 5 mL Versene, detach cells using 4 mL trypsin for 1-2 minutes, then add 8 mL DMEM phenol red free Centrifuge for 3 minutes at 500 g then re-suspend in 1 mL of Ringer buffer. Add 5 µM of Fluo3 and 4 µM of Caged Ca^{2+} in DMSO. Incubate for 1 hours. Centrifuge for 3 minutes at 500 g then re-suspend in ringer buffer.

6.3   Experimental Results

6.3.1   Fluorescent Protein Laser

To investigate the fabrication of cell lasers and investigate their applications we performed a series of experiments. To begin we made use of HEK293 cells containing eGFP to see if we could achieve lasing. Cells were prepared according to the protocol given above and placed in our laser cavity. Illuminating these with our pump laser we selected individual cells or groups and observed their emission as the pump energy was increased. We observed a variety of behaviours due to the variation in cell size and the concentration of eGFP contained in each cell. When the mirrors were unaligned we observed simple fluorescence emission like that given in *Figure 6.5*. Improving the alignment of our mirrors we began to observe amplified spontaneous emission as shown in *Figure 6.6*. There the individual emission peaks correspond to the longitudinal modes of the cavity and as such the spacing between them could be seen to change as the cavity length was changed by pressing down on the mirrors.
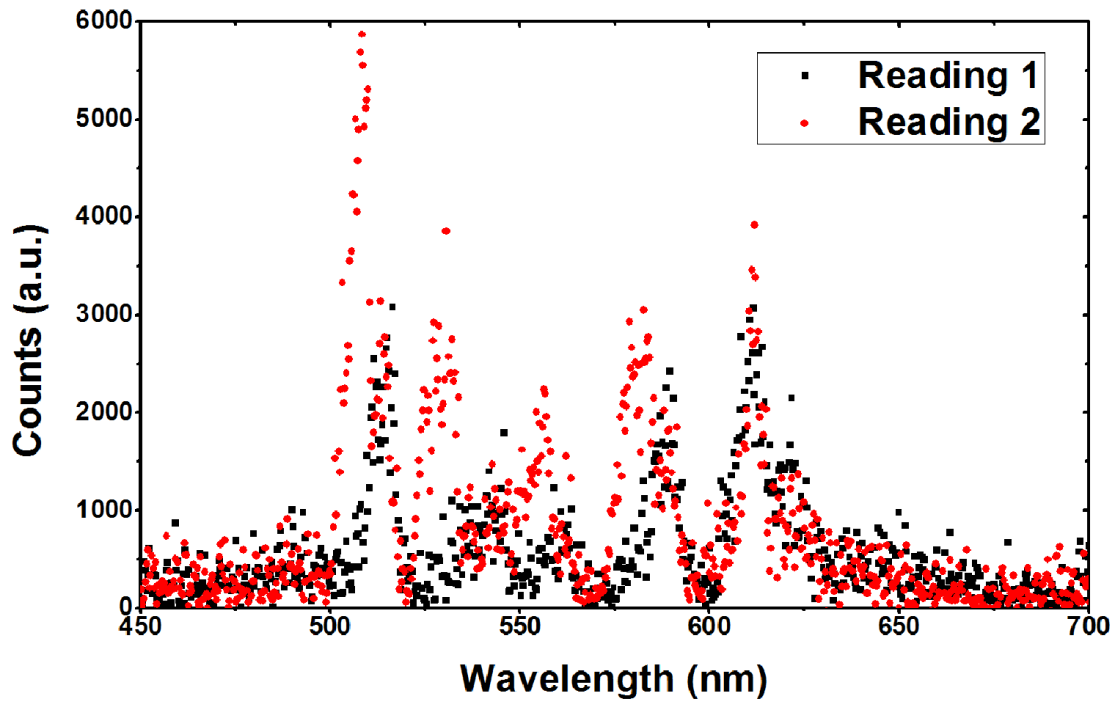
Figure 6.6: Amplified spontaneous emission from eGFP in a laser cavity with pump pulse energy ~ 6 μJ. The peaks of readings 1 and 2 between 500 and 600 nm are displaced relative to each other as cavity spacing changes. The peaks beyond 600 nm are not shifted as they are due to fluorescence outside the reflectivity region of the mirrors.

Due to the broad emission spectrum of the protein we see multiple longitudinal modes as well as emission beyond 600 nm where the reflectivity of the mirrors decreases. The expected mode spacing can be calculated using *Equation 6.2*, where $\Delta\lambda$ is mode spacing, λ wavelength, n refractive index and L cavity length. Using 9 μm microspheres to define cavity length, setting $\lambda = 550$ nm and $n = 1.33$ gives us a spacing between modes of 12.6 nm.

$$\Delta\lambda = \frac{\lambda^2}{2nL} \qquad\qquad \text{Equation 6.2}$$

From our initial experiments looking at fluorescence from within the laser cavity we observe that while the microspheres define the cavity length, it is quite possible to crush them slightly during alignment, reducing the cavity spacing further. The cells themselves have an average size of ~15 μm so for short cavities they will be in contact with the mirrors, and very short cavities result in them rupturing. An alternative arrangement would be to use a longer cavity at which point the stability of the laser relies on cells acting as focusing elements in the cavity.
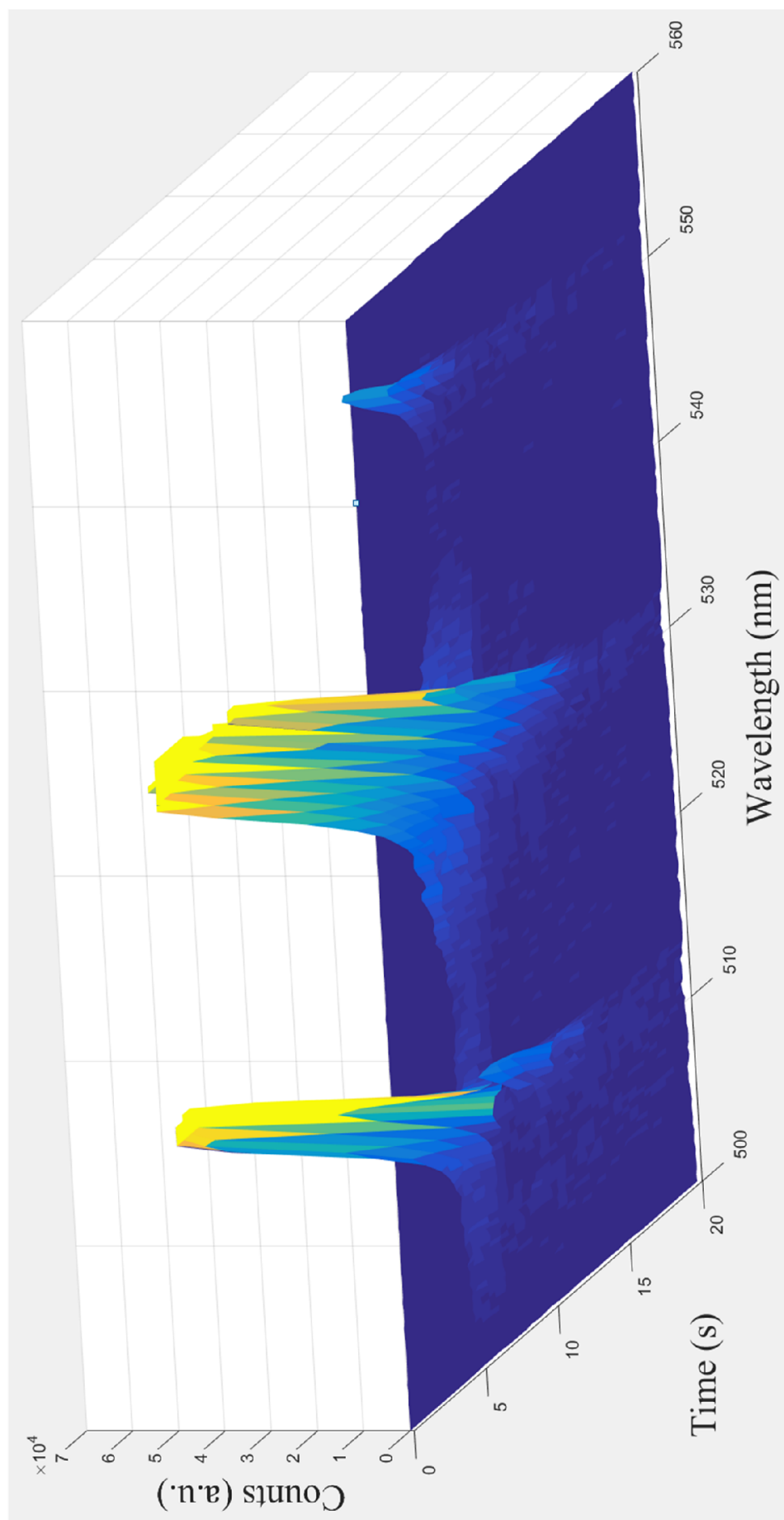
Figure 6.7: The emission of eGFP over time when lasing with a 5 nJ pump pulse energy. Initially three longitudinal modes can be seen before decaying over several seconds.

Searching through a large number of cells we locate some which lase. When this occurs we see a sudden intense emission follower by a rapid decay as shown in *Figure 6.7* where we translate a cell into the location of the pump laser and see three longitudinal modes appear, theses rapidly decay and stop lasing. Cells were manually positioned in the beam so there are some changes in emission as the cell moves relative to the pump. The emission spectrum can be seen in *Figure 6.8* where we see there is one dominant mode and two side modes. From these experiments, looking at a large number of cells, we deduced that transfection efficiency was the major factor with few cells having sufficient eGFP to form a laser. This issue and the rapid photobleaching led us to use a different fluorophore for future experiments.
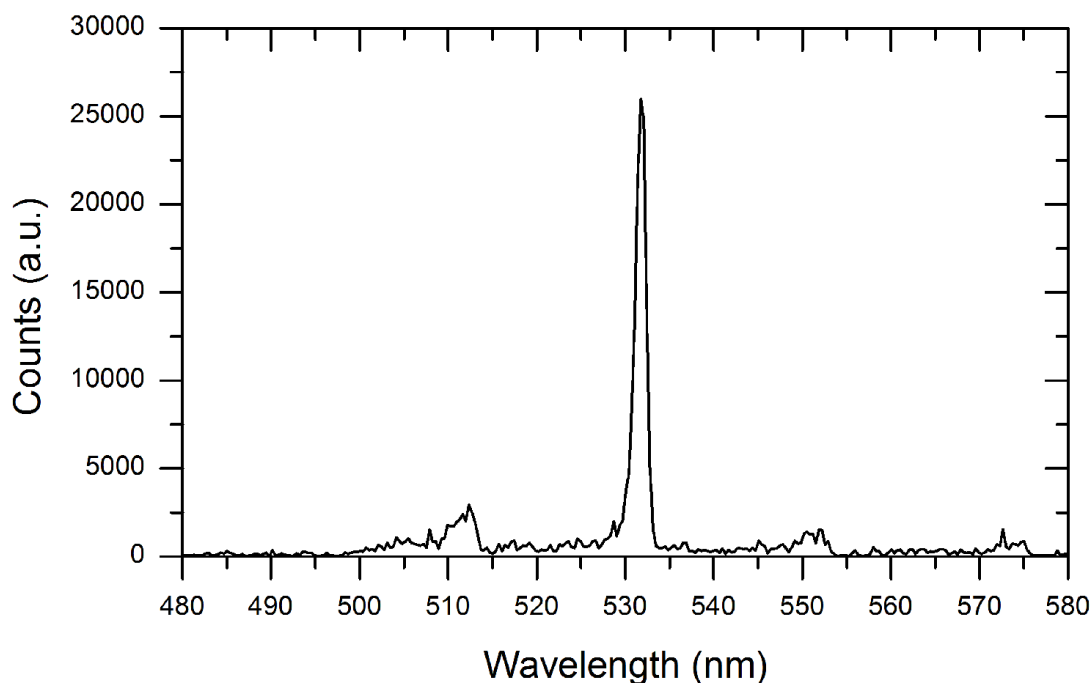
Figure 6.8: Laser spectrum from eGFP at time 12 s from *Figure 6.7*. There are 4 longitudinal modes with the central peak at 532 nm dominating.

6.3.2   Fluorescent Dye Laser

Instead of using eGFP we instead made use of the fluorescent dye Calcein AM as it has similar excitation and emission peaks while being more fluorescent, evenly staining cells and photobleaching more slowly. Using this and performing experiments as before we were able to achieve lasing consistently and for longer periods, though the process still

required locating the cells with the highest concentration of dye. Cell lasing was maintained for up to 60s, at 1 kHz repetition rate before photobleaching prevented further lasing.

The emission of a cell lasing is shown in comparison to fluorescence in *Figure 6.9*. Here we see the 3 longitudinal modes of the laser and that the peak emission is 30 times higher than fluorescence making detection easier for equivalent pump energy. The emission of a cell as pump energy is increased is shown in *Figure 6.10* with a lasing threshold of 300 pJ, lower than previously reported values of 850 pJ [26]. This low lasing threshold is explained by our use of a femtosecond pump source which creates a large population inversion in the dye before lasing occurs.
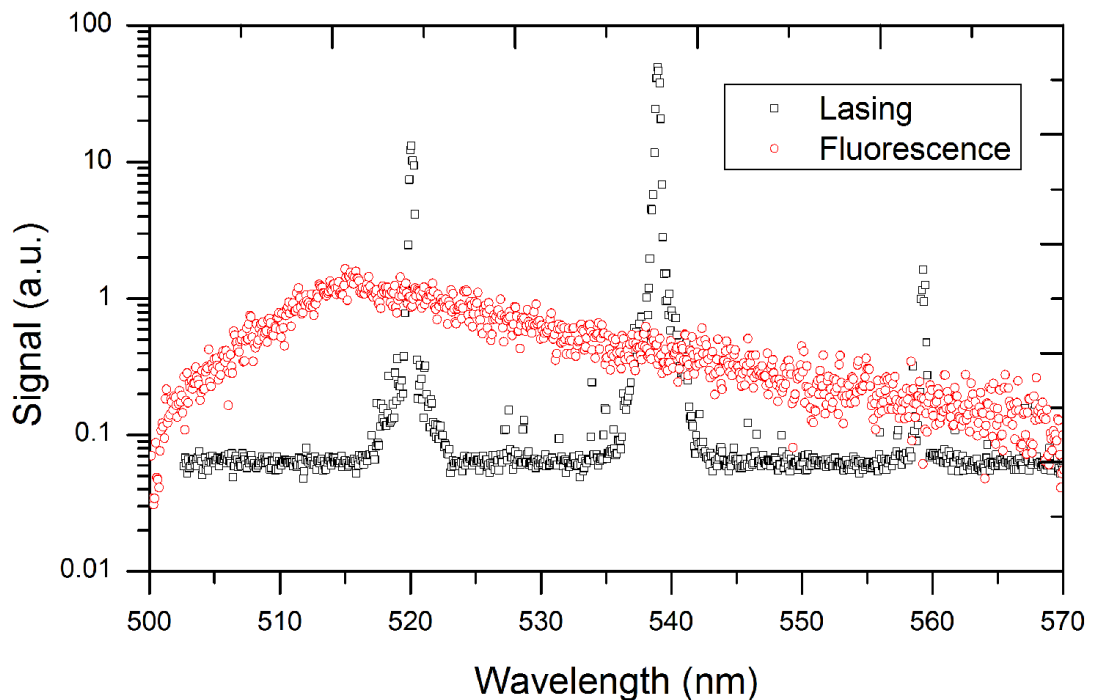
Figure 6.9: Emission spectrum of a single cell emitting on 3 longitudinal modes (black) compared with the fluorescence spectrum from a cell not in a laser cavity (red). Incident pump pulse energies are 1.2 and 1.5 nJ for the lasing and fluorescing cell respectively.
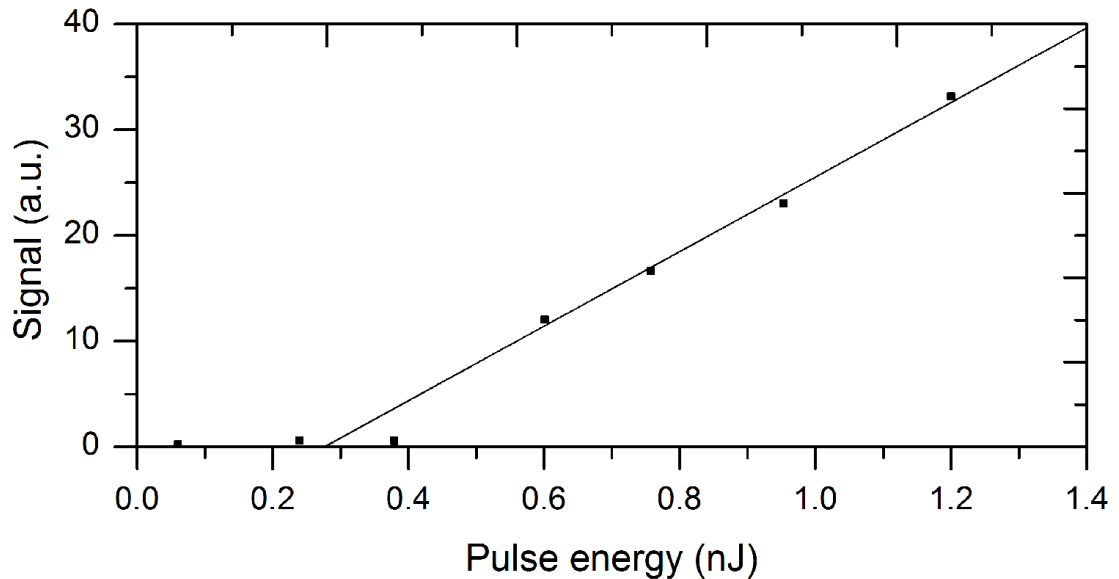
Figure 6.10: Laser emission against pump pulse energy showing a threshold of 300 pJ.

To understand how using a fs pump laser rather than ns, or indeed CW, we constructed a model of the system looking at the energy stored in the upper laser level against time for different input pulses. Increased storage of energy will lead to a lower input pulse energy requirement to obtain a population inversion and thus lasing. For our model we assume a Gaussian input pulse, 100% absorption and a 4 ns fluorescent lifetime. The results of this model are shown in *Figure 6.11* for a 4 ns pump pulse We see that as the laser pulse is absorbed by the sample the stored energy peaks then decays through fluorescence emission. Plotting for a range of input pulse lengths in *Figure 6.12* we see that pulse lengths shorter than the fluorescence lifetime leads to increased energy storage while those longer lead to decreased storage. This will have a correlation with lasing threshold. We conclude that using a pulse at least 10 time shorter than the fluorescence lifetime will lead to the best results with increasingly shorter pulses giving diminishing returns.
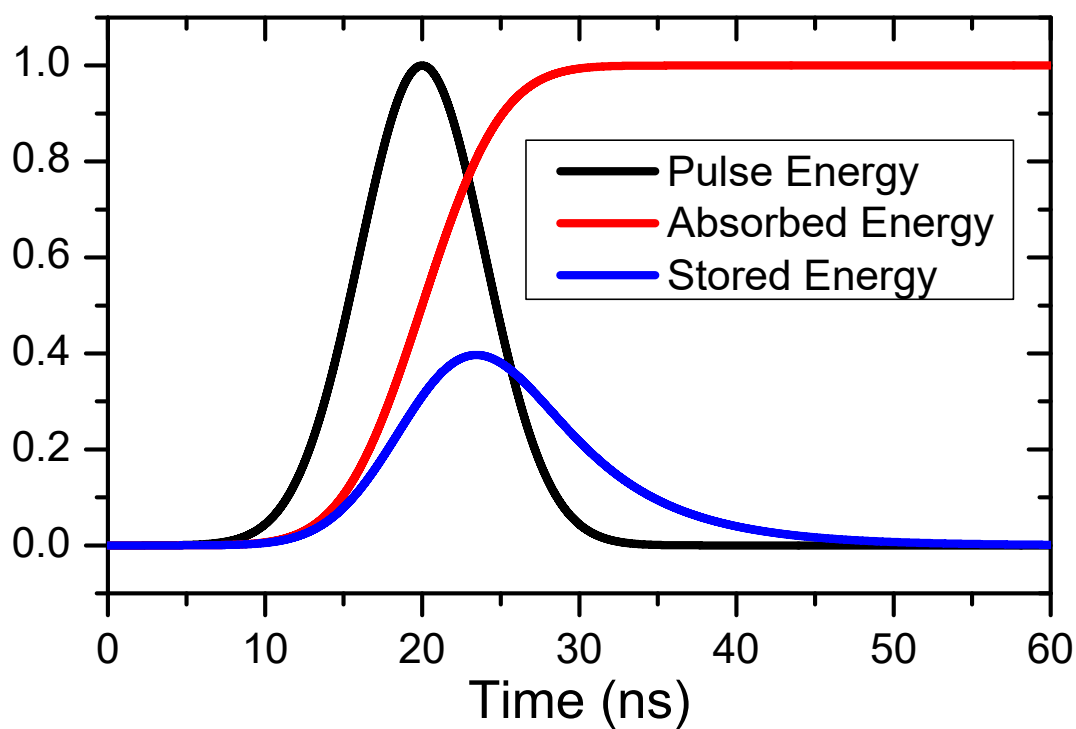
Figure 6.11: Energy stored in the upper state of the fluorescent dye over time. The data shown if for an input pulse length of 4 ns and a fluorescence lifetime of 4 ns.
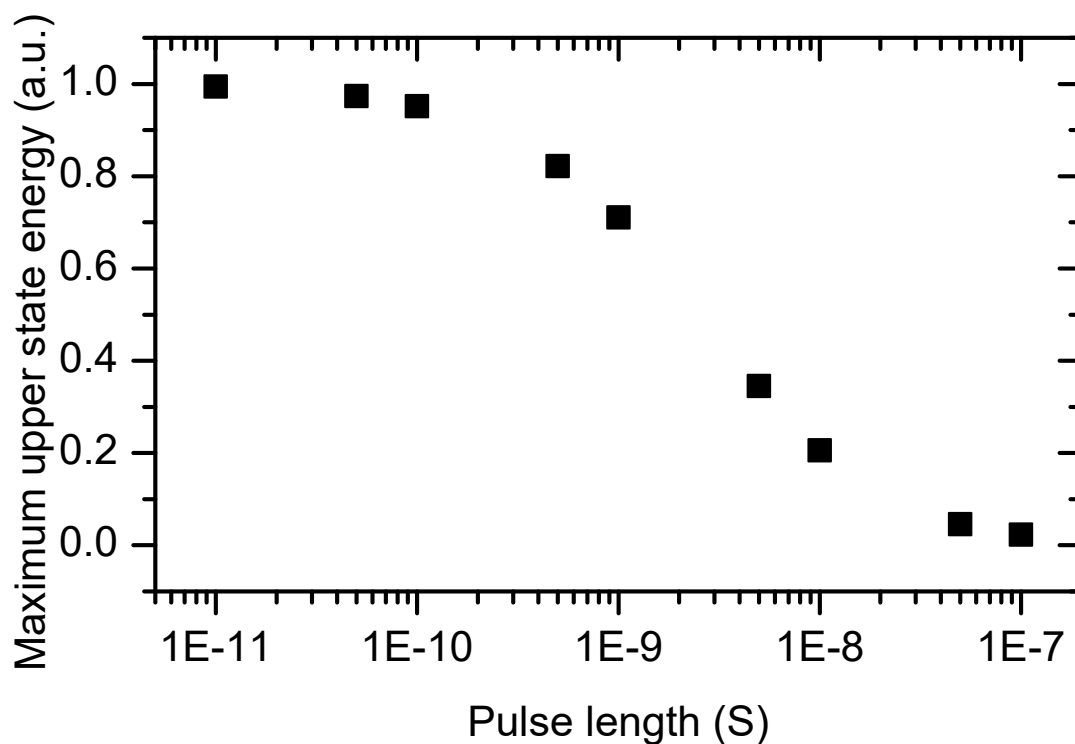
Figure 6.12: Maximum energy stored in the upper state of the fluorescent dye plotted against input pulse length for a 4 ns fluorescence lifetime. Below around 100 ps there are diminishing returns from using a shorter pulse.

Upon imaging of the cells lasing, we observed that they typically only have one transverse mode, as would be expected from the cavity design, though we were able to excite other modes through careful positioning of the pump laser relative to the cell. This would indicate that the cell is acting as a lens in the cavity enabling different beam paths. This behaviour is shown in *Figures 6.13*and *6.14*.
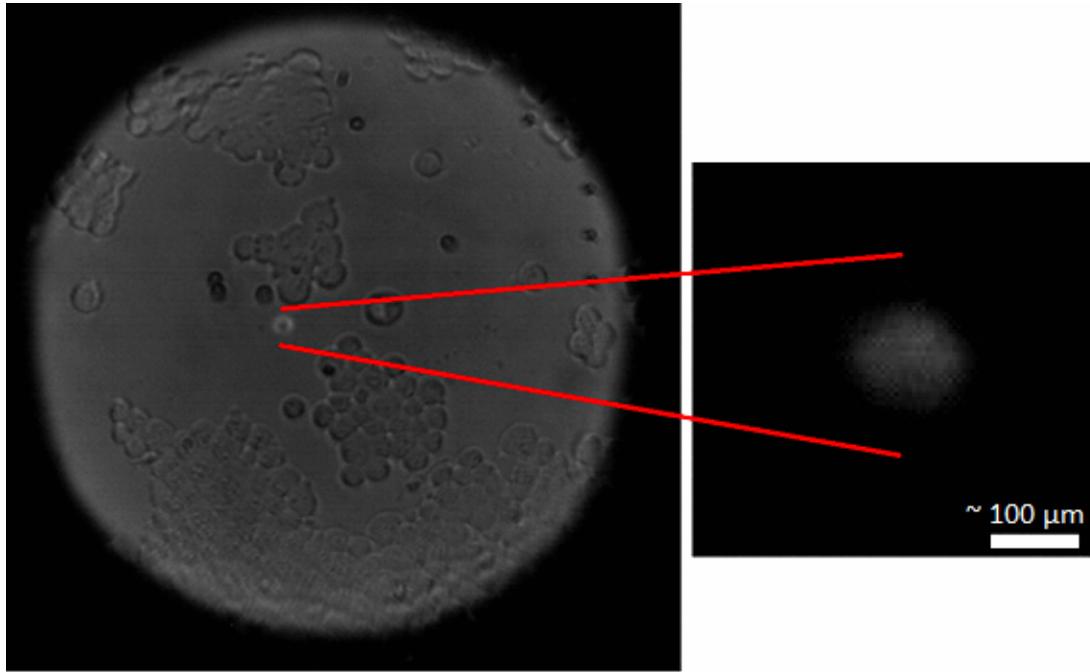
Figure 6.13: Lasing emission from a single cell. Scale bar ~ 10 µm.
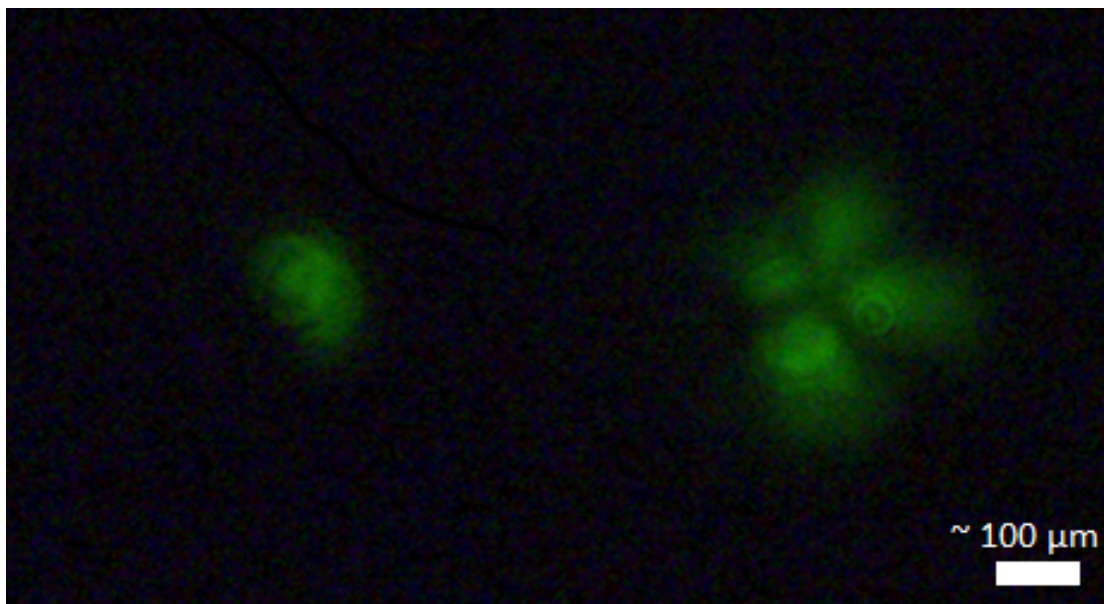
Figure 6.14: Lasing modes from single cells. (a) $LP_{0,1}$ and (b) $LP_{2,1}$. Scale bar ~ 10 µm.

While the emission of our laser lasts up to 60 s it does decrease over time. This could be due to either photobleaching, a common issue when using fluorescent proteins and dyes, or from damage to the cell from the high peak power in our femtosecond pump source. To identify the cause, we used the viability indicator stain propidium iodide. This is a dye which is initially non fluorescent and cannot pass through the intact membrane of live cells. If the cells are dead or damaged however it can enter at which point it binds to DNA inside the cell becoming fluorescent as shown in *Figure 4.13*, where we have added ethanol to cells and thus killed them.
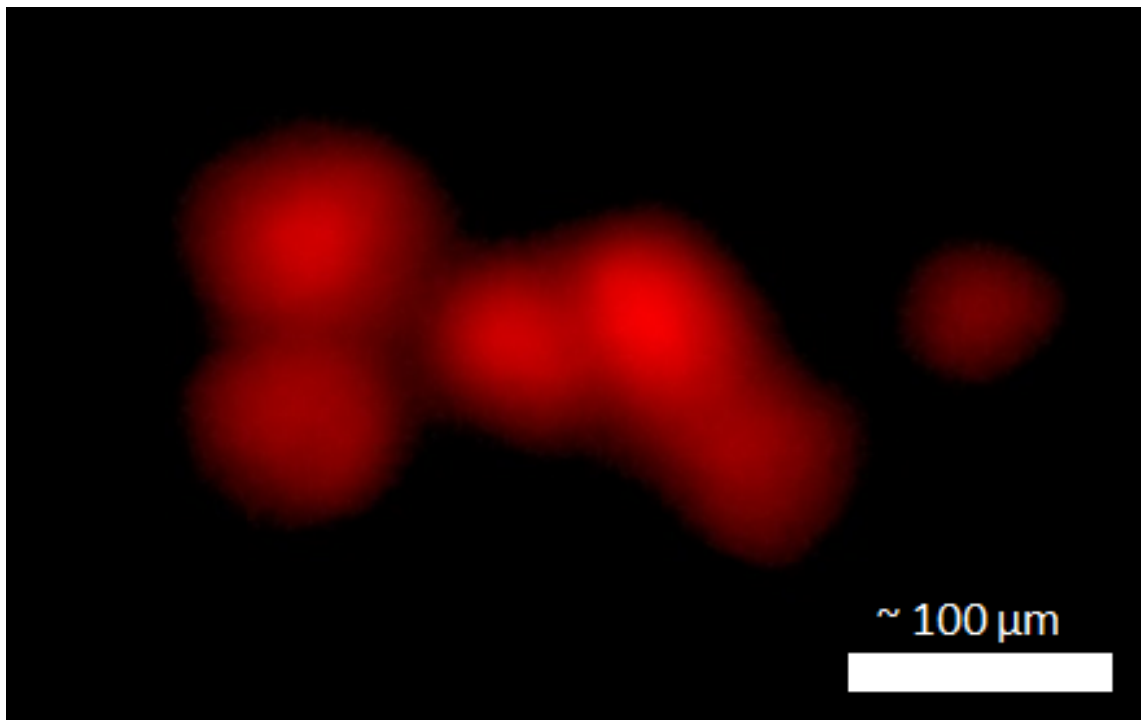
Figure 6.15: Propidium iodide emission from cells exposed to ethanol demonstrating its ability to identify cells with damaged membranes. Scale bar ~ 20 μm.

Cells were prepared containing both Calcein AM and propidium iodide. Using suitable filters, we observed the fluorescence from each before and after exposure to our pump laser. A group of cells is shown in *Figures 6.16* and *6.17*. In *6.16* (a) we see Calcein AM emission at the beginning while in *6.16* (b) we have bleached the central region. In *6.17* (a) we see the propidium iodide emission before exposure and in *6.17* (b) after. There is no notable increase in emission indicating that the cells are unharmed by the exposure to our pump laser and that the decrease in Calcein AM emission is indeed due to photobleaching.
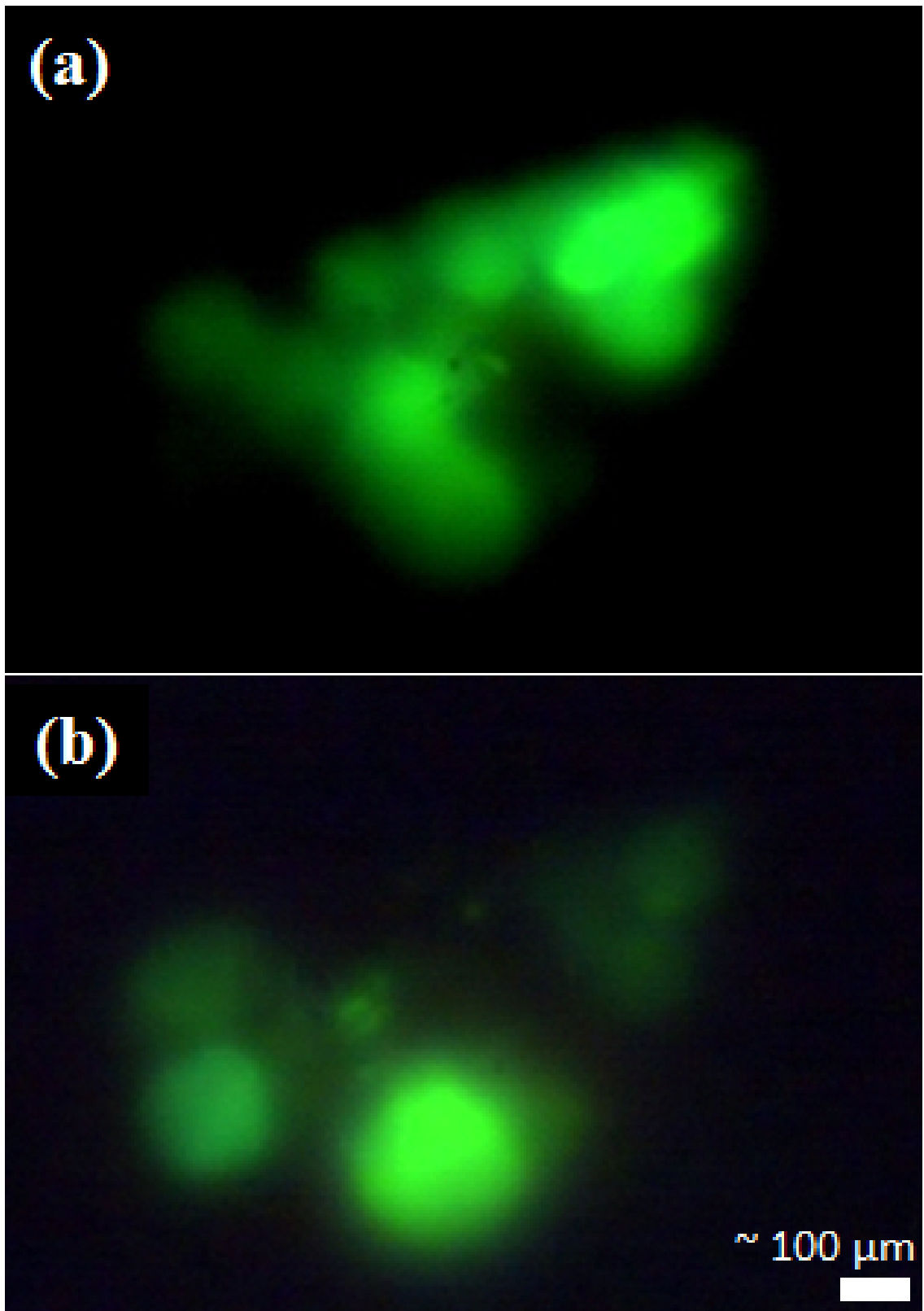
Figure 6.16: Cells containing Calcein AM before and after exposure to femtosecond pumping.
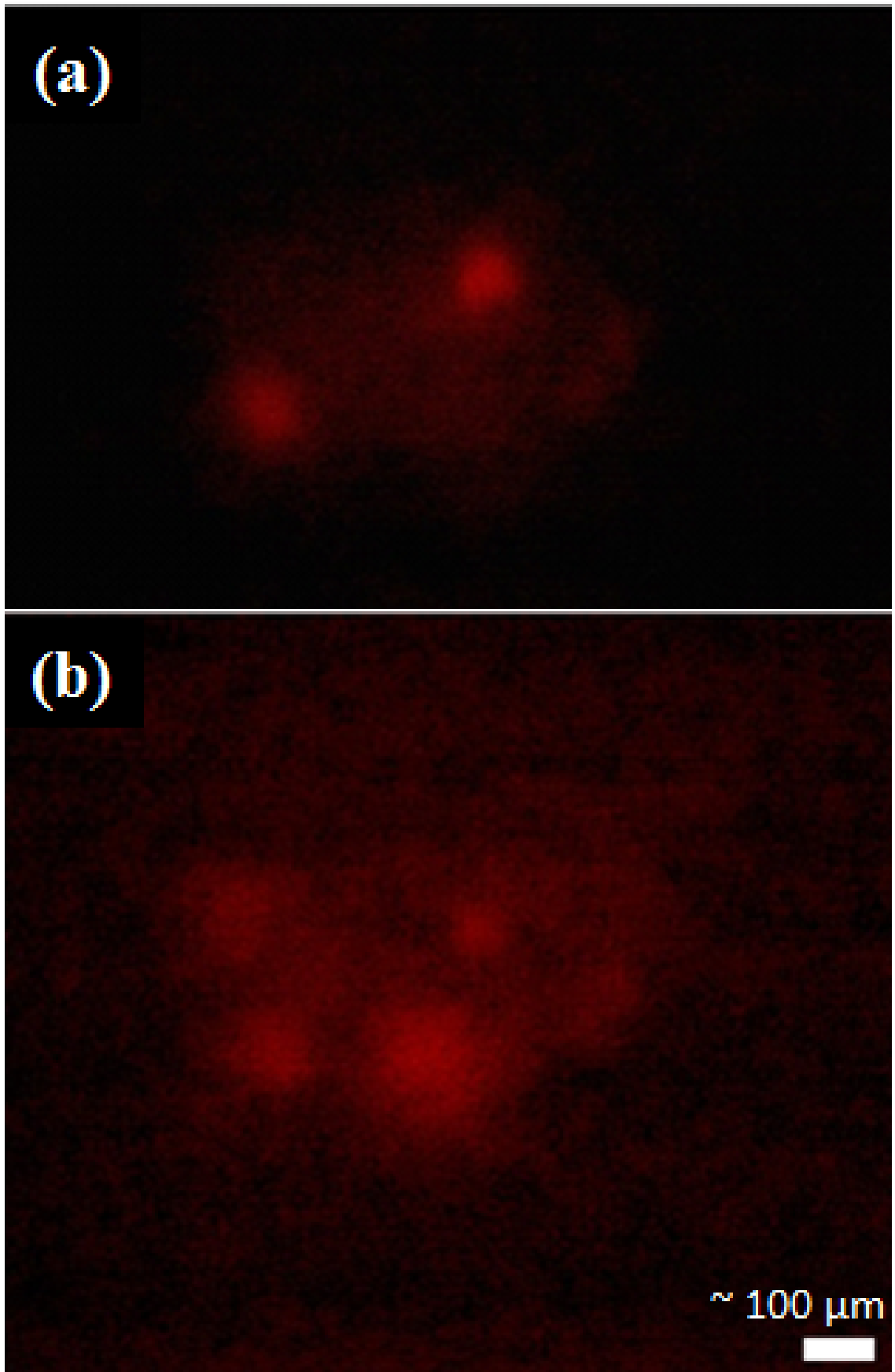
Figure 6.17: Cells containing propidium iodide before and after exposure to femtosecond pumping.

6.3.3 Life Extension Using Vitamin C

The mechanism of photobleaching in fluorescent dyes and proteins is caused by the production of ROS when they fluoresce. This damages both the fluorophore itself and more broadly the cell containing it. To counter this and try to extend the life of our laser we made use of the well-known antioxidant, vitamin C. Adding this to the cells prior to placing them in the laser cavity, we observed an increase in average lifetime as seen in *Figure 6.18*. Without vitamin C our longest recorded laser emission was for 60 seconds, at 1 kHz repetition rate. With vitamin C we observed lasing for up 140 seconds. This is a dramatic improvement considering the simplicity of adding the vitamin to the cells.

A comparison of cell lifetime using different concentrations of vitamin C is made in *Table 6.1*. All data was collected on the same day using the same cells in succession to minimise variations between the cells but there will be differences in laser cavity alignment. Despite these limitations we see a trend of increasing cell lifetime with vitamin C concentration though further studies would be required to determine an optimal concentration. For the analysis lasing was defined as an emission at least 50% of the peak emission.
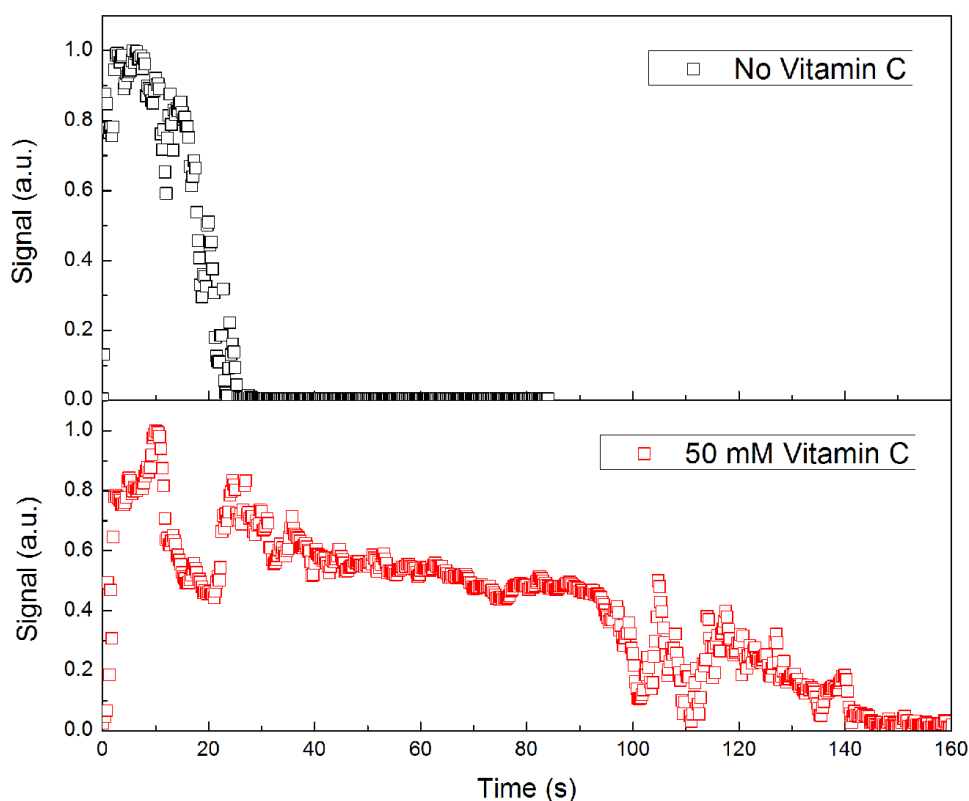
Figure 6.18: Cell lasing lifetime with and without Vitamin C. Pump pulse energy is 1.8 and 0.9 μJ respectively.

Concentration (mM)	Lifetime (s)	Standard deviation (s)
0	11.4	6.4
20	15.8	14.4
50	81	66.9

Table 6.1: Cell lasing lifetime for varying concentrations of vitamin C.

6.3.4 Calcium Sensitive Dye Response

Having demonstrated lasing and extended the lifetime of our laser we next investigated potential applications. The increase in detectability we observed in *Figure 6.9* is of use in any experiment which currently suffers from poor signal to noise ratio. Such an example is the use of fluorescent dyes which respond to cell properties and leads to a very small, and difficult to detect, change in emission. Incorporating such a dye into a laser has the potential to result in a much more detectable change.

For this experiment we made use of the calcium sensitive dye Fluo3 and caged calcium. The caged calcium is necessary to induce a change in the dye, though as an alternative there are some cells available which have predictable changes in calcium levels. Our microscope setup was modified to incorporate a UV source for uncaging the calcium in addition to the laser pump for the dye.

Doing so and investigating concentrations of dye, caged calcium and UV exposure we observed brief increases in fluorescence for cells when the calcium was released as seen in *Figure 6.19*. This increased fluorescence over time as the cells regulate intracellular calcium concentrations. We were not able to achieve lasing using this system. We believe this is due to the low emission intensity of the dye compared to Calcein AM.
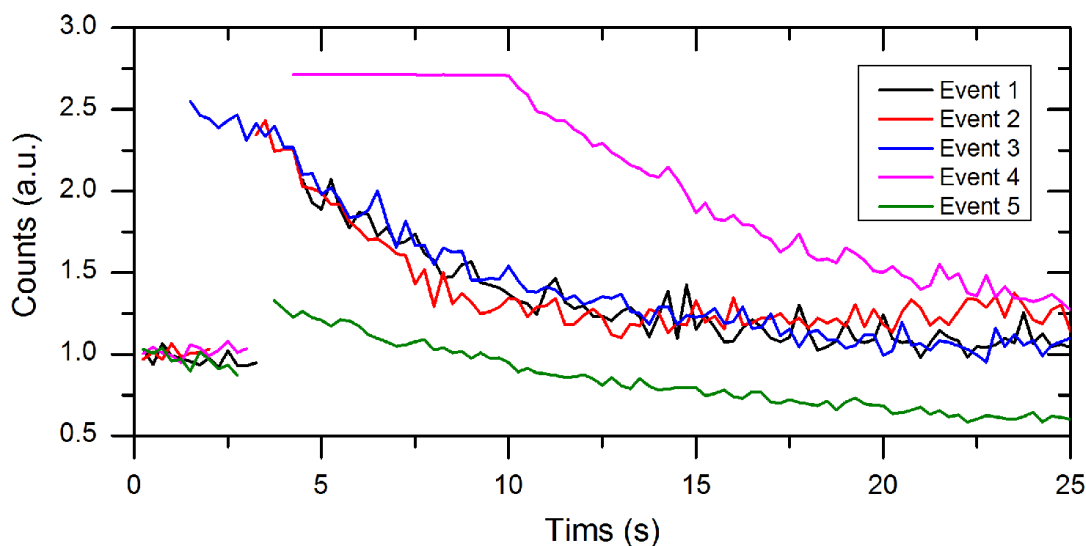
Figure 6.19: Fluorescence emission of Fluo3 when calcium is released into the cell. There is a brief fluorescence spike when UV light is applied which has been removed in the above graph.

6.4   Conclusion

The creation of a 'living' laser by including a fluorescent dye or protein inside a biological cell is a fascinating idea with the potential to significantly improve existing methods of fluorescence imaging while also enabling entirely new ways of examining cells. We decided to investigate these potential applications and how best to fabricate such lasers.

We achieved lasing using both eGFP and Calcein AM contained in HEK293 cells with the latter giving a low lasing threshold of 300 pJ and lasting for up to 60s, at 1 kHz repetition rate. After this time our cell emission decreased until lasing no longer occurred. Using a fluorescent viability marker, we were able to show this is not due to damage being caused to the cell itself but through photobleaching of our fluorophore. To improve performance, we made use of vitamin C to remove neutralise ROS in our cells increasing lifetime up to 140s.

Our lasing cells have 30 times higher peak emission compared to cells fluorescing making them easier to detect. This is potentially useful in any experiments which suffer from poor signal to noise ratio. To attempt to demonstrate this we used the fluorescent dye Fluo3 which increases in emission with calcium concentrations. Despite repeated attempts we were not able to observe lasing from these cells, a result we conclude is due to its lower

108

emission compared to the previous dye used, even in the presence of large amounts of calcium. From this we conclude that while it is possible to fabricate cell lasers, the process is highly dependent on the fluorophore used and that this may conflict with the desire to choose those which simply respond to the desired cell properties.

7. Conclusions and Future Work

7.1 Conclusion

In this thesis we have investigated the fabrication and use of microfluidic devices and biological lasers with the aim of developing biophotonics applications for each. In Chapter 3 we show how temperature can be monitored inside microfluidic devices and investigate how flow rate alters the distribution of heat inside devices. In Chapter 4 we fabricate an imaging flow cytometer for examining red blood cells. This is expanded on to incorporate the ability to take 3D focal stacks of cells incorporating more functions into a single device. Chapter 5 discusses the trapping of upconverting nanorods in a dual beam optical trap. Using this we position the nanorods arbitrarily and determine their orientation by sampling their emission with a polariser. In Chapter 6 we describe the fabrication of a biological laser from HEK293 cells containing eGFP or Calcein AM. We investigate ways of improving laser lifetime and potential applications. The following sections will summarise each of these chapters and discuss potential future work.

Chapter 3

Determining temperature inside microfluidic devices is crucial as temperature will influence the health of any biological samples that flow through or are help within them. Optical cell sorters utilising waveguides or fibre integration, or devices used with optical tweezers are of particular interest as laser powers in the 100's of mW are can be used. Traditionally we would use a thermometer to determine temperate but due to the scale of the devices being investigated this is likely to perturb the system, altering flow inside the device from normal operating conditions. Instead we monitored temperate by using two variants of Rhodamine dye to perform fluorescence thermometry. Rhodamine B decreases in emission intensity as temperature increases allowing us to monitor it while Rhodamine 110 remains constant acting as a reference level. Single channel devices were fabricated through ULI and selective chemical etching in fused silica. Additional PDMS devices were purchased to investigate different channel geometries and demonstrate that the method of temperature measurement worked in multiple materials. We successfully measured temperature inside these devices and observe that flow rate has a significant effect on the change in temperature and the distribution of temperature. Under typical operating conditions some of the devices underwent temperature increases of up to 20°C,

enough alter cell functions [63]. We conclude that fluorescence thermometry can be used in any microfluidic device and that there can be significant temperature increases with flow rate having a significant impact on both temperature change and distribution.

Chapter 4

Flow cytometry is a well-established tool for the analysis of cells giving information about number of cells, their size and shape. Through the addition of fluorescent stains, they can be used to investigate a wide variety of properties, such as identifying particular pathogens or highlighting specific areas or surface markers of cells. Taking advantage of the field of microfluidics, flow cytometers can be miniaturised thus increasing portability and decreasing cost. To investigate the uses of such devices we fabricated an imaging flow cytometer through ULI and selective chemical etching in fused silica. Using red blood cells, we achieved count rates of up to 4,700 cells per second, comparable to other demonstrations of such devices in PDMS. Fused silica is a more biocompatible and resilient material than PDMS which we demonstrated through the use of rhodamine dye comparing the staining of devices fabricated from fused silica and PDMS after use, showing significantly more staining of PDMS. Expanding on this work we incorporated the capability to take 3D focal stacks of cells into our device. This ability can give information about changes in cell shape, can determine cell health or the distribution of fluorescent stains throughout a cells. Using microspheres, we characterised the performance of our imaging system obtaining the expected spherical shape and a size of 4.1 ± 0.2 µm, in good agreement with the value 4.2 ± 0.2 µm given by the manufacturer. To demonstrate the imaging of an actual cell we used bovine sperm cell nuclei stained with DAPI obtaining a resolution of $\sim$ 15 nm, equal to 226 optical slices per cell.

Chapter 5

Every chapter in this thesis makes use of some form of fluorescent dye or protein. These are widely used in fluorescence imaging but have issues with photobleaching. An alternative is the use of Qdots but these have issues with phototoxicity. The development of a new class of materials, upconverting nanoparticles, has the potential to solve these issues which also provides benefits from being excited in the infrared rather than the visible or UV. We examine $NaYF_4$:Er^{3+},Yb^{3+} nanorods which have the interesting property of having polarised emission. Sampling their emission using a polariser we

demonstrate the ability to determine the particles' orientation, despite their sub diffraction limited size limiting our ability to image them directly. For this investigation we constructed a dual beam optical trap to capture and arbitrarily orientate individual nanorods. This successful method of determining nanorod orientation is simpler to implement than previous demonstrations making it more likely this technique could be used in applications such as security tagging or fluorescence experiments.

Chapter 6

Recently it has been demonstrated that it is possible to form a 'living' laser from a biological cell containing a fluorescent gain medium [26]. We investigate the fabrication and use of such lasers with the aim of enabling practical uses of interest in cell investigations. Using HEK293 cells containing eGFP and Calcein AM we successfully demonstrate lasing with a threshold of 300 pJ. This is lower than previously reported values most likely due to our use of femtosecond pumping. We determine that cells are unharmed by the lasing process using the viability indicator propidium iodide. This is clearly important if we are to propose using these cells to investigate cell function. From our experiments we observe that lasing only lasts a short period of time before photobleaching, with the longest continual lasing being 60 s, at 1 kHz repetition rate. To increase this, we use vitamin C, an antioxidant, to neutralise ROS in the cell slowing the process of photobleaching. This gives an improved lifetime of 140 s. Investigating potential applications we consider the monitoring of cell properties and how lasing could improve the sometimes small changes in fluorescent dyes which are sensitive to these properties. Fluo3 is such a dye which increases in emission as intracellular calcium levels increase. We attempt, but do not have success, in forming a laser using this dye and conclude that we do not have enough gain in the system to do so as the dye is less bright compared to Calcein AM and eGFP. From this investigation we determine that while it is possible to form cellular lasers, there is a requirement for bright fluorophores, and so any future work will need to identify those which have both bright emissions while also providing useful information about the cells containing them.

7.2 Future Work
Microfluidic SERS

Preliminary work was conducted looking at the incorporation of silver nanoparticles into microfluidic devices. As discussed in *Section 2.8* sliver nanoparticles are capable of enhancing Raman signals so of interest in analysis of cells or molecules. The goal of such a device would be the rapid, accurate and sensitive identification, followed by sorting of cells. Devices containing silver nanoparticles were fabricated in a two-step process using the same IMRA μ-Jewel laser. ULI and selective chemical etching were used to fabricate the device then a solution of silver nitrate and sodium citrate was added. Focusing the laser into this solution results in patterning of silver nanoparticles on the surface of the channel. The process of inscription is shown in Figure *7.1*. The results are shown in *Figure 7.2* where we have (a) nanoparticles inside a microfluidic device and SEM images of nanoparticles on fused silica substrates in (b) and (c).
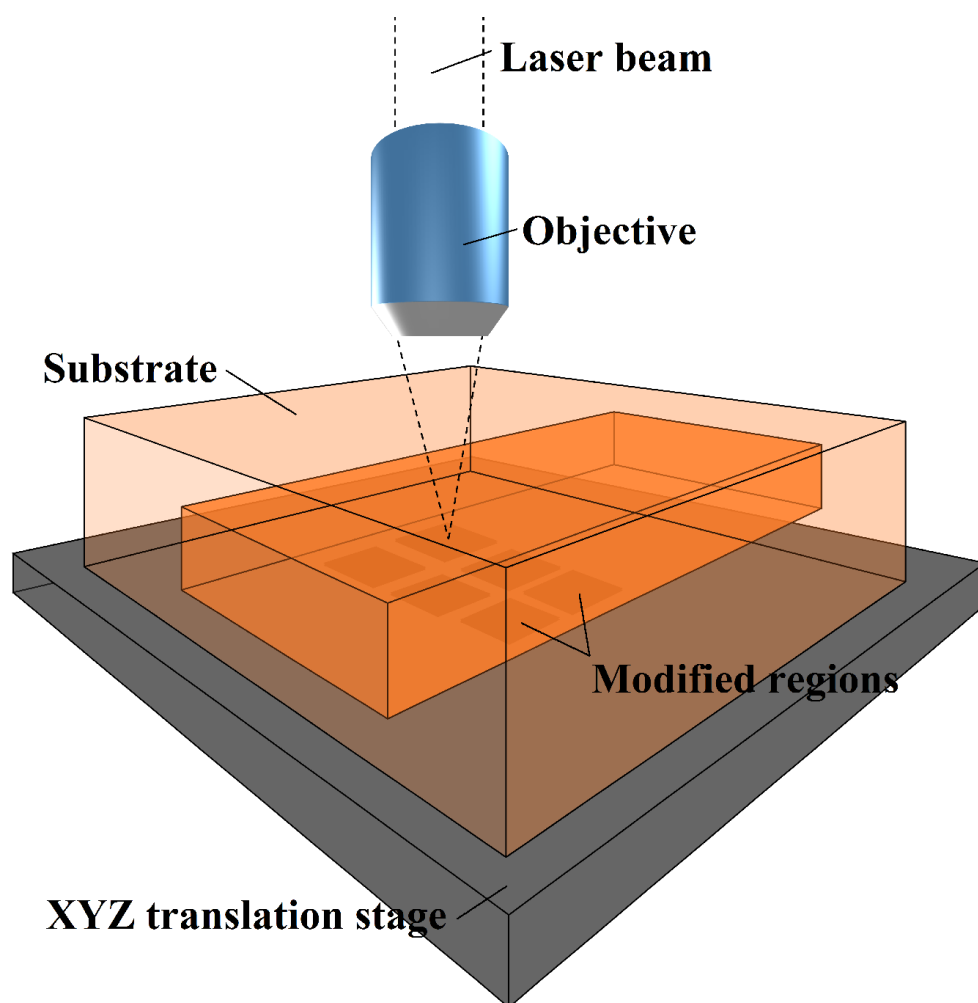
Figure 7.1: An illustration of silver nanoparticles inscription.
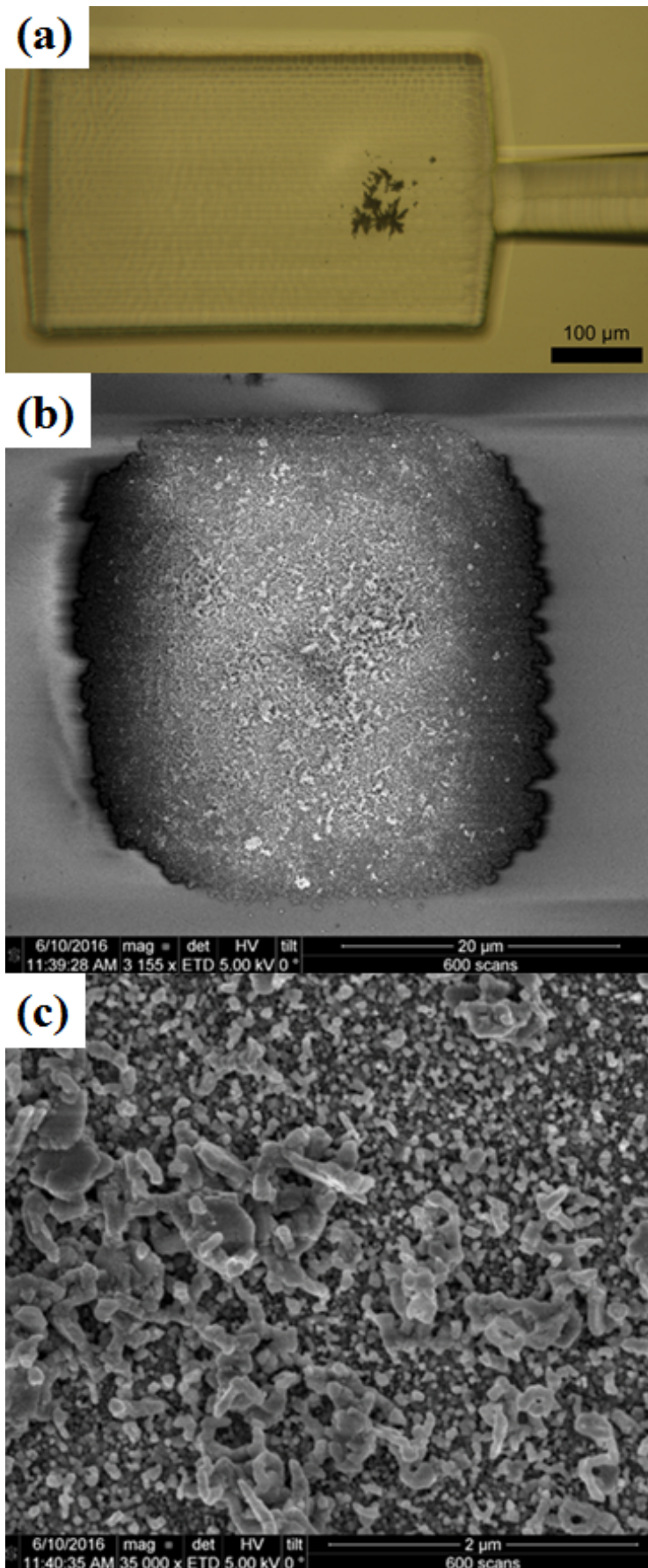
Figure 7.2: Silver nanoparticles. (a) silver nanoparticles inside a microfluidic device. (b) and (c) SEM images of silver nanoparticles on a fused silica substrate. Scale bar in (b) 20 μm and (c) 2 μm.

114

We found a wide range of laser parameters produced nanoparticles with the use of repeated overwrites of the same area giving the best results. These repeated overwrite scans gave an even distribution of nanoparticles and high Raman enhancement. *Figure 7.3* compares two regions inscribed using 400 and 600 scans with the translation speed of the laser being varied so that the total exposure time is the same. The enhancement is consistent within each region with 400 scans giving more enhancement compared to 600. Testing with Rhodamine 6G dye we were able to detect concentrations as low as 1 nM as shown in *Figure 7.4*. Further work would look at biological samples to demonstrate the ability to differentiate between cell types.
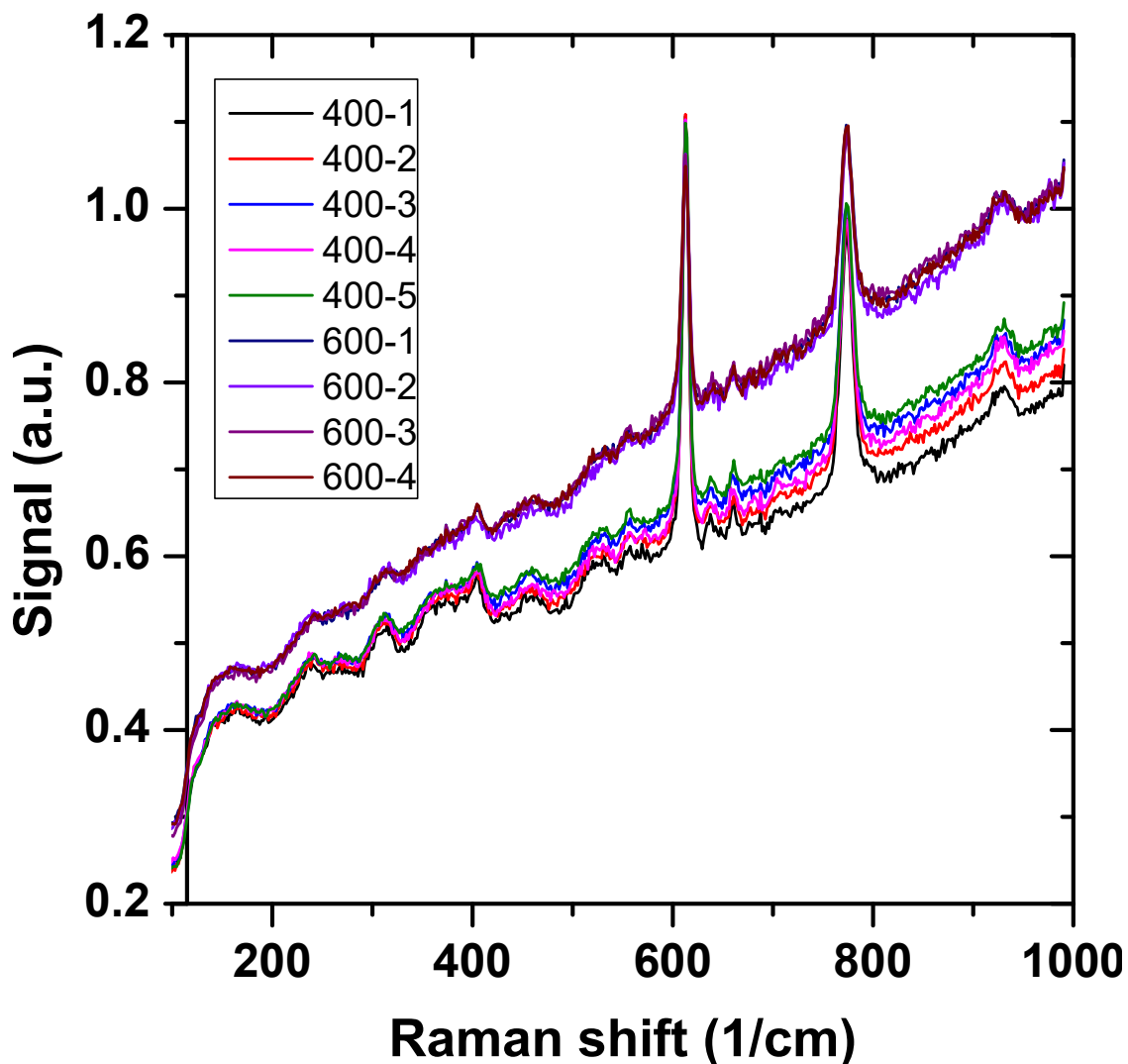
Figure 7.3: Repeat readings showing the difference in signal between silver nanoparticle regions, inscribed with 400 and 600 scans. Readings have been normalised for the 613 cm^{-1} peak.
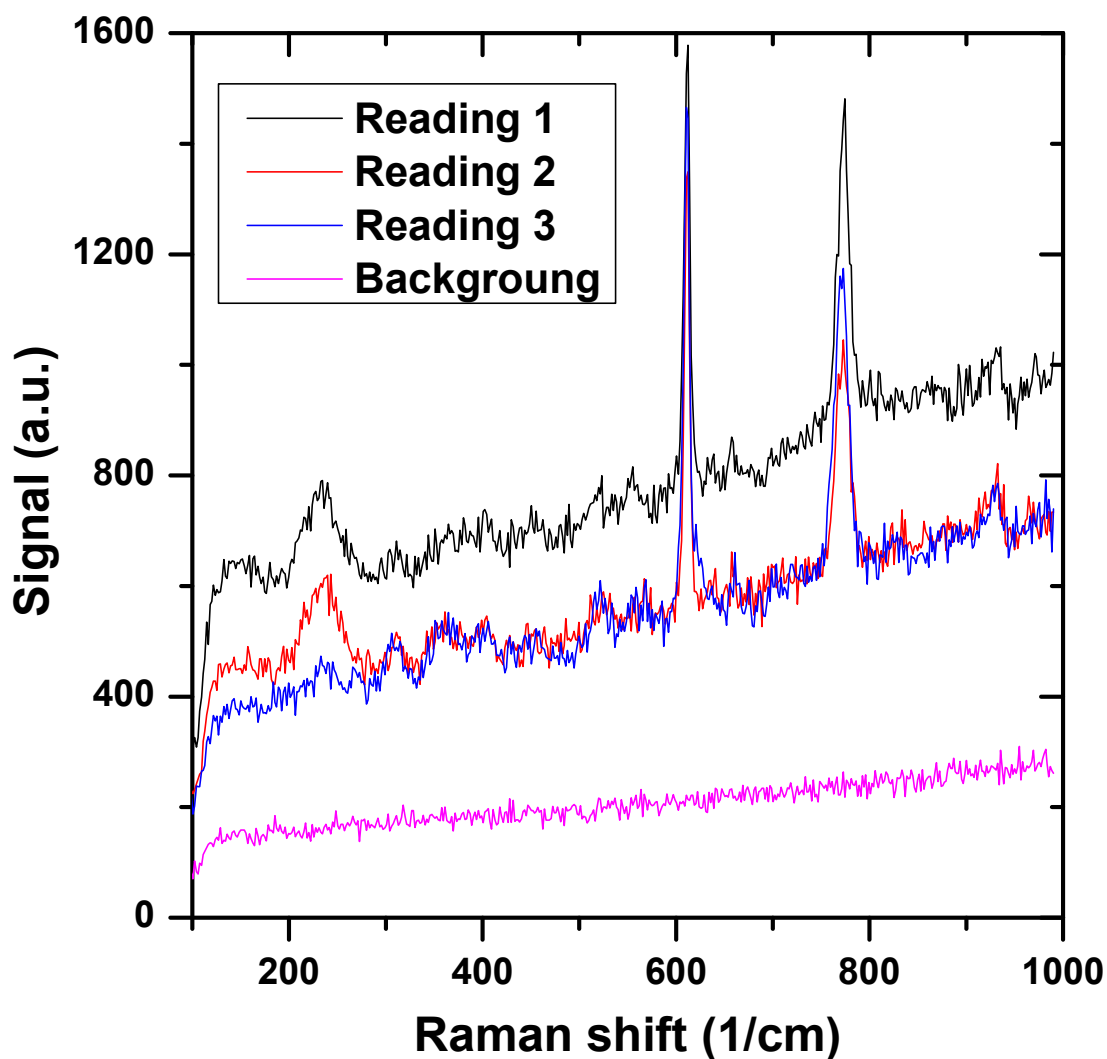
Figure 7.4: Raman signal for 1 nM Rhodamine 6G comparing compared to the background reading.

Upconverting Nanorods

The positioning and tracking of NaYF$_4$:Er^{3+},Yb^{3+} upconverting nanorods demonstrated in this thesis is a first step towards their use in both biological research, for tracking objects which are too small to image conventionally, and manufacturing, for example in anti-counterfeiting. The use of upconverting nanorods to track sub diffraction limit sized objects would add the capability of determining orientation to current methods of determining position. As our method requires only the addition of a polariser to current

experimental setups it has the potential to be implemented easily and cheaply into existing microscopes. This suggested application is illustrated in *Figure 7.5*, where we have a bacterium with attached nanorod being tracked. To demonstrate this application our current experimental setup will require modification. It currently uses a stationary optical trap into which nanorods diffuse. In contrast it will now be necessary to search for and then track a cell as it moves freely in multiple dimensions. This will require the addition of motorised stages and computerised control. Once tracking has been achieved the particles orientation must be monitored with acquisition time faster than expected changes in sample rotation. This would require the addition of a motorised polariser and spectrometer.
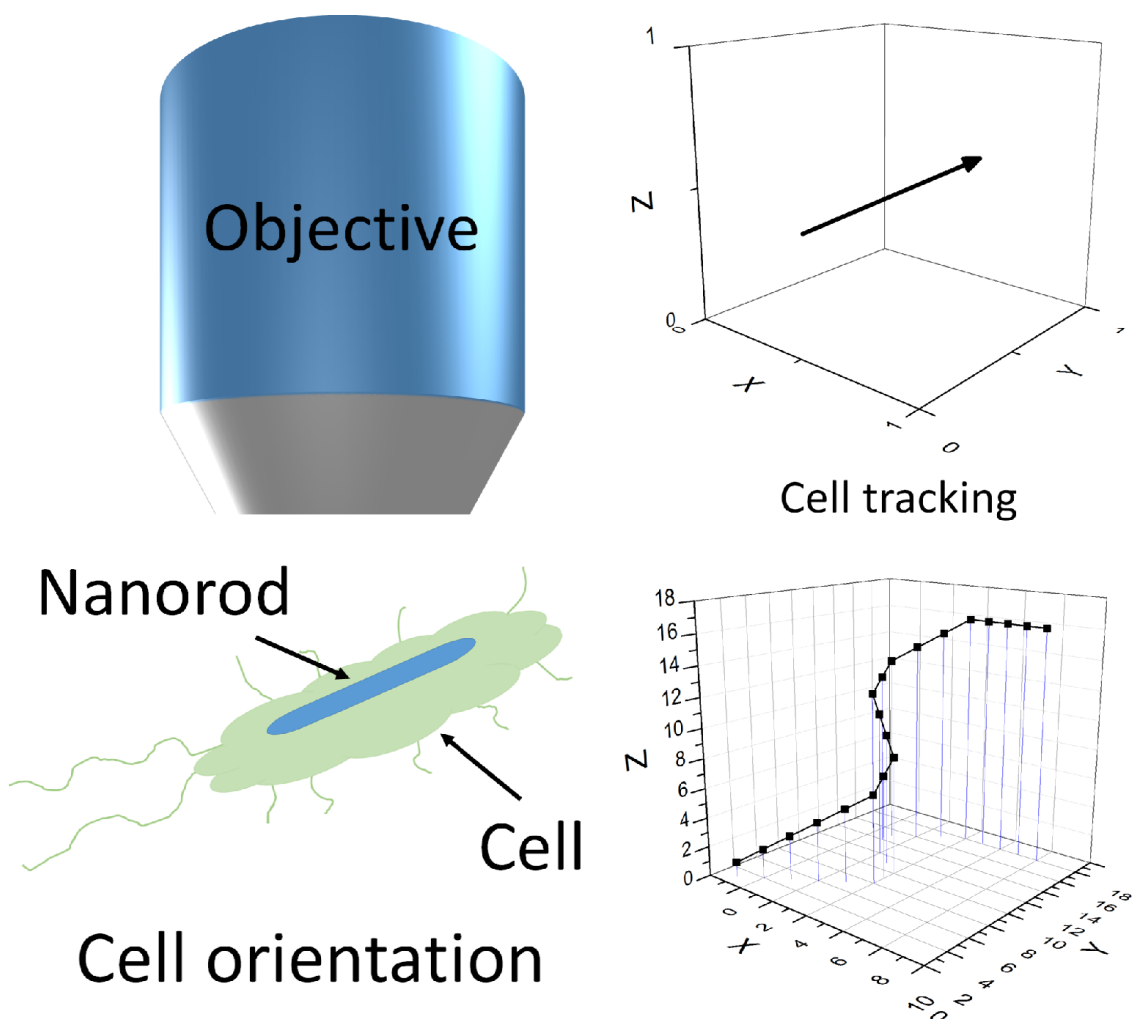
Figure 7.5: A cell being tracked with an embedded nanorod with its orientation and position being recorded over time.

Counterfeiting is a major issue with both currency and high value products. Tagging such items with a nanorod barcode has the potential to discourage counterfeiting as it would

require specialist equipment to implement [99]. This requires a balance where the fabrication and detection of such a barcode is simple to implement in a lab based setting but not so simple that it can be easily implemented by counterfeiters. Previous methods of nanorod detection have been cost prohibitive to implement [92] while we believe our method achieves the correct balance between ease and complexity. To the best of our knowledge there has been no use of optical tweezers for manufacturing purposes, outside of research applications, and implementing such a system is likely to be challenging.

Microfluidic Biological Laser

In this thesis we have demonstrated the fabrication of biological lasers showing that it is possible to maintain lasing for over one hundred thousand pulses. This provides enough time to investigate changes in cell properties such as the monitoring of calcium levels. To achieve this, we used a plane-plane cavity configuration in which cells were manually targeted for lasing. This process is suitable for the investigation of small groups of cells and for monitoring individual cells over time but for the analysis of large populations a different approach is required.

Examining large populations of cells, by analysing multiple single cells in parallel is important in biological research and in health care. Examples of this are investigating the natural variations within a single cell species, identifying the proportions of each species type in a mixed population and finding diseased cells amongst healthy ones. Such analysis is typically conducted using flow cytometry methods, which we investigate and discuss in *Section 4*. Incorporating cell lasing into such devices has the potential to provide increases in detectability, as shown in *Section 6*, or the introduction of new forms of analysis where the lasing emission itself gives information about the cells being investigated, for example cell size will change effective cavity length so by examining laser mode spacing it may be possible to determine this size.

Determining wherever such analysis is achievable will require further investigation for which we propose the device shown in *Figure 7.6*. This is a microfluidic cell laser, similar in concept to microfluidic dye lasers formed using Bragg mirrors embedded in the channel [100] or coated fibre tips [101]. Such a device can be fabricated in fused silica using ULI and selective chemical etching which allows for the fabrication of Bragg waveguides in the device to act as cavity mirrors. Initially the work will focus on fabricating such a device and demonstrating that it can be used to investigate cell lasing with high

throughput of cells. Once this has been achieved further functions can be integrated into the device, one of the benefits of microfluidics being the creation of a 'lab on a chip'; combining multiple functions into one chip. These additional function would be flow focusing to ensure cells are positioned consistently between the cavity mirrors and optical cell sorting, which would allow for cells of interest to be diverted to a separate output channel in the device.
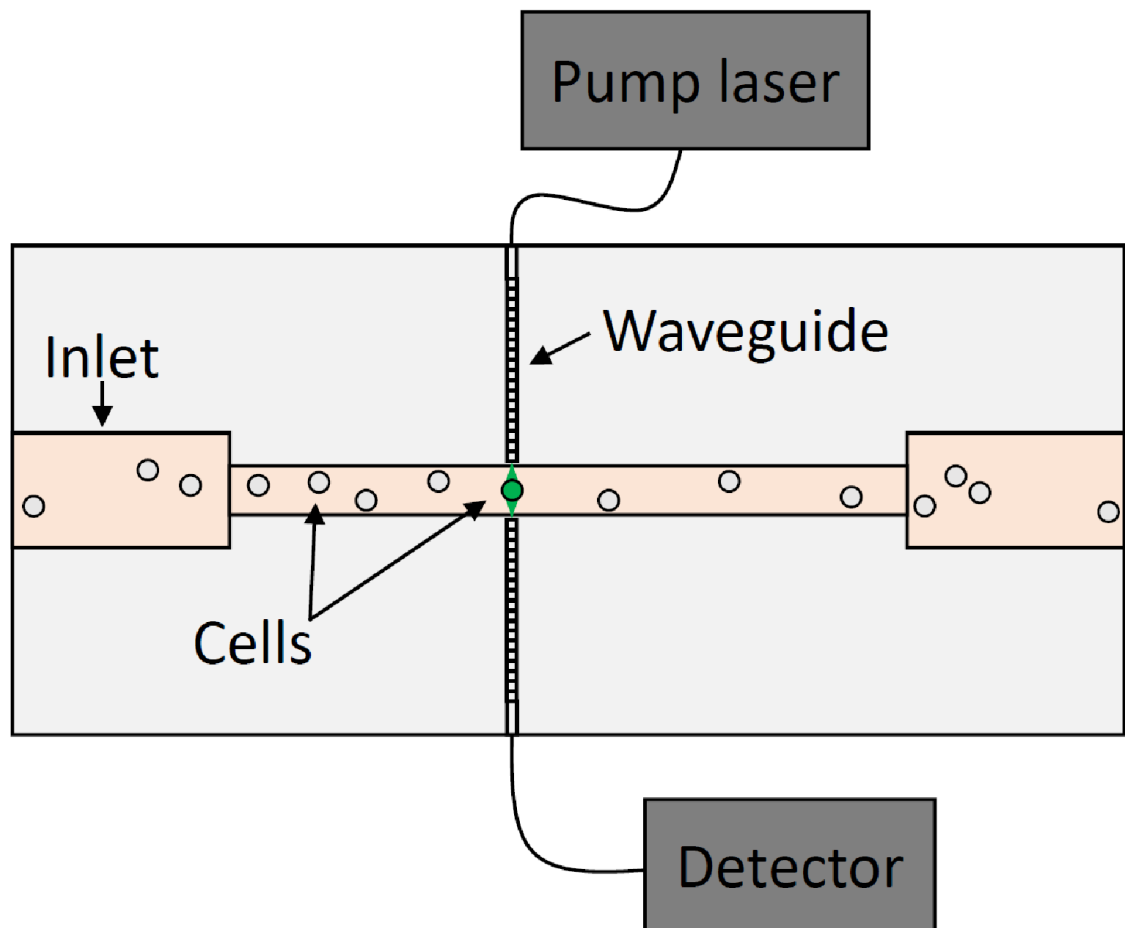
Figure 7.6: Microfluidic cell laser diagram with integrated Bragg waveguides acting as cavity mirrors.

7.3 Summary

In this thesis we have focused on the field of Biophotonics which combines the disciplines of biology and photonics to improve our understanding of cell function and disease. Through the fabrication of microfluidic devices and biological lasers we have investigated how these can be applied to these areas. Temperature is an important property to measure inside microfluidic devices as it impacts on cells function, health and

flow conditions inside the device. Using two dye fluorescence thermometry we demonstrated that we can measure temperature non-invasively and showed that flow rate has a significant effect on both temperature change and distribution. Flow cytometry is a widely used method of analysis large populations of cells and microfluidic flow cytometry offers the benefits of compact devices with low cost. Fabricating such a device we showed that we were able to obtain high quality 3D images of cells in a device which could be easily integrated into current microscopes. Upconverting nanorods were investigated as an interesting new fluorophore for fluorescence microscope. They have polarised emission which enables their orientation to be determined despite their sub diffraction limited size. We constructed a dual beam optical trap and demonstrated that we could both controllably position the particles and determine their orientation through the use of a simple polariser and spectrometer, improving on previous methods of determining nanorod orientation. Using biological cells containing fluorophores we fabricated living lasers and investigated their potential applications. We found that addition of vitamin C significantly increased their emission lifetime enabling longer investigations into their behaviour. All these techniques add to the repertoire of biophotonics techniques that enhance our understanding of the biomedical life sciences.

8. References

1. M. Diaz, M. Herrero, L. A. Garcia, and C. Quiros, "Application of flow cytometry to industrial microbial bioprocesses," Biochemical Engineering Journal **48**, 385-407 (2010).

2. T. H. Maiman, "STIMULATED OPTICAL RADIATION IN RUBY," Nature **187**, 493-494 (1960).

3. D. J. Stevenson, F. J. Gunn-Moore, P. Campbell, and K. Dholakia, "Single cell optical transfection," Journal of the Royal Society Interface **7**, 863-871 (2010).

4. R. R. Gattass, and E. Mazur, "Femtosecond laser micromachining in transparent materials," Nature Photonics **2**, 219-225 (2008).

5. R. Mary, G. Brown, S. J. Beecher, F. Torrisi, S. Milana, D. Popa, T. Hasan, Z. P. Sun, E. Lidorikis, S. Ohara, A. C. Ferrari, and A. K. Kar, "1.5 GHz picosecond pulse generation from a monolithic waveguide laser with a graphene-film saturable output coupler," Optics Express **21**, 7943-7950 (2013).

6. J. R. Macdonald, S. J. Beecher, P. A. Berry, G. Brown, K. L. Schepler, and A. K. Kar, "Efficient mid-infrared Cr:ZnSe channel waveguide laser operating at 2486 nm," Optics Letters **38**, 2194-2196 (2013).

7. S. J. Beecher, R. R. Thomson, B. P. Pal, and A. K. Kar, "Single Stage Ultrafast Laser Inscription of a Side-Polished Fiber-Like Waveguide Sensor," Ieee Sensors Journal **12**, 1263-1266 (2012).

8. T. A. Birks, I. Gris-Sanchez, S. Yerolatsitis, S. G. Leon-Saval, and R. R. Thomson, "The photonic lantern," Advances in Optics and Photonics **7**, 107-167 (2015).

9. E. K. Sackmann, A. L. Fulton, and D. J. Beebe, "The present and future role of microfluidics in biomedical research," Nature **507**, 181-189 (2014).

10. C. Hnatovsky, R. S. Taylor, P. P. Rajeev, E. Simova, V. R. Bhardwaj, D. M. Rayner, and P. B. Corkum, "Pulse duration dependence of femtosecond-laser-fabricated nanogratings in fused silica," Applied Physics Letters **87**, 3 (2005).

11.   D. Choudhury, A. Rodenas, L. Paterson, D. Jaque, A. K. Kar, and Ieee, "3D Microfabrication in YAG Crystals by Direct Laser Writing and Chemical Etching," 2013 Conference on Lasers and Electro-Optics Pacific Rim (Cleo-Pr), 2 (2013).

12.   B. H. Jo, L. M. Van Lerberghe, K. M. Motsegood, and D. J. Beebe, "Three-dimensional micro-channel fabrication in polydimethylsiloxane (PDMS) elastomer," Journal of Microelectromechanical Systems **9**, 76-81 (2000).

13.   R. M. Vazquez, R. Osellame, D. Nolli, C. Dongre, H. van den Vlekkert, R. Ramponi, M. Pollnau, and G. Cerullo, "Integration of femtosecond laser written optical waveguides in a lab-on-chip," Lab on a Chip **9**, 91-96 (2009).

14.   A. Keloth, L. Paterson, G. H. Markx, and A. K. Kar, "Three-dimensional optofluidic device for isolating microbes " SPIE Photonics West (2015).

15.   P. Paie, F. Bragheri, R. M. Vazquez, and R. Osellame, "Straightforward 3D hydrodynamic focusing in femtosecond laser fabricated microfluidic channels," Lab on a Chip **14**, 1826-1833 (2014).

16.   N. Bellini, K. C. Vishnubhatla, F. Bragheri, L. Ferrara, P. Minzioni, R. Ramponi, I. Cristiani, and R. Osellame, "Femtosecond laser fabricated monolithic chip for optical trapping and stretching of single cells," Optics Express **18**, 4679-4688 (2010).

17.   A. Crespi, Y. Gu, B. Ngamsom, H. Hoekstra, C. Dongre, M. Pollnau, R. Ramponi, H. H. van den Vlekkert, P. Watts, G. Cerullo, and R. Osellame, "Three-dimensional Mach-Zehnder interferometer in a microfluidic chip for spatially-resolved label-free detection," Lab on a Chip **10**, 1167-1173 (2010).

18.   Y. Cheng, K. Sugioka, K. Midorikawa, M. Masuda, K. Toyoda, M. Kawachi, and K. Shihoyama, "Three-dimensional micro-optical components embedded in photosensitive glass by a femtosecond laser," Optics Letters **28**, 1144-1146 (2003).

19.   F. Bragheri, P. Minzioni, R. M. Vazquez, N. Bellini, P. Paie, C. Mondello, R. Ramponi, I. Cristiani, and R. Osellame, "Optofluidic integrated cell sorter fabricated by femtosecond lasers," Lab on a Chip **12**, 3779-3784 (2012).

20. D. Choudhury, W. T. Ramsay, R. Kiss, N. A. Willoughby, L. Paterson, and A. K. Kar, "A 3D mammalian cell separator biochip," Lab on a Chip **12**, 948-953 (2012).

21. Y. C. Tan, V. Cristini, and A. P. Lee, "Monodispersed microfluidic droplet generation by shear focusing microfluidic device," Sens. Actuator B-Chem. **114**, 350-356 (2006).

22. M. Zimmer, "GFP: from jellyfish to the Nobel prize and beyond," Chemical Society Reviews **38**, 2823-2832 (2009).

23. M. Chalfie, Y. Tu, G. Euskirchen, W. W. Ward, and D. C. Prasher, "GREEN FLUORESCENT PROTEIN AS A MARKER FOR GENE-EXPRESSION," Science **263**, 802-805 (1994).

24. G. J. Kremers, S. G. Gilbert, P. J. Cranfill, M. W. Davidson, and D. W. Piston, "Fluorescent proteins at a glance," Journal of Cell Science **124**, 157-160 (2011).

25. D. J. Pikas, S. M. Kirkpatrick, E. Tewksbury, L. L. Brott, R. R. Naik, M. O. Stone, and W. M. Dennis, "Nonlinear saturation and lasing characteristics of green fluorescent protein," Journal of Physical Chemistry B **106**, 4831-4837 (2002).

26. M. C. Gather, and S. H. Yun, "Single-cell biological lasers," Nature Photonics **5**, 406-410 (2011).

27. M. Beresna, M. Gecevicius, and P. G. Kazansky, "Ultrafast laser direct writing and nanostructuring in transparent materials," Advances in Optics and Photonics **6**, 293-339 (2014).

28. C. B. Schaffer, A. Brodeur, and E. Mazur, "Laser-induced breakdown and damage in bulk transparent materials induced by tightly focused femtosecond laser pulses," Measurement Science & Technology **12**, 1784-1794 (2001).

29. Y. Shimotsuma, P. G. Kazansky, J. R. Qiu, and K. Hirao, "Self-organized nanogratings in glass irradiated by ultrashort light pulses," Physical Review Letters **91**, 4 (2003).

30. V. R. Bhardwaj, E. Simova, P. P. Rajeev, C. Hnatovsky, R. S. Taylor, D. M. Rayner, and P. B. Corkum, "Optically produced arrays of planar nanostructures inside fused silica," Physical Review Letters **96**, 4 (2006).

31. M. Huang, F. L. Zhao, Y. Cheng, N. S. Xu, and Z. Z. Xu, "Origin of Laser-Induced Near-Subwavelength Ripples: Interference between Surface Plasmons and Incident Laser," Acs Nano **3**, 4062-4070 (2009).

32. R. R. Thomson, A. S. Bockelt, E. Ramsay, S. Beecher, A. H. Greenaway, A. K. Kar, and D. T. Reid, "Shaping ultrafast laser inscribed optical waveguides using a deformable mirror," Optics Express **16**, 12786-12793 (2008).

33. M. Ams, G. D. Marshall, D. J. Spence, and M. J. Withford, "Slit beam shaping method for femtosecond laser direct-write fabrication of symmetric waveguides in bulk glasses," Optics Express **13**, 5676-5681 (2005).

34. G. Cerullo, R. Osellame, S. Taccheo, M. Marangoni, D. Polli, R. Ramponi, P. Laporta, and S. De Silvestri, "Femtosecond micromachining of symmetric waveguides at 1.5 mu m by astigmatic beam focusing," Optics Letters **27**, 1938-1940 (2002).

35. C. Hnatovsky, R. S. Taylor, E. Simova, V. R. Bhardwaj, D. M. Rayner, and P. B. Corkum, "Polarization-selective etching in femtosecond laser-assisted microfluidic channel fabrication in fused silica," Optics Letters **30**, 1867-1869 (2005).

36. G. Spierings, "WET CHEMICAL ETCHING OF SILICATE-GLASSES IN HYDROFLUORIC-ACID BASED SOLUTIONS," Journal of Materials Science **28**, 6261-6273 (1993).

37. S. J. Remington, "Green fluorescent protein: A perspective," Protein Science **20**, 1509-1519 (2011).

38. D. M. Chudakov, M. V. Matz, S. Lukyanov, and K. A. Lukyanov, "Fluorescent Proteins and Their Applications in Imaging Living Cells and Tissues," Physiological Reviews **90**, 1103-1163 (2010).

39. B. A. Pollok, and R. Heim, "Using GFP in FRET-based applications," Trends in Cell Biology **9**, 57-60 (1999).

40. B. Huang, M. Bates, and X. W. Zhuang, "Super-Resolution Fluorescence Microscopy," in *Annual Review of Biochemistry*(Annual Reviews, 2009), pp. 993-1016.

41. H. Patel, C. Tscheka, and H. Heerklotz, "Characterizing vesicle leakage by fluorescence lifetime measurements," Soft Matter **5**, 2849-2851 (2009).

42. M. Y. Berezin, and S. Achilefu, "Fluorescence Lifetime Measurements and Biological Imaging," Chemical Reviews **110**, 2641-2684 (2010).

43. T. M. Drane, H. Bach, M. Shapiro, and V. Milner, "Femtosecond pumped lasing from the fluorescent protein DsRed in a one dimensional random cavity," in *Frontiers in Ultrafast Optics: Biomedical, Scientific, and Industrial Applications Xiii*, A. Heisterkamp, P. R. Herman, M. Meunier, and S. Nolte, eds. (Spie-Int Soc Optical Engineering, 2013).

44. H. Azzouz, L. Alkhafadiji, S. Balslev, J. Johansson, N. A. Mortensen, S. Nilsson, and A. Kristensen, "Levitated droplet dye laser," Optics Express **14**, 4374-4379 (2006).

45. S. K. Y. Tang, Z. Y. Li, A. R. Abate, J. J. Agresti, D. A. Weitz, D. Psaltis, and G. M. Whitesides, "A multi-color fast-switching microfluidic droplet dye laser," Lab on a Chip **9**, 2767-2771 (2009).

46. A. Ashkin, "ACCELERATION AND TRAPPING OF PARTICLES BY RADIATION PRESSURE," Physical Review Letters **24**, 156-& (1970).

47. A. Ashkin, and J. M. Dziedzic, "OPTICAL LEVITATION BY RADIATION PRESSURE," Applied Physics Letters **19**, 283-& (1971).

48. A. Ashkin, and J. M. Dziedzic, "OPTICAL TRAPPING AND MANIPULATION OF VIRUSES AND BACTERIA," Science **235**, 1517-1520 (1987).

49. J. R. Moffitt, Y. R. Chemla, S. B. Smith, and C. Bustamante, "Recent advances in optical tweezers," in *Annual Review of Biochemistry*(Annual Reviews, 2008), pp. 205-228.

50.   J. E. Molloy, and M. J. Padgett, "Lights, action: optical tweezers," Contemporary Physics **43**, 241-258 (2002).

51.   H. Zhang, and K. K. Liu, "Optical tweezers for single cells," Journal of the Royal Society Interface **5**, 671-690 (2008).

52.   P. C. Ashok, B. B. Praveen, and K. Dholakia, "Near infrared spectroscopic analysis of single malt Scotch whisky on an optofluidic chip," Optics Express **19**, 22982-22992 (2011).

53.   M. Moskovits, "Surface-enhanced Raman spectroscopy: a brief retrospective," Journal of Raman Spectroscopy **36**, 485-496 (2005).

54.   P. L. Stiles, J. A. Dieringer, N. C. Shah, and R. R. Van Duyne, "Surface-Enhanced Raman Spectroscopy," in *Annual Review of Analytical Chemistry*(Annual Reviews, 2008), pp. 601-626.

55.   J. Fabrega, S. N. Luoma, C. R. Tyler, T. S. Galloway, and J. R. Lead, "Silver nanoparticles: Behaviour and effects in the aquatic environment," Environment International **37**, 517-531 (2011).

56.   M. Ahamed, M. S. AlSalhi, and M. K. J. Siddiqui, "Silver nanoparticle applications and human health," Clinica Chimica Acta **411**, 1841-1848 (2010).

57.   B. B. Xu, Z. C. Ma, L. Wang, R. Zhang, L. G. Niu, Z. Yang, Y. L. Zhang, W. H. Zheng, B. Zhao, Y. Xu, Q. D. Chen, H. Xia, and H. B. Sun, "Localized flexible integration of high-efficiency surface enhanced Raman scattering (SERS) monitors into microfluidic channels," Lab on a Chip **11**, 3347-3351 (2011).

58.   L. F. Gorup, E. Longo, E. R. Leite, and E. R. Camargo, "Moderating effect of ammonia on particle growth and stability of quasi-monodisperse silver nanoparticles synthesized by the Turkevich method," Journal of Colloid and Interface Science **360**, 355-358 (2011).

59.   Q. H. Tran, V. Q. Nguyen, and A. T. Le, "Silver nanoparticles: synthesis, properties, toxicology, applications and perspectives," Advances in Natural Sciences-Nanoscience and Nanotechnology **4**, 20 (2013).

60.   C. A. Jarro, M. Bresin, and J. T. Hastings, "Control of the structure and density of silver nanoparticles obtained by laser-induced chemical deposition from liquids," Journal of Vacuum Science & Technology B **31**, 6 (2013).

61.   D. Mark, S. Haeberle, G. Roth, F. von Stetten, and R. Zengerle, "Microfluidic lab-on-a-chip platforms: requirements, characteristics and applications," Chemical Society Reviews **39**, 1153-1182 (2010).

62.   D. Choudhury, J. R. Macdonald, and A. K. Kar, "Ultrafast laser inscription: perspectives on future integrated applications," Laser & Photonics Reviews **8**, 827-846 (2014).

63.   T. R. Kiessling, R. Stange, J. A. Kas, and A. W. Fritsch, "Thermorheology of living cells-impact of temperature variations on cell mechanics," New Journal of Physics **15**, 19 (2013).

64.   F. Vetrone, R. Naccache, A. Zamarron, A. J. de la Fuente, F. Sanz-Rodriguez, L. M. Maestro, E. M. Rodriguez, D. Jaque, J. G. Sole, and J. A. Capobianco, "Temperature Sensing Using Fluorescent Nanothermometers," Acs Nano **4**, 3254-3258 (2010).

65.   D. Jaque, and F. Vetrone, "Luminescence nanothermometry," Nanoscale **4**, 4301-4326 (2012).

66.   L. V. Johnson, M. L. Walsh, and L. B. Chen, "LOCALIZATION OF MITOCHONDRIA IN LIVING CELLS WITH RHODAMINE-123," Proceedings of the National Academy of Sciences of the United States of America-Biological Sciences **77**, 990-994 (1980).

67.   S. K. Ko, Y. K. Yang, J. Tae, and I. Shin, "In vivo monitoring of mercury ions using a rhodamine-based molecular probe," Journal of the American Chemical Society **128**, 14150-14155 (2006).

68.   A. M. Michaels, M. Nirmal, and L. E. Brus, "Surface enhanced Raman spectroscopy of individual rhodamine 6G molecules on large Ag nanocrystals," Journal of the American Chemical Society **121**, 9932-9939 (1999).

69. J. Sakakibara, and R. J. Adrian, "Whole field measurement of temperature in water using two-color laser induced fluorescence," Experiments in Fluids **26**, 7-15 (1999).

70. L. H. Kou, D. Labrie, and P. Chylek, "REFRACTIVE-INDEXES OF WATER AND ICE IN THE 0.65-MU-M TO 2.5-MU-M SPECTRAL RANGE," Applied Optics **32**, 3531-3540 (1993).

71. G. Baffou, R. Quidant, and F. J. G. de Abajo, "Nanoscale Control of Optical Heating in Complex Plasmonic Systems," Acs Nano **4**, 709-716 (2010).

72. L. A. Herzenberg, D. Parks, B. Sahaf, O. Perez, M. Roederer, and L. A. Herzenberg, "The history and future of the fluorescence activated cell sorter and flow cytometry: A view from Stanford," Clinical Chemistry **48**, 1819-1827 (2002).

73. Y. Y. Wang, F. Hammes, K. De Roy, W. Verstraete, and N. Boon, "Past, present and future applications of flow cytometry in aquatic microbiology," Trends in Biotechnology **28**, 416-424 (2010).

74. F. Hammes, M. Berney, Y. Y. Wang, M. Vital, O. Koster, and T. Egli, "Flow-cytometric total bacterial cell counts as a descriptive microbiological parameter for drinking water treatment processes," Water Res. **42**, 269-277 (2008).

75. D. B. Kay, J. L. Cambier, and L. L. Wheeless, "IMAGING IN FLOW," Journal of Histochemistry & Cytochemistry **27**, 329-334 (1979).

76. E. Schonbrun, S. S. Gorthi, and D. Schaak, "Microfabricated multiple field of view imaging flow cytometry," Lab on a Chip **12**, 268-273 (2012).

77. G. T. Roman, T. Hlaus, K. J. Bass, T. G. Seelhammer, and C. T. Culbertson, "Sol-gel modified poly(dimethylsiloxane) microfluidic devices with high electroosmotic Mobilities and hydrophilic channel wall characteristics," Analytical Chemistry **77**, 1414-1422 (2005).

78. M. W. Toepke, and D. J. Beebe, "PDMS absorption of small molecules and consequences in microfluidic applications," Lab on a Chip **6**, 1484-1486 (2006).

79. D. A. Basiji, W. E. Ortyn, L. Liang, V. Venkatachalam, and P. Morrissey, "Cellular image analysis and imaging by flow cytometry," Clin. Lab. Med. **27**, 653-+ (2007).

80. N. C. Pegard, and J. W. Fleischer, "Three-dimensional deconvolution microfluidic microscopy using a tilted channel," Journal of Biomedical Optics **18**, 3 (2013).

81. S. S. Gorthi, and E. Schonbrun, "Phase imaging flow cytometry using a focus-stack collecting microscope," Optics Letters **37**, 707-709 (2012).

82. D. Powell, D. G. Cran, C. Jennings, and R. Jones, "SPATIAL-ORGANIZATION OF REPETITIVE DNA-SEQUENCES IN THE BOVINE SPERM NUCLEUS," Journal of Cell Science **97**, 185-191 (1990).

83. G. Gopakumar, V. K. Jagannadh, S. S. Gorthi, and G. Subrahmanyam, "Framework for morphometric classification of cells in imaging flow cytometry," J. Microsc.. **261**, 307-319 (2016).

84. P. Sarder, and A. Nehorai, "Deconvolution methods for 3-D fluorescence microscopy images," Ieee Signal Processing Magazine **23**, 32-45 (2006).

85. K. Konig, "Multiphoton microscopy in life sciences," J. Microsc.. **200**, 83-104 (2000).

86. F. Wang, D. Banerjee, Y. S. Liu, X. Y. Chen, and X. G. Liu, "Upconversion nanoparticles in biological labeling, imaging, and therapy," Analyst **135**, 1839-1854 (2010).

87. G. Y. Chen, H. L. Qju, P. N. Prasad, and X. Y. Chen, "Upconversion Nanoparticles: Design, Nanochemistry, and Applications in Theranostics," Chemical Reviews **114**, 5161-5214 (2014).

88. H. E. Ruda, and A. Shik, "Polarization-sensitive optical phenomena in semiconducting and metallic nanowires," Physical Review B **72**, 11 (2005).

89. J. Wang, M. Gudiksen, X. Duan, Y. Cui, and C. Lieber, "Highly polarized photoluminescence and photodetection from single indium phosphide nanowires," Science **293**, 1455-1457 (2001).

90. G. P. Dong, H. L. He, Q. W. Pan, G. X. Chen, J. H. Xie, Z. J. Ma, and M. Y. Peng, "Controllable Synthesis and Peculiar Optical Properties of Lanthanide-Doped Fluoride Nanocrystals," ChemPlusChem **79**, 601-609 (2014).

91. J. J. Zhou, G. X. Chen, E. Wu, G. Bi, B. T. Wu, Y. Teng, S. F. Zhou, and J. R. Qiu, "Ultrasensitive Polarized Up-Conversion of Tm3+-Yb3+ Doped beta-NaYF4 Single Nanorod," Nano Letters **13**, 2241-2246 (2013).

92. Y. H. Zhang, L. X. Zhang, R. R. Deng, J. Tian, Y. Zong, D. Y. Jin, and X. G. Liu, "Multicolor Barcoding in a Single Upconversion Crystal," Journal of the American Chemical Society **136**, 4893-4896 (2014).

93. S. Liu, G. Chen, T. Y. Ohulchanskyy, M. T. Swihart, and P. N. Prasad, "Facile Synthesis and Potential Bioimaging Applications of Hybrid Upconverting and Plasmonic NaGdF4: Yb3+, Er3+/Silica/Gold Nanoparticles," Theranostics **3**, 7 (2013).

94. Dominika Wawrzynczyk, Dawid Piatkowski, Sebastian Mackowski, Marek Samoca, and M. Nyk, "Microwave-assisted synthesis and single particle spectroscopy of infrared down- and visible up-conversion in Er3+ and Yb3+ co-doped fluoride nanowires," Journal of Materials Chemistry C (2015).

95. M. Humar, and S. H. Yun, "Intracellular microlasers," Nature Photonics **9**, 572 (2015).

96. M. Schubert, A. Steude, P. Liehm, N. M. Kronenberg, M. Karl, E. C. Campbell, S. J. Powis, and M. C. Gather, "Lasing within Live Cells Containing Intracellular Optical Microresonators for Barcode-Type Cell Tagging and Tracking," Nano Letters **15**, 5647-5652 (2015).

97. A. Jonas, M. Aas, Y. Karadag, S. Manioglu, S. Anand, D. McGloin, H. Bayraktar, and A. Kiraz, "In vitro and in vivo biolasing of fluorescent proteins suspended in liquid microdroplet cavities," Lab on a Chip **14**, 3093-3100 (2014).

98. M. Humar, M. C. Gather, and S. H. Yun, "Cellular dye lasers: lasing thresholds and sensing in a planar resonator," Optics Express **23**, 27865-27879 (2015).

99. B. Creran, B. Yan, D. F. Moyano, M. M. Gilbert, R. W. Vachet, and V. M. Rotello, "Laser desorption ionization mass spectrometric imaging of mass

barcoded gold nanoparticles for security applications," Chem. Commun. **48**, 4543-4545 (2012).

100. Z. Li, Z. Zhang, T. Emery, A. Scherer, and D. Psaltis, "Single mode optofluidic distributed feedback dye laser," Optics Express **14**, 696-701 (2006).

101. G. Aubry, Q. Kou, J. Soto-Velasco, C. Wang, S. Meance, J. J. He, and A. M. Haghiri-Gosnet, "A multicolor microfluidic droplet dye laser with single mode emission," Appl. Phys. Lett **98** (2011).